University of Nevada, Reno

Experimental Investigations of Carbon and Titanium Molecular Species in Laser Ablation Plumes

A dissertation submitted in partial fulfillment of the
requirements for the degree of Doctor of Philosophy in
Physics

by

Jeremy Jean Iratcabal

Professor Aaron M. Covington / Dissertation Advisor

August 2020

THE GRADUATE SCHOOL

We recommend that the dissertation
prepared under our supervision by

JEREMY JEAN IRATCABAL

Entitled

Experimental Investigations Of Carbon And Titanium Molecular Species In Laser Ablation Plumes

be accepted in partial fulfillment of the
requirements for the degree of

DOCTOR OF PHILOSOPHY

Aaron M. Covington, Ph.D., Advisor

Roberto C. Mancini, Ph.D., Committee Member

Paul A. Neill, Ph.D., Committee Member

Sergey A. Varganov, Ph.D., Committee Member

Robert J. Watters, Ph.D., Graduate School Representative

David W. Zeh, Ph. D., Dean, Graduate School
August, 2020

Abstract

A new multi-parameter apparatus has been developed for this dissertation in order to study laser ablation. The purpose of this apparatus is to better understand the evolution and energy partitioning of an ablation plume from the warm dense plasma stage to the cool neutral gas stage. The Laser Ablation Plume Experiment (LAPeX) apparatus was designed and built to include a large number of optical and spectroscopic diagnostics, various background environment configurations, and adjustable laser intensity. This new experimental platform required the design, assembly, alignment, calibration, and testing of the various components involved. Extensive metrology and characterization of the diagnostic elements of the apparatus were undertaken to ensure the quality of the data.

Diatomic carbon was investigated using absorption spectroscopy. Graphite was ablated into a 100 Torr nitrogen atmosphere with a 1,024 nm pulsed Nd:YAG laser. A quasi-CW supercontinuum laser was used to generate the absorption probe beam. High resolution spectroscopic data of the Swan bands for $\Delta v = 0$ and $\Delta v = 1$ was collected and compared to simulations. A data reduction method was developed to extract an absorption spectrum from the data. Simulations indicated that the plume was not in thermodynamic equilibrium.

TiO was produced by ablating titanium into a 100 Torr oxygen atmosphere. TiO absorption is observed in material ejected from the yellow hypergiant ρ Cassiopeiae. Fast imaging of the plume, with a band-pass filter to allow only TiO γ band emission, showed emission at $t \geq 5$ μs after target irradiation. Spectroscopic analysis of emission from neutral titanium at 5 μs indicated a temperature of $\sim 1,000$ K. The strongest TiO emission was observed 1-3 mm behind the shock wave with fast imaging and spectroscopy.

Acknowledgments

I would like to thank and acknowledge Professor Aaron Covington of the Physics Department, my doctoral advisor, for the opportunity that he gave me to build and develop a new lab, and conduct the first experiments on the LAPeX apparatus. I appreciate his ideas, enthusiasm, and support that made this project successful. He has been a true mentor during my time as a graduate student.

My doctoral committee members, Professor Roberto Mancini, of the Physics Department, Professor Paul Neill, of the Physics Department, Professor Sergey Varganov, of the Chemistry Department, and Professor Robert Watters, of the Department of Geological Engineering, each deserve acknowledgment and my appreciation for the time that each of them took to review my dissertation. Dr. Timothy Darling, who was a member of this project and my doctoral committee until his retirement, deserves my appreciation for his suggestions.

I would like to acknowledge several people for loaning equipment to this project. Former graduate student, Dr. Eric Dutra, and Mission Support and Test Services, LLC generously provided various calibration instruments and a spectrometer for the work on LAPeX. Tom Babcock and NKT Photonics loaned the SuperK EXTREME supercontinuum laser to the LAPeX apparatus for the work described in Chapter 4. Dr. Bernhard Bach deserves a thank you for loaning a laser to this project for calibration.

I would like to acknowledge, also, Dr. Piotr Wiewior, for helping to assemble the supercontinuum laser system. Thanks go to fellow graduate student Kyle Swanson for his helpful tips on the analysis of interferometry. Thank you to Dr. Vernon Davis for his experimental tips. Acknowledgment is also given to the technical staff, Alexey Astanovitskiy, Vidya Nalajala, Oleg Dmitriev, and Oleksandr Chalyy, and the machine shop staff, Wade Cline, Carl Davidson, Dennis Meredith, and Walt Weaver, for their assistance. I would like to acknowledge, also, my friends and family.

Financial support for this work is gratefully acknowledged under a Cooperative Agreement between the U.S. Department of Energy NNSA and UNR NTF (DE-NA0002075), from the Nevada Governor's Office of Economic Development, and from Mission Support and Test Services, LLC.

Contents

List of Tables

List of Figures

Chapter 1

Introduction

Laser ablation is the physical process of creating a plume of material from a target irradiated by a laser. Ablation is any process which removes material from a target. Ablation comes from the Latin word “ablatio” meaning “removal” or “taking away.” Laser ablation leads to the emission of material as a vapor, a gas, and/or a plasma. Lasers, first theorized by Schawlow and Townes in 1958, did not exist in operational form until first demonstrated by Maiman in 1960 [1, 2]. LASER, or Light Amplification by Stimulated Emission of Radiation, owes its name to Gordon Gould, who independently developed the concept of lasing [3]. The study of high-power laser pulses interacting with matter began with the development of the first pulsed lasers in the early 1960’s [4, 5].

The processes of laser ablation and desorption have been intensively studied to better understand the fundamental processes at work and to improve the application of laser ablation to science and to industry. Descriptions of the basic theory of laser ablation can be found in a number of sources [6–10]. Laser ablation spans a wide array of topics in physics and finds applicability in fields as diverse as electronics, propulsion, fusion research, and chemical analysis. The subject of pulsed laser ablation (PLA) has grown to include many books and journal articles describing the process and its applications.

1.1 Laser Ablation: The Process

The removal of material during PLA occurs as the result of heating matter at the location where the laser intersects the target. Continuous wave (CW) lasers can also heat the target and evaporate material. A practical application of CW lasers is cutting through materials. CO_2 gas lasers are often used for this purpose because they are able to deliver high power CW output.

Laser pulsing is desirable in order to increase the peak power deposited onto a target. Q-switch lasers are capable of delivering laser pulses on the nanosecond (ns) scale. Solid state lasers with a modest energy output in the range of tens of millijoules per pulse can generate tens of megawatts of power output. A target will heat, melt, and vaporize when this amount of energy is deposited onto a small area that is often less than 1 cm in diameter. Nonlinear and multiphoton processes occur at these fluences, and some of the removed material will be in the plasma state [11].

Material that has been ablated expands into either a vacuum or a background gas. The plume rapidly cools and decreases in density due to its free expansion in vacuum; in contrast, a shock wave is launched into the gas with the expanding material following behind when the plume expands into a background gas. The velocity of the expanding plume decreases as the gas pressure increases. Material in this plume includes neutral and ionized atomic and molecular species, and free electrons. This material is hot and emits light so that it can be measured with optical instruments including cameras and spectrometers. Droplets of condensed target material are observed to boil off tens of microseconds later [12, 13].

Laser parameters, including laser pulse energy, temporal pulse width, focus size on target, and wavelength, play a critical role in the development of the plume. Eq.

(1.1) describes an important quantification for laser parameters.

$$Intensity[W/cm^2] = \frac{Energy[J]}{Time[s] * Area[cm^2]} \tag{1.1}$$

The laser wavelength determines how the laser light couples to the material. Shorter wavelengths are better at breaking the interatomic bonds of the solid target. Longer wavelengths couple more efficiently to the phonon spectrum of the solid. Other important laser quantities that can affect PLA include the polarization and the laser repetition rate [14].

A threshold intensity exists for laser ablation. This threshold is dependent on the target material and is in the $10^7 - 10^8$ W/cm^2 region. Most table-top nanosecond scale pulsed lasers operate in the $10^8 - 10^{14}$ W/cm^2 regime, and larger systems can reach up to 10^{16} W/cm^2. Femtosecond laser systems can reach up to 10^{22} W/cm^2. Laser intensity increases dramatically when the pulse length is reduced from the nanosecond regime to the femtosecond regime as is shown in Eq. (1.1).

Nanosecond (10^{-9} s), picosecond (10^{-12} s), and femtosecond (10^{-15} s) laser pulses each have distinct effects on targets. Nanosecond laser pulses produce rapid melting and evaporation of the material off of the target. Collisions and, in some instances, multiphoton processes lead to ionization of the material producing a plasma. Femtosecond pulses primarily drive multiphoton ionization of the atoms leading to a large degree of ionization. Material is removed from the target due to the resulting Coulomb explosion. A Coulomb explosion results from the repulsion of like charged ions.

1.2 Plasmas and Warm Dense Matter

One important result of laser ablation is the production of plasma. A plasma is an ionized gas consisting of a mixture of unbound positive ions and negative electrons. Plasmas are found widely throughout the universe but are rarely found naturally on Earth. A couple of notable examples include lightning discharges and the Aurora Borealis and Aurora Australis. Lightning is a plasma confined by the magnetic field produced as the current passes through a column of ionized air. The plasma in the aurora exists at a much lower density and results from electrons (protons also produce a faint aurora) from the sun entering the magnetic field lines produced by the dynamo motion of the molten core of the earth. These fields are called the Van Allen belts and direct the protons to the poles where they enter Earth's atmosphere and ionize atoms and molecules in the atmosphere. The green color in the aurora is a result of ionized N_2. The next plasma beyond the Earth is the Sun. Plasmas ranging from low temperature and low density to high temperature and high density are found beyond our solar system.

Material ablated from a target using sufficient laser energy will be partially or fully ionized. The ionization is due to photon-electron interactions and electron-electron collisions. This plasma state is of interest because of its application in high energy density plasma (HEDP) and warm dense matter (WDM) research. Plasmas may fall into the category of warm dense matter if the density and temperature are sufficiently high. Warm dense matter is a plasma regime which exists between traditional condensed matter physics and traditional plasma physics. Temperatures range from 0.1-100 eV, and the density equals or exceeds solid density [15]. This is the state space regime in which planet interiors and inertial confinement fusion compression reside.

1.3 Applications of Pulsed Laser Ablation

A multitude of applications of laser ablation are currently in use. Intensive research has been carried out to study the use of laser ablation for depositing thin films onto substrates in the electronics industry since the mid-1980's. A survey of the available literature describing PLA shows a large number of papers devoted to the properties of the materials deposited onto a substrate by a plume [14]. A further survey of the literature shows that laser ablation appears in chemical analysis techniques, plasma physics, laboratory astrophysics, spacecraft propulsion, and medical applications such as removing tissue [16]. PLA is also used to produce ions used in other research. These applications are discussed in more detail below.

1.3.1 Thin Film Production

One early application of laser ablation was applied in materials science. Micromachining and thin film deposition, called pulsed laser deposition (PLD), are both applications in which laser ablation has been applied [14, 17–19]. Thin film deposition and growth on substrates using PLA is now used for many different types of materials including conductors, dielectrics, metals, semiconductors, and superconductors [14]. This diversity makes PLD a more versatile technique than others deposition techniques, such as evaporative deposition. PLD produces thin films that are identical to the bulk material from which they were produced with high purity. Typical nanosecond laser pulses will not produce atomic species in the plume with kinetic or neutralization energies large enough to damage the film substrate. The substrate can be biased to allow or reject certain ion energies. Gases can be added to the ablation environment to change the film chemistry or to thermalize the plasma in the plume. Combining PLA with background gases is useful for producing nanoparticulates [14, 20].

1.3.2 Propulsion

Spacecraft propulsion has been investigated as an application for laser ablation for over forty years [21]. The most basic design for this type of propulsion uses a pulsed laser to ablate a target fuel such as Teflon. That plume is then directed out through a nozzle [22]. Newton's Third Law guarantees an equal and opposite reaction force to the force of the expanding plume which generates thrust. Pulsed lasers are preferred to CW lasers due to the large power needed to achieve the required specific impulse. Technical challenges remain in deploying this type of system, but significant work has been done in this area of research. Spacecraft size and the thrust requirements for traditional satellites are too great for current lasers.

One particularly interesting direction for laser ablation-based thrust schemes is the propulsion of microsatellites and nanosatellites. CubeSats are one example [23]. These small and lightweight spacecraft (1-100 kg) provide an arena in which a laser ablation thruster might be useful. CubeSats are designed to the standard dimensions of 10 cm × 10 cm × 10 cm. These standard dimensions are designated as "U", and CubeSats are built in the sizes 1U, 2U, 3U, and 6U. Each of these designs weighs less than three pounds [24, 25]. A current limitation for CubeSats is the need for novel propulsion systems [23]. CubeSats generally use deployable solar panels to power the onboard instruments and propulsion. Laser ablation propulsion would be used once the system is in orbit because CubeSats are currently launched with larger payloads. The power requirements for propulsion are far less once the satellite is in orbit. Small diode lasers, with their low power consumption requirements, would then be ideal candidates for generating laser ablation plumes.

1.3.3 LIBS and LAMIS

Laser Induced Breakdown Spectroscopy (LIBS) provides an important and useful tool to analytical chemistry [26–28]. LIBS can quickly provide an elemental identification of a small sample material in a non-destructive testing method. A LIBS sample is irradiated with a pulsed laser, and the resulting plume is studied using optical spectroscopy. LIBS requires no sample preparation and is minimally destructive when compared to many other analytical techniques. Ablating the sample ensures that the sample is atomized. Many of the same quantities that are important in the study of the plasma formed at early times in the plume are also important for LIBS. Quantification of electron temperature and electron density are needed to properly analyze the spectrum that is produced.

Challenges in the study of LIBS plasmas are similar to those experienced by all laser ablation research. The plasma formed in the first 100 nanoseconds is composed of atomic species which are usually partially ionized. Chemical reactions can occur as the plasma expands, cools, and becomes neutral. The condition of Local Thermodynamic Equilibrium (LTE) is often imposed on these plasmas to make the modeling and analysis of the data possible. A rapidly expanding plasma is not strictly in thermodynamic equilibrium. The condition of LTE can be imposed on these plasmas as the plume expands and slows down. LTE is valid when densities remain high and the characteristic times for hydrodynamic flow become greater than the characteristic time for chemical reactions [28]. The condition of LTE generally occurs at times greater than 100 nanoseconds after laser irradiation. Many LIBS systems insert a delay between target irradiation and collecting data with the spectrometer to avoid the early non-equilibrium plasma.

Laser Ablation Molecular Isotopic Spectroscopy (LAMIS) is a subset of LIBS that allows for the measurement of isotope abundance by looking at the energy shift of non-homopolar diatomic molecular spectra caused by the change in mass of one or both of the atoms [29–31]. The isotopic shift of the spectra is greater for molecular species than it is for atomic species. Most isotope measurements are made using mass spectroscopy. LAMIS does not require sample preparation, is minimally destructive, and any type of target that can be ablated can be analyzed. This technique has been used on elements such as hydrogen, boron, carbon, nitrogen, oxygen, chlorine, strontium, and zirconium [31, 32]. Work has extended to femtosecond lasers to help improve atomization and isotopic equilibration to provide greater accuracy. Experiments have also been carried out to test the ability to make measurements from various distances [31].

1.3.4 Inertial Confinement Fusion

Inertial confinement fusion is a fusion scheme which uses lasers to compress a spherical deuterium-tritium (D-T) target in order to meet the Lawson criteria for fusion. The target is composed of D-T surrounded by a plastic ablator. Two different approaches are being researched. The first uses direct drive confinement and has been researched at the University of Rochester and the Jupiter Laser Facility at Lawrence Livermore National Lab. A large number of separate laser beams are focused directly onto the spherical target from all directions in this approach. Ablation of the ablator generates an equal and opposite force which compresses the target to attempt to achieve a density greater than Lawson's criteria. The second approach uses an indirect drive method. This method focuses the laser beams onto a hohlraum. The hohlraum is a small cylinder that the target sphere sits in and is made of a heavy metal, such as gold. X-rays are produced when the lasers interact with the hohlraum. These x-rays then impinge on the spherical target and ablate the plastic producing the necessary compression [33].

1.3.5 Astrophysical Applications

Many natural processes can be simulated by laser ablation. Expanding laser ablation plumes provide a platform for simulating the magnetohydrodynamic and hydrodynamic phenomena found in astrophysical systems. Many of these astrophysical systems fall into the HEDP area of physics. Examples of astrophysical systems that can be studied in laser ablation experiments include supernova hydrodynamics, protostellar jet dynamics, and photoionized plasmas [34]. Instability formation and high Mach number flows are additional areas of interest for astrophysics research [35]. Astrophysical phenomena outside of the HEDP regime can also be researched with pulsed laser ablation. Chemical reactions produced by a hot jet of material expanding into a cooler background gas are important for stellar chemistry.

1.4 LAPeX

This dissertation will describe the development and initial experimental investigations of the LAPeX apparatus. Chapter 2 of this dissertation will develop the theory necessary to understand and analyze the data collected with this apparatus. Topics covered include the interaction of lasers with solids, basic plasma physics and kinetics, and atomic and molecular spectroscopy. Chapter 3 describes the LAPeX apparatus in detail. Descriptions of the lasers and diagnostics in the experimental apparatus are provided. A discussion of the process used to calibrate the spectroscopic systems is included in Chapter 3. Chapter 4 describes an experiment which explored the use of a supercontinuum laser for absorption spectroscopy of diatomic carbon in an ablation plume. The production of TiO from the ablation of titanium into a rarefied oxygen atmosphere is described in Chapter 5. Conclusions are discussed in Chapter 6.

Chapter 2

Theory

Pulsed laser ablation is a process which requires the theoretical input from a number of different subjects within Physics. The subjects of Plasma Physics, Atomic, Molecular, and Optical Physics, Solid State and Condensed Matter Physics, Thermodynamics, and Quantum Theory contribute to laser ablation. An understanding of the contributions from these different areas of Physics is necessary to fully understand laser ablation. An extensive theoretical treatment of laser ablation has been produced over the last fifty years. An introduction to the theoretical principles necessary to understand the work completed for this dissertation is presented in this chapter.

2.1 Laser Parameters

Laser parameters play an important role in many of the characteristics of the laser ablation plume. Laser parameters, including the laser wavelength (λ), pulse duration (τ), energy (E_l), and target focal diameter (D_f), define the final photon beam on target. Many of the effects resulting from the pulsed laser interacting with the target material are dependent on these laser pulse characteristics. Some of these parameters are fixed, while others can be varied, depending upon the laser and the experimental setup. Three quantities of interest can be generated from these parameters. These quantities are laser power, P, (Eq. (2.1)), laser fluence, Fl, (Eq. (2.2)), and laser intensity, I, (Eq. (2.3)) and are given by:

$$P = \frac{E_L}{\tau}, \tag{2.1}$$

$$Fl = \frac{E_L}{D_f}, \tag{2.2}$$

$$I = \frac{P}{D_f}.. \tag{2.3}$$

An understanding of basic laser physics is necessary to fully understand laser ablation. Lasers have the important quality of producing coherent and monochromatic light. Light emitted from a laser has a very narrow wavelength (energy) spread and is in phase. Light, as with any electromagnetic wave, can be viewed as either composed of particles (photons) or waves. These two views are equivalent, and the choice of which position to take is motivated by the particular physical process that is described. The electric and magnetic fields oscillate in the wave description of light. Electromagnetic waves are composed of perpendicular oscillating electric and magnetic fields. Eqs. (2.4) and (2.5) show the amplitudes of an electric and magnetic field [36]:

$$\mathbf{E} = \mathbf{E_0} \exp i(\frac{2\pi z}{\lambda - \omega t}), \tag{2.4}$$

$$\mathbf{H_0} = n\epsilon c\mathbf{E_0}. \tag{2.5}$$

E_0 is the electric field amplitude, H_0 is the magnetic field amplitude, z is the position along the propagation axis, λ is the wavelength, ω is the angular frequency, c is the

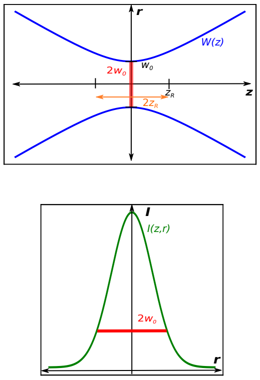

Figure 2.1 This figure shows a Gaussian profile with the beam waist W_0, the Rayleigh Length z_R, and the beam radius W(z).

speed of light, and n is the index of refraction (c/ν or $\sqrt{\epsilon\mu}$). Laser irradiance is an important quantity in the study of laser ablation. The irradiance is given by Eq. (2.6):

$$I = |\mathbf{E} \times \mathbf{H}| = n_1 \epsilon_0 c \mathbf{E_0}^2. \tag{2.6}$$

The irradiance has units of energy per unit time per unit area, or power per unit area. The most common units used are W/cm^2. Irradiance is also referred to as "laser flux density" or "intensity" in the literature (see Eq. (2.3)). Intensity provides an accurate definition of the laser properties because it includes all of the laser parameters except for wavelength.

The typical spatial and temporal profile for a pulsed laser is a Gaussian profile. Other profile functions may be produced for specialized applications with additional optical components, but a Gaussian profile is naturally produced by the laser. The spatial intensity profile of a Gaussian beam is [37, 38]:

$$I(r,z) = \frac{2P}{\pi W^2(z)} exp\left[-\frac{2r^2}{W^2(z)}\right], \tag{2.7}$$

and,

$$P = \frac{1}{2} I_0 (\pi W_0^2), \tag{2.8}$$

$$W(z) = W_0 \left[1 + \left(\frac{z}{z_0} \right)^2 \right]^{\frac{1}{2}}. \tag{2.9}$$

P is the total power of the beam, and W(z) is the beam radius. W_0 is the beam waist given by:

$$W_0 = \left(\frac{\lambda z_0}{\pi} \right)^{1/2}. \tag{2.10}$$

2.2 Lasers Interacting with Matter

Laser ablation is often modeled in the adiabatic limiting condition. This condition requires that the light absorption, heating, melting, and vaporization occur much faster than the ablation plume expands [39]. This adiabatic approximation greatly simplifies the analytical and numerical analysis of laser ablation. The adiabatic approximation reduces the ablation process to two separate events. The first event occurs when the laser energy is absorbed and converted to internal energy in the target and vapor. The second event occurs when internal energy evolves to kinetic energy in the expanding plume. The leading edge of the laser pulse produces a thin vapor that is essentially transparent to the remaining laser pulse in low laser intensity cases. In contrast, the leading edge of the laser pulse produces a vapor with atomic excitations and ionization when the fluence is large enough. This vapor becomes a plasma and absorbs light which shields the target from the remaining laser pulse. Laser plasma coupling and plasma kinetics dominate at this stage.

The temporal pulse width of the laser greatly influences the mechanisms responsible for ablation. Two commonly used pulse durations have the temporal lengths of the nanosecond (10^{-9} s) and femtosecond (10^{-15} s) scale. Thermal processes dominate the production of an ablation plume when a nanosecond pulse irradiates a target. Atoms can be fully stripped of electrons resulting in a Coulomb explosion for a femtosecond pulse.

A material's response to laser light is defined by rearranging Eq. (2.6) [14]:

$$E_0 = \left(\frac{2I}{cn\epsilon_0}\right)^{1/2}. \tag{2.11}$$

E_0 is the electric field amplitude, I is the power density, n is the index of refraction, and ϵ_0 is the permittivity of free space. Laser light is absorbed in metal targets by the free electrons in the Fermi gas due to the inverse bremsstrahlung process. Electrons from the Fermi gas are promoted to higher energy states and re-thermalize by colliding with other electrons and phonons in the crystal lattice of the metal, resulting in heat transfer [6,40].

The absorption coefficient is defined as:

$$\alpha = -\frac{1}{I}\frac{dI}{dz} = \frac{2\omega n_2}{c} = \frac{4\pi n_2}{\lambda}. \tag{2.12}$$

The quantity $1/\alpha$ is the absorption depth. The absorption depth is the depth that an electromagnetic wave will penetrate in a material. Eq. (2.12) states that the absorption depth is proportional to λ. Longer wavelengths in the infrared will penetrate deeper into the target than shorter wavelengths in the visible and UV.

A classical approach to heat transfer can be applied to understand the movement of heat in the target during irradiation. Eq. (2.13) gives the three-dimensional partial differential heat flow equation [6]:

$$\nabla^2 T(x,y,z,t) - \frac{1}{\kappa}\frac{\partial T(x,y,z,t)}{\partial t} = \frac{-A(x,y,z,t)}{k}. \tag{2.13}$$

T is the temperature, κ is the thermal diffusivity, k is the thermal conductivity, and A is the heat production per unit volume per unit time. The initial condition for this equation is $T(x, y, z, 0) = 0$. Boundary conditions are described as $T \to 0$ as $z \to \infty$ and $T = 0$ at $z \leq 0$.

Equation (2.13) can be simplified to a one-dimensional differential equation. This simplification is justified because the transverse dimension (x, y coordinates) of the laser is much greater than the depth (z coordinate) that heat travels during the laser pulse [6]. The term $A(x, y, z, t)$ is reduced to $A(z, t)$ and is defined as:

$$A(z,t) \cong (1-R)I(t)(1/\delta)e^{-z/\delta} \approx \alpha(1-R)I(t)e^{-\alpha z}. \tag{2.14}$$

R is the reflectivity of the target surface, and $I(t)$ is the laser intensity as a function of time. The absorbance is defined as: $A = 1 - R$. The electric field penetration depth is δ, and the skin depth is δ'. These quantities are related in the following way:

$$\delta = \delta'/2 = c/2\omega(-\epsilon)^{(1/2)}. \tag{2.15}$$

The speed of light is c, ω is the angular frequency of the incident light, and ϵ is the permitivity of the material. The one-dimensional heat flow equation is given by:

$$\rho c \frac{\partial T}{\partial t} = \frac{\partial T}{\partial z}\left(k\frac{\partial T}{\partial z}\right) + \alpha A I(t)e^{-\alpha z}. \tag{2.16}$$

T is the temperature, ρ is the material density, t is time, and z is the direction of flow normal to the target surface. The quantity, α, is large for most metals ($10^5 - 10^6$ cm^{-1}). A laser beam with a Gaussian profile, $I(R) = I_0 exp(-r^2/d^2)$, will produce a laser spot on the target with absorption profiles given by [6]:

$$F(r) = AI_0 exp(-r^2/d^2), \tag{2.17}$$

$$F(t) = AI(t). \tag{2.18}$$

The solution to the heat transfer equation for a spot with a Gaussian profile is [6]:

$$T(r,z,t) = \frac{F_{max}d^2}{k}\left(\frac{\kappa}{\pi}\right)^{1/2}\int_0^t \frac{p(t-t')dt'}{t^{1/2}(4\kappa t'+d^2)} exp\left[-\frac{z^2}{4\kappa t^2} - \frac{r^2}{4\kappa t' + d^2}\right]. \tag{2.19}$$

The function, $p(t)$, is defined as:

$$p(t) = F(t)/F_{max}. \tag{2.20}$$

F_{max} is the value for the maximum absorbed energy at the center of the laser spot when $F(t)$ is at a maximum. The Gaussian beam radius is d.

Energy transport into a metal can be described by the following equations which are similar to Eq. (2.16) [40]:

$$C_e\frac{\partial T_e}{\partial t} = -\frac{\partial Q(z)}{\partial z} - \gamma(T_e - T_i) + S, \tag{2.21}$$

$$C_i\frac{\partial T_i}{\partial t} = \gamma(T_e - T_i), \tag{2.22}$$

$$Q(z) = -k_e\frac{\partial T_e}{\partial z}, \tag{2.23}$$

$$S = I(t)A\alpha \exp -\alpha z. \tag{2.24}$$

T_e and T_i are the electron and lattice temperatures, respectively. C_e and C_i are the heat capacities of the electron and lattice systems, respectively. $Q(z)$ describes the heat flux, and z is the direction perpendicular to the target surface. The coupling of the electron-lattice system is characterized by γ, S is a laser heating source term, and $I(t)$ is the laser intensity. Electron thermal conductivity is k_e, $A = 1 - R$ is the surface transmissivity (absorbance), and α is the material absorption coefficient [40].

Three timescales are associated with the heat transfer process:

$$Electron\ \ Cooling\ \ Time : \tau_e = \frac{C_e}{\gamma}, \tag{2.25}$$

$$Lattice\ \ Heating\ \ Time : \tau_i = \frac{C_i}{\gamma}, \tag{2.26}$$

$$Laser\ \ Pulse\ \ Duration : \tau_L. \tag{2.27}$$

Femtosecond laser pulses are characterized by $\tau_L \ll \tau_e, \tau_i$, and picosecond pulses are characterized by $\tau_e \ll \tau_L \ll \tau_i$ [40]. Different degrees of equilibrium are established between the electrons and the lattice at these time scales. The phase transition from solid to vapor is direct for short laser pulses [39]. The absorption of a nanosecond laser pulse is characterized by the condition $\tau_L \gg \tau_i$, and the electron and lattice temperatures are equal, $T_e = T_i = T$. Eqs. (2.21)-(2.23) reduce to:

$$C_i \frac{\partial T}{\partial t} = \frac{\partial}{\partial z}\left(k_0 \frac{\partial T}{\partial z}\right) + I_a \alpha \exp(-\alpha z). \tag{2.28}$$

Eq.(2.28) is equivalent to Eq. (2.16). Metal melts, then vaporizes, when a nanosecond laser pulse is absorbed. Heat is conducted into the material as described by the heat penetration depth, l, and the heat diffusion constant, D [39]:

$$l \sim (Dt)^{\frac{1}{2}}, \tag{2.29}$$

$$D = \frac{k_0}{C_i}. \tag{2.30}$$

$$\tag{2.31}$$

The heat penetration depth, l, describes the depth that the energy from the laser pulse is absorbed from the propagating heat wave, and $l \gg \alpha^{-1}$.

Nanosecond scale laser pulses are long enough that they typically meet the condition: $D\tau_L\alpha^2 \gg 1$. The total energy deposited into the target is: $E \sim (I_a t)/(\rho l)$. The threshold time, t_{th}, measures the time before the energy deposited by the laser becomes larger than the specific heat of vaporization, C_{vap}. Evaporation then becomes the dominant process. The intensity and fluence thresholds are defined by Eqs. (2.32) and (2.33), respectively, when $E_m > C_{vap}$ ($\tau_L > t_{th}$) [40]:

$$I > I_{th} \sim \frac{\rho C_{vap} D^{0.5}}{\tau_L^{0.5}}, \tag{2.32}$$

$$F > F_{th} \sim \rho C_{vap} D^{0.5} \times \tau_L^{0.5}. \tag{2.33}$$

Another way to show the threshold fluence is [39]:

$$F_{th} \approx \frac{\rho c \Delta T_m L_{th}}{A}. \tag{2.34}$$

$\Delta T_m = T_m - T_0$ where T_m and T_0 are the melting and initial target temperatures, respectively. The fluence threshold increases as $\tau_L^{1/2}$.

Charge is emitted from the laser irradiated target in the form of electrons and ions. Electrons are ejected from the surface of the target by two mechanisms. Thermionic electron emission is the first mechanism. The target material's work function, ϕ, is overcome, and electrons are emitted as the temperature at the surface of the target is increased. Richardson's equation describes the current density emitted by the target [6]:

$$j = AT^2 exp(-\phi/kT). \tag{2.35}$$

A is a constant equal to 60.2 A$\cdot$cm^{-2}deg^{-2}, T is the target surface temperature, ϕ is the target's work function, and k is the Boltzmann constant. Eq. (2.35) shows that the current scales as the square of the target surface temperature.

The second mechanism responsible for electron emission involves multiphoton processes. Multiple photons are simultaneously absorbed by an electron. This absorption allows the electron to gain enough energy to overcome its work function, ϕ. Thermionic emission dominates the electron current for laser intensities greater than 10^8 W/cm^2. The current generated by multiphoton processes may be equal to, or greater than, the current generated by thermionic emission for $I \leq 10^8$ W/cm^2 [6].

Positive charge emission follows electron emission. Positive ions emitted by thermionic emission are observed later than electron emission (100 ns - 10 μs) because the ions are more massive than electrons. An equation similar to Eq. (2.35) can be stated for ion emission [6]:

$$j_+ = A_p T^2 exp(-\phi_p/kT). \tag{2.36}$$

A different work function, ϕ_p, is used for ions:

$$\phi_p = I + \phi_0 - \phi. \tag{2.37}$$

Eq. (2.37) provides the relationship between a quantity defined as the positive work function, ϕ_+, the electron work function, ϕ, the ionization potential, I, and the energy required to remove a neutral molecule, ϕ_0.

Evaporation rates for the neutral vapor are given by the Clausius–Clapeyron equation [39]. The production of a plasma is observed at intensities greater than $10^8 - 10^9$ W/cm^2. This plasma is a mixture of electrons and ions. Absorption of light in the plasma occurs due to two processes. Inverse bremsstrahlung applies to the free electrons in the plasma. These free electrons absorb photons according to the absorption coefficient in Eq. (2.38) [39, 41]:

$$\alpha_{IB} = \sigma_{IB} N_e = \frac{4}{3}\left(\frac{2\pi}{3k_B T_3}\right)^{1/2} \frac{Z^2 e^6}{hcm_e^{3/2}\nu^3} N_i g_{ff}\left[1 - \exp\left(-\frac{h\nu}{k_B T_e}\right)\right] N_e. \tag{2.38}$$

The cross section for inverse bremsstrahlung is σ_{IB}, N_e is the electron number density, h is Planck's constant, ν is the frequency of the light, c is the speed of light, m_e is the mass of the electron, N_i is the ion number density, and g_{ff} is the Gaunt factor. Light is also absorbed in the plasma by photoionization. Photons from the laser beam ionize atoms in the plasma. The absorption coefficient for photoionization is [39, 41]:

$$\alpha_{PI} = \sigma_{PI} N_n \approx \sum_n 2.9 \times 10^{-17} \frac{(\epsilon_n)^{5/2}}{(h\nu)^3} N_n. \tag{2.39}$$

The cross section for photoionization is σ_{PI}, N_n is the number density of the excited state, and ϵ_n is the ionization energy. The lifetime of the plasma depends on the amount of laser energy deposited on the target [42].

2.3 Plasmas

2.3.1 Basic Plasma Definitions and Quantities

A development of some of the central theory of plasmas is necessary to understand the early stages of PLA. The discussion here is based on several texts [43–46]. Plasmas contain positively charged ions, negatively charged electrons, and, in some cases, neutral atoms and molecules. Negative ions may also be present. The total charge of a plasma is neutral, but a plasma has a large number of individual charges:

$$\sum_i q_i n_i - q_e n_e = 0, \tag{2.40}$$

or,

$$\sum_i q_i n_i = q_e n_e. \tag{2.41}$$

The ion density, n_i, in a charge state, q_i, is equal to the electron density, n_e, multiplied by the charge of the electron, q_e. The density of ions from a given atomic species and charge state may not be equal to the density of other ions or electrons. Plasma can be viewed as a fluid that is not only governed by hydrodynamic equations, but also by magnetohydrodynamic (MHD) equations because it is an ionized gas. The particles in a plasma exhibit a Maxwellian velocity distribution when in thermodynamic equilibrium. Eq. (2.42) defines a Maxwellian velocity distribution:

$$f(v) = Av^2 \left(\frac{m}{2\pi k_B T}\right)^{3/2} exp\left(-\frac{mv^2}{2k_B T}\right), \tag{2.42}$$

where A is a normalization constant, m is the particle's mass, k_B is Boltzmann's constant, and T is the temperature.

Charges in a plasma will move to neutralize a charged object inserted into it. Electrons will move towards a positively charged object and away from a negatively charged object, leaving the positively charged ions behind. The charges in the plasma will create a thin sheath that will shield the charged object. The thickness of this sheath is called the Debye length:

$$\lambda_D \equiv \left(\frac{\epsilon_0 K T_e}{ne^2}\right)^{1/2}. \tag{2.43}$$

Plasmas have the unique feature that their charged particles can interact over a longer range than a neutral gas due to the Coulomb force. The atoms and molecules in a neutral gas interact primarily through collisions. A Maxwellian distribution can be applied to systems with spatial dimensions much larger than the mean free path of neutral particles, and times much longer than the collision time between particles.

The gas is thermalized, and kinetic theory can provide the pressure and temperature under these conditions. The Maxwellian distribution is reached more slowly in a plasma than in a neutral gas because particle collision times are greater. Many plasma processes occur on time scales shorter than the thermalization time [46].

The most fundamental description of plasmas comes from kinetic theory, in which each particle's position and velocity are defined in a six-dimensional phase space distribution function, $f(\mathbf{x}, \mathbf{v}, t)$. Equation (2.44) gives the density of particles from that function:

$$n(\mathbf{x}, t) = \int_{-\infty}^{\infty} f(\mathbf{x}, \mathbf{v}, t) d^3 v. \tag{2.44}$$

The distribution function, $f(\mathbf{x}, \mathbf{v}, t)$, can be used to calculate macroscopic quantities. The density of the plasma, $n(\mathbf{x}, t)$, is called the zero-order moment of the function f, the velocity, $u(\mathbf{x}, t)$, is the first-order moment, and the second-order moment gives the mean particle energy. The Vlasov equation plays an important role in the kinetic description of plasmas. Inserting the Lorentz force,

$$\mathbf{F} = q(\mathbf{E} + \mathbf{v} \times \mathbf{B}), \tag{2.45}$$

into the collisionless Boltzmann equation,

$$\frac{\partial f}{\partial t} + \mathbf{v} \cdot \frac{\partial f}{\partial \mathbf{x}} + \frac{\mathbf{F}}{m} \frac{\partial f}{\partial \mathbf{v}} = 0, \tag{2.46}$$

generates Eq. (2.47), the collisionless Vlasov equation:

$$\frac{\partial f}{\partial t} + \mathbf{v} \cdot \frac{\partial f}{\partial \mathbf{x}} + \frac{q}{m} (\mathbf{E} + \mathbf{v} \times \mathbf{B}) \cdot \frac{\partial f}{\partial \mathbf{v}} = 0. \tag{2.47}$$

An additional term, $\left(\frac{\partial f}{\partial t}\right)_C$, is needed to describe a collisional plasma:

$$\frac{\partial f}{\partial t} + \mathbf{v}\cdot\frac{\partial f}{\partial \mathbf{x}} + \frac{q}{m}(\mathbf{E} + \mathbf{v}\times\mathbf{B}) \cdot \frac{\partial f}{\partial \mathbf{v}} = \left(\frac{\partial f}{\partial t}\right)_C. \tag{2.48}$$

The Krook collision term, $\left(\frac{\partial f}{\partial t}\right)_C$, is defined as:

$$\left(\frac{\partial f}{\partial t}\right)_C = -\frac{f - f_m}{\tau}. \tag{2.49}$$

The Maxwellian distribution function, f_m, is the distribution that the system is moving towards, and τ is the mean collision time. The Fokker-Planck equation may replace the Krook collision term in fully ionized plasmas.

The zero-order moment of the Vlasov equation (Eq. (2.48)) yields the continuity equation, which conserves the particle number:

$$\frac{\partial n}{\partial t} + \frac{\partial}{\partial \mathbf{x}} \cdot (n\mathbf{u}) = 0. \tag{2.50}$$

The first-order moment gives the force balance equation,

$$mn\left[\frac{\partial \mathbf{u}}{\partial t} + (\mathbf{u}\cdot\nabla)\mathbf{u}\right] = qn(\mathbf{E} + \mathbf{u}\times\mathbf{B}) - \nabla\cdot\mathbf{P} + \mathbf{P}_{ij}, \tag{2.51}$$

where $\mathbf{P}$ is the pressure tensor. The second-order moment generates the adiabatic equation of state, which describes the conservation of energy as:

$$\frac{p}{\rho^\gamma} = constant. \tag{2.52}$$

The scalar pressure is p, ρ is the mass density, and γ is the adiabatic index.

2.3.2 Thermodynamic Equilibrium Conditions

A full understanding of the kinetic description of all direct and inverse collisional and photo processes, and their reaction rates, is required to give an accurate description of the atomic and ionic electron energy levels, the molecular vibrational and rotational energy levels, and the free electron energy levels in a plasma [47]. Thermodynamic quantities are preferable to the use of a full kinetic description of a system with a large number of particles. The problem of completely describing all particles in the plasma in phase space, N particles $\times$ 6 parameters, is reduced to a few quantities including temperature and density by using thermodynamic quantities.

Thermal equilibrium is required for a proper thermodynamic description of the plasma. Thermal equilibrium requires that the particle velocities and energies have a statistical distribution which follows the Maxwell-Boltzmann distribution. This equilibrium is critically important for the interpretation of spectroscopic data. The intensity of emission lines is tied to the atomic state distribution among energy levels and the charge state distribution [48]. The kinetic energy distribution of the electrons is defined by the electron energy distribution function (EEDF), which depends on spectral emission given by a system in equilibrium. Laboratory plasmas are rarely in full thermodynamic equilibrium (TE) because of their transient nature. Laser induced plasmas are not only transient in time, but these plasmas also tend to be inhomogeneous.

Electron-electron elastic collisions are efficient, and the Maxwellian EEDF holds for most of the expansion, resulting in a condition known as Local Thermodynamic Equilibrium (LTE). Inelastic collisions between electrons and atoms/ions generate a Boltzmann distribution with the same temperature as the EEDF when the plasma is in LTE [42]. Electron impact ionization and three body recombination are the primary atomic processes for most of the plume's expansion.

The McWhirter criteria must be met in order for LTE to be assumed [42]:

$$n_e > 1.6 \times 10^{12}\sqrt{T_e} \cdot \Delta E_{ul}^3. \tag{2.53}$$

Collisional excitation and de-excitation occur approximately ten times faster than radiative excitation and de-excitation if the McWhirter criteria is met [42]. Spectral line intensity is given by Eq. (2.54) if the plasma is in LTE [42]:

$$I_{ul} = \frac{1}{4\pi} A_{ul} h \nu_{ul} N_u. \tag{2.54}$$

The line transition energy is included in Eq. (2.53). A plasma in which the McWhirter criteria is satisfied for only certain atomic transitions is possible. A plasma with these characteristics is considered to be in partial LTE (pLTE). A plasma in pLTE no longer has a Maxwellian EEDF or heavy particle Boltzmann distribution [42].

2.4 Thermodynamics and Fluid Dynamics of Ablation Plumes

Fluid Dynamics describes the plume for much of its duration. The plume behaves like a ballistic fluid when it expands into vacuum. A shock wave often precedes the expansion of the plume when it expands into a background gas. Eqs. (2.55), (2.56), and (2.57) describe the flow of the plume [46]:

$$Continuity\ \ Equation: \ \frac{\partial \rho}{\partial t} + \frac{\partial}{\partial x}(\rho u) = 0, \tag{2.55}$$

$$Euler\ \ Equation: \ \frac{\partial u}{\partial t} + u\frac{\partial u}{\partial x} + \frac{1}{\rho}\frac{\partial p}{\partial x} = 0, \tag{2.56}$$

$$Energy\ \ Equation: \ \rho\frac{\partial E_i}{\partial t} + \rho u\frac{\partial E_i}{\partial x} + p\frac{\partial u}{\partial x} = \frac{\partial \Phi}{\partial x}. \tag{2.57}$$

The mass density is ρ, p is the pressure, E_i is the internal energy, and Φ is the laser intensity. The equation of state for a perfect gas is needed to complete the fluid flow equations:

$$p = nk_BT = \frac{\rho k_B T}{m} = \frac{\rho a^2}{\gamma}. \tag{2.58}$$

A shock wave can be described by equations (2.59), (2.60), and (2.61). One of the primary characteristics of a shock wave is the discontinuity of fluid properties across the shock. Eqs. (2.59), (2.60), and (2.61) describe the conditions in front of and behind the shock:

$$Continuity : \rho_1 u_1 = \rho_2 u_2, \tag{2.59}$$

$$x - momentum : p_1 - p_2 = \rho_2 u_2^2 - \rho_1^2, \tag{2.60}$$

$$Energy : h_1 + \frac{1}{2}u_1^2 = h_2 + \frac{1}{2}u_2^2. \tag{2.61}$$

Combining Eqs. (2.59), (2.60), and (2.61) with the equation for a perfect gas, (2.62),

$$h = C_pT = \frac{\gamma R}{\gamma - 1}\frac{P}{\rho R} = \frac{\gamma p}{(\gamma - 1)\rho}, \tag{2.62}$$

gives a new energy equation where γ is the ratio between the specific heat at constant pressure (C_P) to the heat capacity at constant volume (C_V),

$$\frac{\gamma}{\gamma - 1}\frac{p_1}{\rho_1} + \frac{1}{2}u_1^2 = \frac{\gamma}{\gamma - 1}\frac{p_2}{\rho_2} + \frac{1}{2}u_2^2. \tag{2.63}$$

A set of ratios between the parameters in front of and behind the shock can be generated using Eqs. (2.59), (2.60), (2.61), and (2.63). These ratios are known as the Rankine-Hugoniot relations [49]:

$$\frac{p_2}{p_1} = 1 + \frac{2\gamma}{\gamma+1}(M_1^2 - 1), \tag{2.64}$$

$$\frac{\rho_2}{\rho_1} = \frac{u_1}{u_2} = \frac{(\gamma+1)M_1^2}{(\gamma-1)M_1^2+2}, \tag{2.65}$$

$$M_2^2 = \frac{(\gamma-1)M_1^2+2}{2\gamma M_1^2+1-\gamma}, \tag{2.66}$$

$$\frac{T_2}{T_1} = 1 + \frac{2(\gamma-1)}{(\gamma+1)^2}\frac{\gamma M_1^2+1}{M_1^2}(M_1^2-1). \tag{2.67}$$

The entropy is given as:

$$\frac{S_2 - S_1}{C_V} \approx \frac{2\gamma(\gamma-1)}{3(\gamma+1)^2}(M_1^2-1). \tag{2.68}$$

The entropy then reduces to:

$$\frac{S_2 - S_1}{C_V} \approx \frac{\gamma^2-1}{12\gamma^2}\left(\frac{\Delta P}{\rho_1}\right)^3. \tag{2.69}$$

The shockwave thickness, δ, is given by,

$$\frac{\delta \Delta u}{v} \sim 1, \tag{2.70}$$

where $(\delta\Delta u)/v$ is the Reynold's number.

Analytical expressions have been derived to describe the expansion of a shock wave produced by a strong explosion [41]. The laser ablation used in the experiments in this dissertation generates strong explosions. Several assumptions are needed in order to derive this analytical expression. A large, instantaneous amount of energy, E, is released into a small volume during a small time interval. This energy is released into a perfect, ideal gas with constant density, ρ_0, and specific heats to create a strong explosion. The phrase "strong explosion" is used here as it is used by Zel'dovich and

Razier in *Physics of Shock Waves and High-Temperature Hydrodynamic Phenomena* [41]. The initial pressure, p_0, of the ambient gas is neglected because it is assumed to be much less than the pressure behind the shock. A more stringent requirement is [41]:

$$p_1 \gg [(\gamma + 1)/(\gamma - 1)]p_0. \tag{2.71}$$

It must be assumed that the shock wave is early in its propagation and that it has not propagated far from its source in order for this condition to be satisfied. The shock wave must also have traveled a distance, R, that is large compared to where it started, and the mass of gas set in motion by the explosion must be larger than the mass of the explosion products. Neglecting the initial pressure of the ambient gas means, by extension, that the internal energy of the gas may be neglected because the energy of the explosion is much greater. The initial speed of sound in the gas is much less than the velocity of the shock and wave front and may be neglected.

The dimensionless similarity variable, ζ, is defined as [41]:

$$\zeta = r\frac{\rho_0}{Et^2}^{1/5}. \tag{2.72}$$

The motion of a spherical wave-front can then be defined as [41]:

$$R(t) = \zeta_0 \left(\frac{E}{\rho_0}\right) t^{2/5}, \tag{2.73}$$

$$D(t) = \frac{dR}{dt} = \zeta_0 \frac{2}{5} \left(\frac{E}{\rho_0}\right)^{1/5} t^{-3/5}. \tag{2.74}$$

The pressure behind the shock, p_1, decreases in time according to [41]:

$$p_1 \sim \rho_0 D^2 \sim \rho_0 \left(\frac{E}{\rho_0}\right)^{2/5} t^{-6/5} \sim \frac{E}{R^3}. \tag{2.75}$$

The velocity distribution of molecules ejected from the condensed phase of material is different from the velocity distribution of molecules in the vapor phase [50]. This difference in the velocity distributions produces a thin region at the interface with a strong non-equilibrium state. This thin region is named the Knudsen layer. The Knudsen layer serves as a discontinuous boundary condition between the condensed phase and the vapor phase. Vapors escaping from the molten surface are non-isotropic because their velocity vectors are directed away from the molten material. Atoms and molecules in the vapor experience collisions, and their velocities move towards an isotropic distribution. The Knudsen layer is the region where these collisions convert the vapor's non-isotropic velocity distribution to an isotropic velocity distribution [36]. Separate Maxwellian functions describe the molten material at the surface and the material in the vapor. The Knudsen layer is usually the width of a few mean free paths of the vapor atoms/molecules. This width is generally a few micrometers.

Ratios between the Knudsen layer and the target surface for the temperature, the density, and the pressure are given by Eqs. (2.76), (2.77), and (2.78) [11]:

$$\frac{T_{KL}}{T_s} = \left[\sqrt{1+\pi\left(\frac{\gamma-1}{\gamma+1}\frac{\alpha}{2}\right)^2} - \sqrt{\pi}\frac{\gamma-1}{\gamma+1}\frac{\alpha}{2}\right]^2, \tag{2.76}$$

$$\frac{\rho_{KL}}{\rho_S} = \sqrt{\frac{T_S}{T_{KL}}}\left[\left(\alpha^2+\frac{1}{2}\right)e^{\alpha^2}erfc(\alpha) - \frac{\alpha}{\sqrt{\pi}}\right] + \frac{1}{2}\frac{T_S}{T_{KL}}[1-\sqrt{\pi}\alpha e^{\alpha^2}erfc(\alpha)], \tag{2.77}$$

$$\frac{p_{KL}}{p_s} = \frac{\rho_{KL}T_{KL}}{\rho_S T_S}. \tag{2.78}$$

T is temperature, P is pressure, ρ is density, and $\gamma = C_P/C_V = (j+5)/(j+3)$ where j is the number of accessible internal degrees of freedom. M is the Mach number,

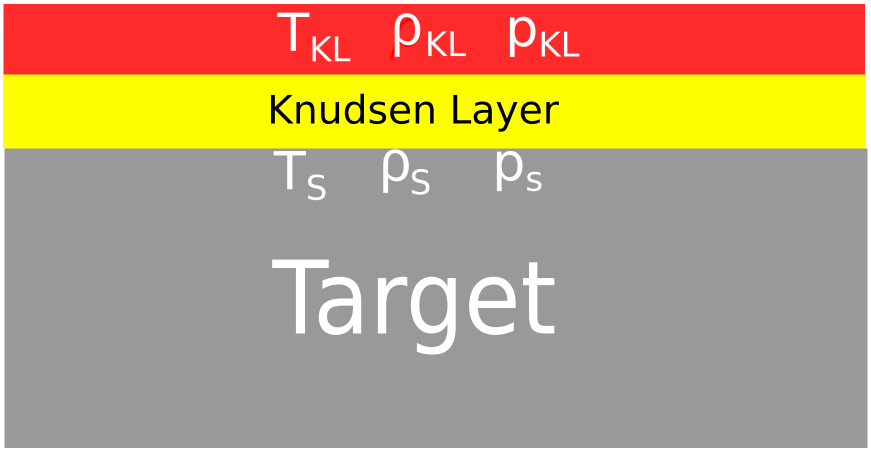

Figure 2.2 This sketch shows T_s, ρ_s, and p_s at the surface. The new parameters, T_{KL}, ρ_{KL}, and p_{KL}, represent the new equilibrium established after the collisional processes in the Knudsen layer.

$M = u_K L/(\gamma R T_{KL})^{1/2}$, and $\alpha = (\gamma/2)^{1/2} M$. The erfc is the complimentary error function $(erfc(\alpha) = (2/\sqrt{\pi}) \int_{\alpha}^{\infty} e^{-s} ds)$.

Four collision processes can be outlined for laser ablated plasmas. The following equations hold if the plasma in question is described by Maxwell-Boltzmann statistics [42].

1) Elastic collisions between electrons:

$$e^-(E_{e^-\alpha}) + e^-(E_{e^-\beta}) \iff e^-(E_{(e^-\alpha} - \Delta E_{\alpha\beta}) + e^-(E_{e^-\beta} + \Delta E_{\alpha\beta}), \tag{2.79}$$

2) Inelastic collisions between electrons leading to excitation and de-excitation:

$$A_l + e^-(E_{e^-}) \iff [K^{deexc}]K^{exc} A_u + e^-(E_{e^-} - \Delta E_{ul}), \tag{2.80}$$

3) Ionization/Recombination:

$$A_l + e^-_{(E_{e^-})} \iff A^+ + e^-_{(E_{e^-} - E'_{e^-} - E_{ion} + E_l)} + e^-_{(E'_{e^-})}, \tag{2.81}$$

$$A_l + h\nu_{(E_{e^-} - E_l)} \iff A^+ + e^-_{(E_{e^-} - E_{ion} + E_l)}, \tag{2.82}$$

4) Spontaneous emission and absorption:

$$A_u \iff A_l + h\nu_{ul}. \tag{2.83}$$

2.5 Optical Spectroscopy

The subject of spectroscopy is indispensable for research involving laser ablation and plasmas. A full development and derivation of the equations used in atomic and molecular spectroscopy can be found in books including those by Griem, Cowan, and Herzburg [51–53]. The treatment of spectroscopy presented below develops the major relevant results focused on this project.

2.5.1 Atomic Spectroscopy

Atomic spectroscopy measures the change in energy of the electron(s) in an atom. The energy states of an electron are a result of the Coulomb interaction between that electron and all other electrons in the atom, and the nucleus. The most direct derivation of energy levels is seen for the hydrogen atom. Hydrogen has one electron and one proton. This configuration makes the Coulomb interaction straightforward. The Schrödinger equation,

$$H\psi = \left(-\frac{\hbar^2}{2m}\nabla^2 + V\right)\psi = E\psi, \tag{2.84}$$

for the hydrogen atom in spherical coordinates is [54]:

$$r^2\left(\frac{\partial^2}{\partial r^2} + \frac{2}{r}\frac{\partial}{\partial r}\right)\psi + \frac{2mr^2}{\hbar^2}(E - V)\psi = L^2\psi. \tag{2.85}$$

L^2 describes the angular components:

$$L^2 = -\left[\frac{1}{sin\theta}\frac{\partial}{\partial\theta}\left(sin\theta\frac{\partial}{\partial\theta}\right) + \frac{1}{sin^2\theta}\frac{\partial}{\partial\phi}\right]. \tag{2.86}$$

Eq. (2.86) is solved with Legendre polynomials that give spherical harmonics which are eigenfunctions of the operators $\hat{L}^2$ and $\hat{L}_z$. These eigenfunctions are characterized by the numbers l and m:

$$\hat{L}^2 = l(l+1)\hbar^2, \tag{2.87}$$

$$\hat{L}_z = m\hbar. \tag{2.88}$$

Another form of momentum that is important for the electron is the spin. Spin is an intrinsic property of the electron and takes on the values $\pm\frac{1}{2}$ because the electron is a fermion. The operator $\hat{s}^2$ is:

$$\hat{s}^2 = s(s+1)\hbar^2. \tag{2.89}$$

The total angular momentum of any single electron is given by:

$$j = l + s, \tag{2.90}$$

and can take on the values $j = |l+s|, |l+s-1|, \ldots, |l-s|$.

The coupling of the total angular momentum contributions from different electrons is accomplished by using the LS-coupling scheme for light atoms. The LS-coupling scheme is also known as the Russell-Saunders coupling scheme. The total angular momentum for an electron is given by:

$$S = s_1 + s_2 + \cdots = \sum_i s_i, \tag{2.91}$$

$$L = l_1 + l_2 + \cdots = \sum_i l_i, \tag{2.92}$$

$$\vec{J} = \vec{L} + \vec{S}, \tag{2.93}$$

$$|\vec{J}|^2 = |\vec{L} + \vec{S}| \cdot |\vec{L} + \vec{S}| = \vec{L}^2 + \vec{S}^2 + 2\vec{L} \cdot \vec{S}, \tag{2.94}$$

$$J_z = M_J \hbar \quad with \quad M_J = \pm|J|, \pm|J-1|, \ldots. \tag{2.95}$$

An atomic state can be characterized by the term symbol $^{2S+1}L_J$. Selection rules in the LS-coupling scheme are given in Table 2.1. Heavier atoms use the jj-coupling scheme:

$\Delta l = \pm 1$; $\Delta m = 0, \pm - 1$
Parity Must Change
$\Delta J = 0, \pm - 1$ ($0 \leftrightarrow 0$ Not Allowed); $\Delta M_j = 0, \pm - 1$ ($\Delta M_j = 0$ Not Allowed if $\Delta J = 0$)

Table 2.1 These selection rules apply to dipole allowed transitions.

L:	0	1	2	3	4	5
	S	P	D	F	G	H

Table 2.2 The term symbols that are used for L.

$$\vec{j}_1 = \vec{l}_1 + \vec{s}_1, \tag{2.96}$$

$$\vec{j}_2 = \vec{l}_2 + \vec{s}_2, \tag{2.97}$$

$$\vec{J} = \vec{j}_1 + \vec{j}_2 + \cdots = \sum_i \vec{j}_i. \tag{2.98}$$

The degeneracy of an energy level described by ^{2S+1}L is $g_{LS} = (2S+1)(2L+1)$ in the LS-coupling scheme. The multiplicity of states is given by $2s+1$, and specifies the singlet, doublet, and triplet states as 1, 2, and 3, respectively.

The energy levels of the hydrogen atom are described by [38]:

$$E_n = -\left(\frac{1}{4\pi\epsilon_0}\right)^2 \frac{me^4}{2n^2\hbar^2}. \tag{2.99}$$

A general expression for hydrogen-like ions with Z protons is:

$$E_n = -\left(\frac{Z^2}{4\pi\epsilon_0}\right)^2 \frac{me^4}{2n^2\hbar^2}. \tag{2.100}$$

Atoms with a large number of electrons require a different approach. The repulsive interactions between the electrons must be accounted for. It is common to use the Hartree-Fock method to analyze the energy levels of high Z molecules. The Hartree-Fock method describes each electron as a spherical average over the distribution of all other electrons in the atom [55].

A temperature can be determined by measuring the relative light intensity for different wavelengths. The calculated temperature applies to the particular degree of freedom for the particular species under study. This method is called the Boltzmann plot method and is derived from a Maxwell-Boltzmann statistical distribution [56]. Two energy levels, E_i and E_j, are chosen for a specific atomic (or molecular) species. The number of counts measured is represented by N_i and N_j at each energy level. The Boltzmann distribution is given by Eq. (2.101) if thermal equilibrium has been reached [56]:

$$\frac{N_j}{N_i} = \frac{g_j}{g_i} \exp\left[-\frac{E_j - E_i}{kT}\right]. \tag{2.101}$$

The statistical weights for the lower and upper states in Eq. (2.101) are g_i and g_j, respectively. T is the temperature in K, and k is the Boltzmann constant given by 8.617×10^{-5} eV/K. The Boltzmann relation is applicable to the population distribution over an atomic state if the total population density is N:

$$\frac{N_j}{N} = \frac{g_j}{Z(T)} \exp\left[-\frac{E_j - E_i}{kT}\right]. \tag{2.102}$$

$Z(T)$ is called the partition function:

$$Z(T) = \sum g_m \exp\left(-\frac{E_m}{kT}\right). \tag{2.103}$$

$Z(T)$ is the sum of the weighted Boltzmann functions of all the discrete energy levels. The emission coefficient for a given atomic transition from E_j to E_i is given by Eq. (2.104):

$$\epsilon_{ji} = \frac{hc_0}{4\pi\lambda_{ji}} A_{ji} N_j. \tag{2.104}$$

A_{ji} is the transmission probability, λ_{ji} is the wavelength of the transition, h is Planck's constant (6.626 x 10^{-34} $J \cdot s$), and c_0 is the speed of light (3 x 10^8 m/s). A_{ji}, named the spontaneous emission coefficient, is the probability per second that the atom in energy state E_j will spontaneously emit a photon in a random direction and transition to energy state E_i. Eq. (2.105) is produced when Eq. (2.104) is inserted into Eq. (2.102) and rearranged:

$$\frac{\epsilon_{ji}\lambda_{ji}}{A_{ji}g_j} = \frac{hc_0 N}{4\pi Z(T)} exp\left[-\frac{E_j}{kt}\right]. \tag{2.105}$$

The final equation used to calculate the temperature is generated after taking the natural logarithm of both sides of Eq. (2.105) [56]:

$$\ln\frac{\epsilon_{ji}\lambda_{ji}}{A_{ji}j_j} = -\frac{E_j}{kt} + C. \tag{2.106}$$

C is a constant. A graph that plots the left side of Eq. (2.106), as a function of E_j, shows a straight line. The slope of that line gives the temperature.

2.5.2 Molecular Spectroscopy

The molecules discussed in this dissertation will all be diatomic. Diatomic molecules are sometimes found in low temperature plasma. The density of available energy states increases when molecules are added to plasmas and produces a more complex spectrum. This discussion of molecular spectroscopy will be based on the works of Herzburg, Steinfeld, Weissbluth, and Kakkar [53, 54, 57, 58].

The Born-Oppenheimer approximation shows that the electronic, vibrational, and rotational energies of diatomic molecules can be treated independently because they differ by several orders of magnitude:

$$\Delta E_{electronic} \approx 10^3 \Delta E_{vibrational} \approx 10^6 \Delta E_{rotational}. \tag{2.107}$$

The total wavefunction is the product of the individual wavefunctions for the electronic, vibrational, and rotational components,

$$\psi_T \approx \psi_{el} \psi_{vib} \psi_{rot}, \tag{2.108}$$

and the total energy of a state can be calculated as:

$$E_{Total} \approx E_{electronic} + E_{vibrational} + E_{rotational}. \tag{2.109}$$

Eq. (2.109) provides the expression for the approximate total internal energy of a simple diatomic molecule.

The rotational motion of a diatomic molecule has a classical analogue in the rigid rotor shown in Fig. 2.3. Two masses are attached with a rigid rod which is allowed

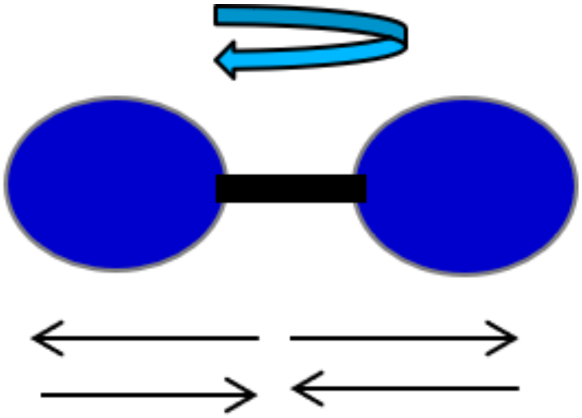

Figure 2.3 This model of a diatomic molecule shows the vibrational and rotational degrees of freedom.

to rotate around the center of mass. The reduced mass, μ, of this system is:

$$\mu = \frac{m_1 m_2}{m_1 + m_2}. \tag{2.110}$$

The moment of inertia is:

$$I = \frac{m_1 m_2}{m_1 + m_2} r_e^2 = \mu r_e^2. \tag{2.111}$$

The equilibrium distance between the two nuclei is r_e. Eq. (2.112) describes the kinetic energy of the relative motion of the atoms in the diatomic molecule if the motion of the electron is neglected. Center of mass motion is not relevant for the internal motion of the molecule, and the second term on the right side of Eq. (2.112) is dropped [54],

$$T = \left(\frac{\mathbf{p}^2}{2\mu}\right) + \left(\frac{\mathbf{P}^2}{2M}\right), \tag{2.112}$$

where

$$\mathbf{p} = \left[\frac{1}{m_1 + m_2}\right]\left[m_1\mathbf{p_2} - m_2\mathbf{p_1}\right], \tag{2.113}$$

$$\mathbf{P} = \mathbf{p_1} + \mathbf{p_2}, \tag{2.114}$$

$$M = m_1 + m_2. \tag{2.115}$$

The potential energy, $V(r)$, for the vibration and rotation depends on the distance between the two nuclei, $r = r_2 - r_1$. The equilibrium distance, r_e, is defined as the the location where $V(r)$ is at a minimum. The Taylor expansion around r_e is:

$$V(r) = V(r_e) + \left(\frac{dV}{dr}\right)_{r=r_e}(r - r_e) + \frac{1}{2}\left(\frac{d^2V}{dr^2}\right)_{r=r_e}(r - r_e)^2 + \cdots . \tag{2.116}$$

The expansion in Eq. (2.116) is reduced to:

$$V(r) = V(r_e) + \frac{1}{2}\left(\frac{d^2V}{dr^2}\right)_{r=r_e}(r - r_e)^2, \tag{2.117}$$

and rewritten as:

$$V(r) = -D_e + \frac{1}{2}k(r - r_e)^2, \tag{2.118}$$

because dV/dr is zero, $V(r_e) \equiv -D_e$, and $(d^2V/dr^2)_{r=r_e} \equiv k$.

$V(r)$ is inserted into the Hamiltonian,

$$H = \left(\frac{p^2}{2\mu}\right) + V(r), \tag{2.119}$$

and the Hamiltonian is inserted into Schrödinger's Equation:

$$\left[-\frac{\hbar^2}{2\mu}\nabla^2 + V(r)\right]\psi = E\psi. \tag{2.120}$$

Eq. (2.120), represented in spherical coordinates, becomes Eq. (2.121):

$$r^2\left(\frac{\partial^2}{\partial r^2}+\frac{2}{r}\frac{\partial}{\partial r}\right)\psi+\frac{2\mu r^2}{\hbar^2}[E-V(r)]\psi=L^2\psi, \tag{2.121}$$

with

$$L^2\psi=J(J+1)\psi. \tag{2.122}$$

ψ takes the following form in spherical coordinates [54]:

$$\psi=\frac{1}{r}P(r)Y_{J,M}(\theta,\phi). \tag{2.123}$$

The radial component of Eq. (2.121) is:

$$\frac{d^2P}{dr^2}+\frac{2\mu}{\hbar^2}[E-V(r)]P(r)-\frac{J(J+1)}{r^2}P(r)=0, \tag{2.124}$$

with $J=0,1,2,...$ and $M=J,J-1,...,-J$. J is set to $J=0$ to represent no rotational motion and yields the Schrödinger equation for the simple harmonic oscillator:

$$\frac{d^2P(r)}{dr^2}+\frac{2\mu}{\hbar^2}[E-V(r)]P(r)=0. \tag{2.125}$$

The energies of the simple harmonic oscillator are given by:

$$E_\nu=\hbar\omega_0\left(\nu+\frac{1}{2}\right)-D_e, \tag{2.126}$$

with $\omega_0=\sqrt{k/\mu}$ and $\nu=0,1,2,\ldots$.

The simple harmonic oscillator is generally a poor model for representing the potential of chemical bonds. An empirically derived potential, named the Morse potential, is more appropriate and is shown in Eq. (2.127):

$$V = D_e[1 - e^{-\beta(r-r_e)}]^2. \tag{2.127}$$

D_e is the dissociation energy and β is a constant which is derived when the Morse potential is inserted into the Schrödinger equation. The energy levels are given by Eq. (2.128) [54]:

$$G(\nu) = \omega_e(\nu + (1/2)) - \omega_e\chi_e(\nu + (1/2))^2, \tag{2.128}$$

with

$$\omega_e = \beta\sqrt{\frac{D_e\hbar}{\pi c\mu}}, \tag{2.129}$$

$$\chi_e = \frac{\hbar\beta^2}{4\pi c\mu}. \tag{2.130}$$

χ_e is the anharmonicity constant.

$V(r)$ is set to zero when the oscillating motion between the atoms is removed, and the Schrödinger equation becomes:

$$\left(\frac{2I}{\hbar^2}\right) E\psi = L^2\psi = J(J+1)\psi, \tag{2.131}$$

and

$$E_J = \left(\frac{\hbar^2}{2I}\right) J(J+1) \qquad (J = 0, 1, 2, \dots). \tag{2.132}$$

I is defined in Eq. (2.111). The energy for the rotational degree of freedom is written as [54]:

$$F(J) = B_\nu J(J+1). \tag{2.133}$$

B_ν is the rotational constant and is given in units of cm^{-1}:

$$B_\nu = \frac{\hbar}{4\pi Ic}. \tag{2.134}$$

The rotational constant depends on the vibrational state, ν. Higher order terms, the coupling between vibrational and rotational motions, and the addition of electronic rotations about the other two axes should be considered when higher precision is needed. The total energy for a particular state of the molecule's vibrational and rotational motion is generated when Eq. (2.128) and Eq. (2.133) are combined:

$$G(\nu) + F(J) = \omega_e \chi_e (\nu + \frac{1}{2})^2 + B_\nu J(J+1). \tag{2.135}$$

The equation for the total energy of a diatomic molecule, in a particular state, is:

$$T = \frac{E_{el}}{hc} + \omega_e \chi_e (\nu + \frac{1}{2})^2 + B_\nu J(J+1). \tag{2.136}$$

A molecular state can be characterized by the term symbol $^{2\Sigma+1}\Lambda_\Omega$. The molecular state term symbol is analogous to the atomic state term symbol. Λ is equal to the sum of the individual orbital angular momentum numbers, λ_i, for each electron: $\Lambda = \sum \lambda_i$. The selection rules for diatomic molecules are given in Tables 2.4 and 2.5.

Λ:	0	1	2
	Σ	Π	Δ

Table 2.3 The term symbols that are used for Λ.

$\Delta l = \pm 1$; $\Delta m = 0, \pm - 1$
parity must change
$\Delta J = 0, \pm - 1$ ($0 \leftrightarrow 0$ Not Allowed); $\Delta M_j = 0, \pm - 1$ ($\Delta M_j = 0$ Not Allowed if $\Delta J = 0$)

Table 2.4 These selection rules apply to dipole allowed transitions in molecules.

$\Delta\Lambda = 0, \pm 1$
$\Delta S = 0$
$\Delta 0, \pm 1$
$+ \leftrightarrow +, \quad - \leftrightarrow -$
Homonuclear Molecules: $g \leftrightarrow u$

Table 2.5 Additional dipole allowed transition selection rules for molecules.

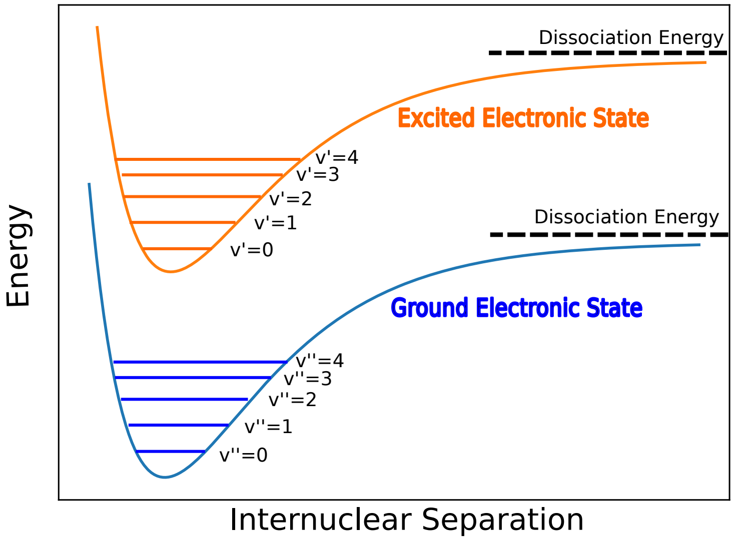

Figure 2.4 The vibrational energy levels for two electronic states for a generic diatomic molecule are shown. The Morse potential is used for the vibrational energy levels.

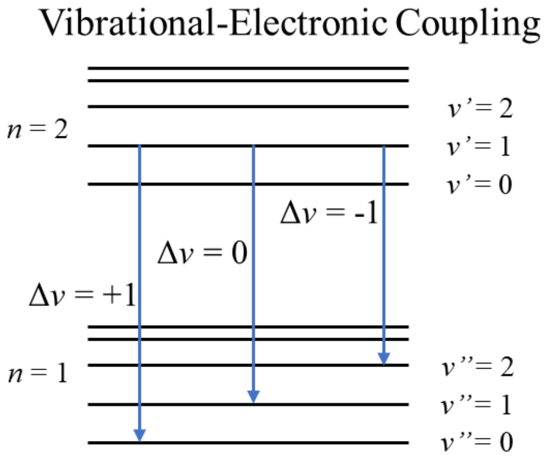

Figure 2.5 This diagram shows $\Delta v = +1, 0, -1$ for a transition between electronic energy states.

2.5.3 Line Broadening

The discussion of atomic and molecular spectroscopy has focused on determining energy states and the transitions between energy states that generate the emission or absorption of electromagnetic radiation. Purely mono-energetic states are not observed in spectroscopy. The line width that is observed in spectroscopy is produced by a combination of physical effects and limitations in the experimental apparatus.

Natural broadening results from quantum mechanics. The lifetime of the upper state of an atom or molecule is limited by its spontaneous transition to a lower state. The lifetime, Δt, directly affects the energy spread of the transition between the two states due to the uncertainty relation [59]:

$$\Delta E \approx \frac{h}{2\pi t}, \tag{2.137}$$

with

$$\frac{1}{t} \approx \Sigma_j A_{ij}. \tag{2.138}$$

A_{ij} is the Einstein spontaneous emission coefficient. Eq. (2.138) is the sum of all spontaneous transitions from state i. The broadening of spectral lines for transitions from state i due to the broadening of state i is:

$$\Delta\nu = \Delta E/h \approx 1/2\pi t. \tag{2.139}$$

The profile of the broadened line is given as:

$$I(v) = I(\nu_0)\frac{1}{1 + [(\nu - \nu_0)2\pi t]^2}, \tag{2.140}$$

with the intensity, I, and the line center, v_0. Eq. (2.140) has a Lorentzian line profile, and the Full-Width-Half-Maximum (FWHM) is:

$$\Delta\nu_{1/2} = \frac{1}{\pi t}. \tag{2.141}$$

Doppler broadening occurs due to the thermal motion of the emitting atoms or molecules. This motion produces a Doppler shift [59]:

$$\Delta\nu = \nu - \nu_0 = \nu_0 v/c, \tag{2.142}$$

where v is the line of sight particle velocity. This leads to a Maxwell velocity distribution for each species of particles:

$$I(\nu) = I(\nu_0)exp[-(\nu - \nu_0)^2 c^2/2\nu_{ta}^2\nu_0^2], \tag{2.143}$$

where $\nu_{ta}^2 = T_a/m_a$ for the emitting atom or molecule. The FWHM is given by:

$$\Delta\nu_{1/2} = 2\nu_0(\nu_{ta}/c)(2ln2)^{1/2}. \tag{2.144}$$

Eq. (2.144) can also be written as:

$$\Delta\nu_{1/2} = \sqrt{\frac{8kT\ln 2}{mc^2}}\,\nu_0. \tag{2.145}$$

Pressure broadening results from the collision between atoms and molecules in the gas or plasma. The collisions perturb the undisturbed state lifetimes. The greater variation in state lifetime (Δt) directly leads to a greater energy spread (ΔE) due to the uncertainty relation $\Delta E \Delta t \geq \hbar$. The broadening of the spectral line is directly proportional to the pressure. Eq (2.146) gives the FWHM width of the light's frequency ($\Delta\nu_{1/2}$) due to pressure broadening [60]:

$$\Delta\nu_{1/2} = P\sum_{A} X_A \sigma_{AB}^2 \sqrt{\frac{8}{\pi \mu_{AB} kT}} \cdot 1.0113 \times 10^6. \tag{2.146}$$

P is the pressure in atm, μ_{AB} is the reduced mass of the perturbed and the perturbing atom/molecule, and σ_{AB} is the collision cross section. The factor 1.0113×10^6 converts pressure from atm to Pa. and the summation occurs over the molar ratios (X_A) of the different perturbing gases. The line shape is given by Eq. (2.147) [60]:

$$I(\nu) = \frac{1}{\pi}\frac{\Delta\nu_c/2}{(\nu-\nu_0)^2 + (\Delta\nu_c/2)^2} \tag{2.147}$$

Instrumental broadening contributes a Gaussian line profile to the width of spectral lines. Instrumental broadening results directly from the resolution of the spectroscopic system used to measure the spectral lines. An equation which produces the Gaussian line profile is:

$$I(\nu) = Aexp[(-\frac{(\nu-\nu_0)^2}{2C^2}]. \tag{2.148}$$

A is the amplitude. C is a parameter related to the FWHM by:

$$C = \frac{\nu_{1/2}}{2\sqrt{2\log 2}}. \tag{2.149}$$

The instrumental broadening FWHM is measured experimentally by shining a narrow wavelength laser, such as a HeNe or Ar-ion, into the spectrometer at low power. Gas lasers like the HeNe and Ar-ion have line widths much narrower than what is produced as a result of instrumental line broadening. Any observed broadening is generated by the spectroscopic system.

2.5.4 Radiation Transport

Any material which emits radiation is capable of absorbing radiation. Plasma which emits radiation at a particular frequency, ν, will also absorb radiation at that frequency. Some spectroscopic measurements are taken with the assumption that the plasma is optically thin. This assumption means that the re-absorption of emitted radiation is negligible. The theory of radiation transport must be integrated into any spectroscopic intensity measurement when the plasma is not optically thin. Eq. (2.150) gives the equation for radiation transport for a slab geometry [59, 61–63]:

$$\mu\frac{dI_{\nu\mu}}{dz} = -\kappa_\nu(z)I_{\nu\mu}(z) + j_\nu(z), \quad \mu = cos\theta. \tag{2.150}$$

The distance along the path of the light is z, $I_{\nu\mu}$ is the intensity at frequency ν, $j(\nu)$ is the coefficient for spectral line emission at frequency ν, and κ_ν is the coefficient for spectral line absorption, known as the opacity, at frequency ν.

Eqs. (2.151) and (2.152) demonstrate the case of a transition between the upper level i and lower level k with particle density n_i [61, 62]:

$$j_\nu = \sum_{i=1}^{n_i} \sum_{k<i} n_i A_{ik} \{\phi_{ik}\}_\nu \frac{h\nu_{ik}^0}{4\pi}, \tag{2.151}$$

$$\kappa_\nu = \sum_{i=1}^{n_i} \sum_{k>i} (n_i B_{ik} - n_k B_{ki}) \{\phi_{ik}\}_\nu \frac{h\nu_{ik}^0}{4\pi}. \tag{2.152}$$

A_{ik} is the Einstein coefficient for radiative decay, B_{ik} is the Einstein coefficient for stimulated emission, and B_{ki} is the Einstein coefficient for absorption. Eq. (2.150) is a first-order ordinary differential equation whose solution is [61, 62]:

$$I_{\nu\mu}(L) = \int_0^L exp\left(-\int_t^L \kappa_\nu(t')dt'\right) j_\nu(t)dt. \tag{2.153}$$

The integrand $\int_t^L \kappa_\nu(t')dt'$ is set equal to $\tau(t)$, which is the optical depth, and gives [61]:

$$I_{\nu\mu}(L) = \int_0^L exp\left(-\tau(t)\right) j_\nu(t)dt. \tag{2.154}$$

Eq. (2.154) gives the total intensity of light observed at a spectrometer outside of the plasma at a point L. This equation accounts for light with spectral frequencies between ν and $\nu + d\nu$ that was produced in the plasma in the region $t + dt$. Eq. (2.154) also accounts for the attenuation from t to L of the radiation produced in the region $t + dt$.

Chapter 3

Experimental Apparatus

3.1 Introduction

A significant component of the work involved in this dissertation was the development of the LAPeX experimental apparatus. The Laser Ablation Plume eXperiment (LAPeX) apparatus was originally conceived to be a platform to explore the parameter space surrounding laser ablation. LAPeX was designed and built to explore the laser ablation process with both spatial and temporal resolution. LAPeX was located at the SAGE building Cheetah Laser Lab which was a part of the Physics Department at the University of Nevada, Reno.

The LAPeX apparatus was capable of studying laser ablation plumes generated from solid targets created by a pulsed ND:YAG laser in vacuum or background gas pressure up to atmosphere. Optical spectrometers were used to collect both low- and high- resolution spectra of the ablation plume. Optical diagnostics included shadowgraphy and interferometry. Short temporal gate images of the plume were collected with intensified CCD cameras, and additional diagnostics included mass spectroscopy and total plume charge measurement.

The LAPeX apparatus was designed not only to measure many simultaneous

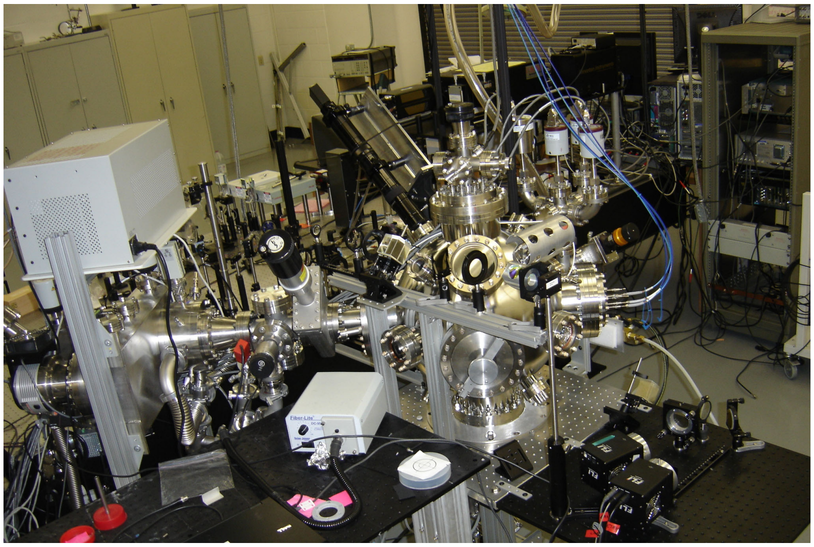

Figure 3.1 Image of the LAPeX apparatus.

parameters in parameter space, but also to be able to explore a wide variety of experimental conditions. Variations in gas species and pressure, laser intensity on target, and external electric and magnetic fields could be introduced into the experiment. These built in capabilities provided a wide diversity of possible experiments that included the investigation of plasmas, the interaction of lasers with solids, and LIBS/LAMIS.

3.2 General Experimental Procedure

Each set of experiments carried out with the LAPeX apparatus involved the same general procedures. Solid targets in the form of thin sheets were cut to fit onto the target holder plug. The target holder plug was then carefully inserted into the target holder so that the surface of the target was aligned with the front face of the target holder. Any wires or fiber optics that needed to be connected to the target holder were connected at this time.

Wavelength calibration and imaging alignment were verified before inserting the target. Wavelength calibration was carried out with spectral calibration lamps, a HeNe laser, and an Ar-ion laser. The lasers were allowed to bounce off of the target holder and reflect back to the spectrometer. The ICCD gain would be turned down, or neutral density filters would be inserted in front of the spectrometers, if the intensity was too large to safely put into the spectrometer without damaging the ICCD detector. The spectral lamps were either inserted into the target holder and imaged with the optics used to gather and transport the light from the chamber, or placed immediately outside of the chamber in the same optical path and imaged with a different lens.

Wavelength calibrations were made by measuring the centroid pixel position for a given wavelength. Polynomial fits with $R^2 > 0.95$ were used for low resolution gratings. Polynomial and linear fits were used for high resolution gratings. Linear fits were sometimes required because of the difficulty in finding more than two calibration wavelengths in the spectral window. High resolution gratings generally have a linear fit over the spectral window being imaged by the ICCD. The focal position of all optics was also inspected at this stage. A grid with a 1-mm ruled scale was used to check the quality of optical images for each ICCD. A test shot with the optical diagnostics laser was fired, and a machine screw was illuminated from behind for a target scale to check the optical quality of the image.

The vacuum chamber was evacuated at this stage. The system was allowed to pump down to $1 \times 10^{-6} - 1 \times 10^{-7}$ Torr, if the experiment was going to be conducted in vacuum. The chamber was also evacuated to $1 \times 10^{-5} - 1 \times 10^{-6}$ Torr before experiments using rarefied gas backgrounds. The gas was then introduced into the chamber and pumped out to bring the chamber back to vacuum. This process was repeated two additional times to ensure that the chamber had been purged of any other gas that could contaminate the experiment. The final back-fill of the chamber introduced the gas to the desired pressure.

The alignment of the target was verified with the free-standing and spectrometer ICCD's, after the system was brought to the proper pressure. This verification was done by taking a single shot with the ablation laser. The mark left on the target was imaged by the ICCD's. The target was rotated so that the surface was perpendicular to the camera's line of sight. All data was collected using the manufacturer's software for each diagnostic.

Large amounts of material could coat the debris shield for the laser input port window when the final focusing lens was at its optimal focal distance and laser energy was at its maximum. The craters left in the target following this type of irradiation were deep enough that no additional shots could be taken in the same spot. One solution to this problem was to de-focus the final focusing lens by pushing the lens towards the target. This adjustment moved the focal spot past the target surface which had the effect of reducing the laser pulse intensity by increasing the spot size at the target surface. Another solution, described later in this chapter, involved the lowering of the pulse energy using a polarizer.

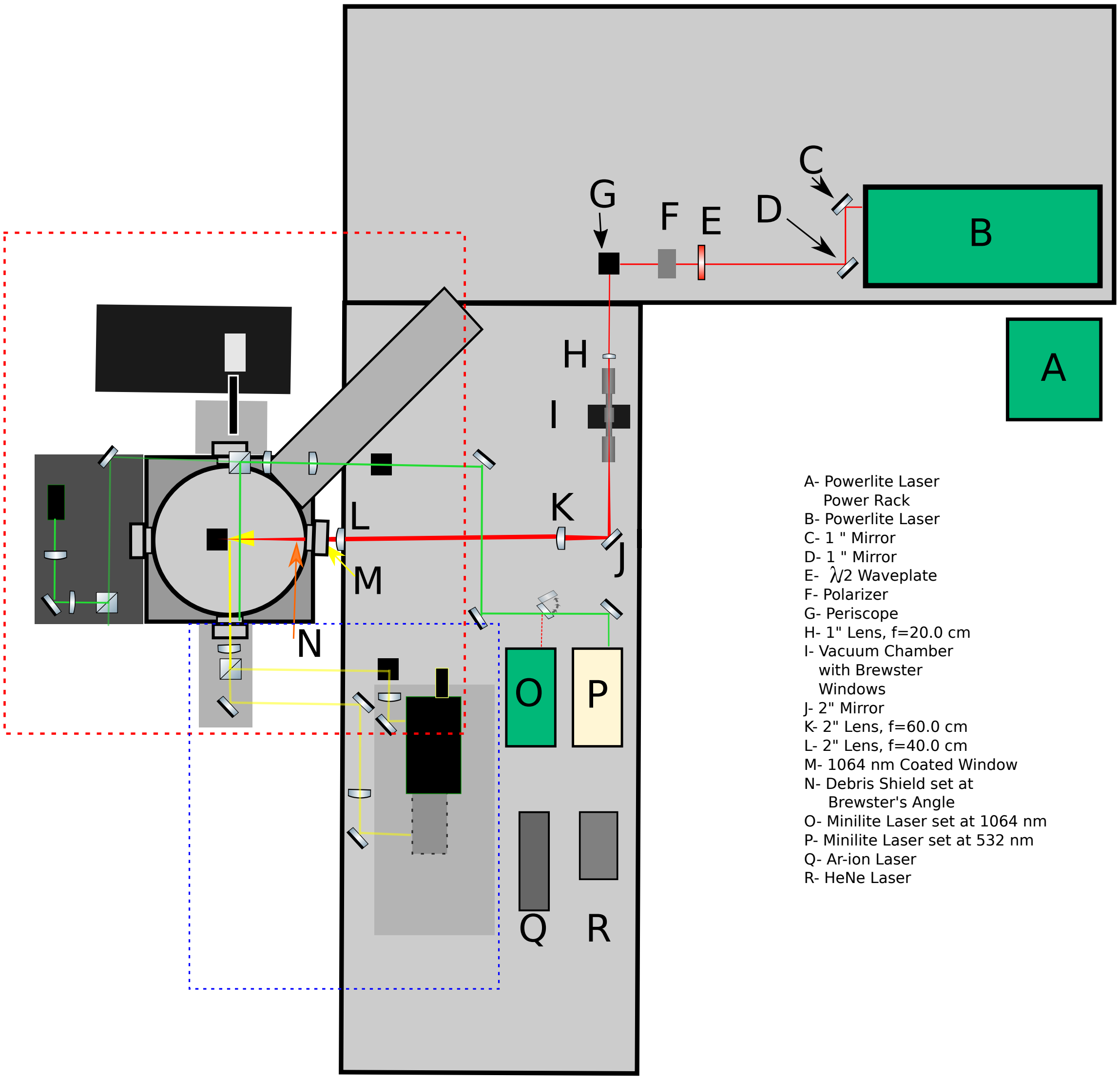

A- Powerlite Laser
Power Rack
B- Powerlite Laser
C- 1 " Mirror
D- 1 " Mirror
E- λ/2 Waveplate
F- Polarizer
G- Periscope
H- 1" Lens, f=20.0 cm
I- Vacuum Chamber
with Brewster
Windows
J- 2" Mirror
K- 2" Lens, f=60.0 cm
L- 2" Lens, f=40.0 cm
M- 1064 nm Coated Window
N- Debris Shield set at
Brewster's Angle
O- Minilite Laser set at 1064 nm
P- Minilite Laser set at 532 nm
Q- Ar-ion Laser
R- HeNe Laser

Figure 3.2 This diagram shows the LAPeX apparatus.

3.3 Ablation Laser

A "Continuum Powerlite II" laser served as the ablation laser for LAPeX. This laser was an ND:YAG laser operated at the fundamental wavelength at 1,064 nm. A doubling crystal for optional operation at 532 nm could also be installed. The laser pulse length was ∼ 9 ns.

Laser Wavelength	1064 nm	532 nm
Maximum Laser Energy	3.0 J	1.5 J
Polarization	Elliptical	Linear
Laser Pulse Length	∼9 ns	
Laser Spatial Profile	Gaussian	

Table 3.1 Various Powerlite laser parameters.

All laser beam energy measurements were taken with a Gentec Maestro meter and a Gentec QE50SP two-inch power head with a detachable Gentec QEA50 attenuator. The measurement was taken at the output of the laser and outside of the vacuum chamber after the final focusing lens. The spatial profile of the beam was taken using a Coherent Laser Cam IIID beam profiler. Temporal profiles were made using a Thorlabs DET 025A photodiode fed into a Tektronix TDS 3034B oscilloscope with 50 Ω input impedance. Table 3.1 shows the relevant laser parameters. See Figs. 3.3 and 3.4 for typical laser pulse profiles.

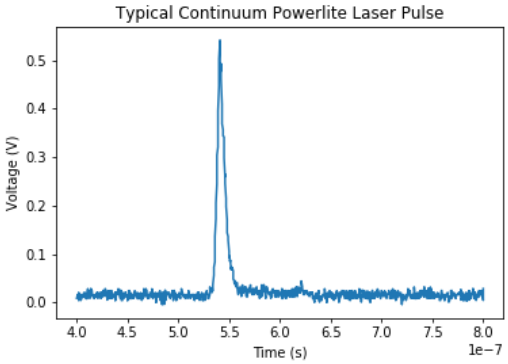

Figure 3.3 This is the temporal pulse profile of the Powerlite.

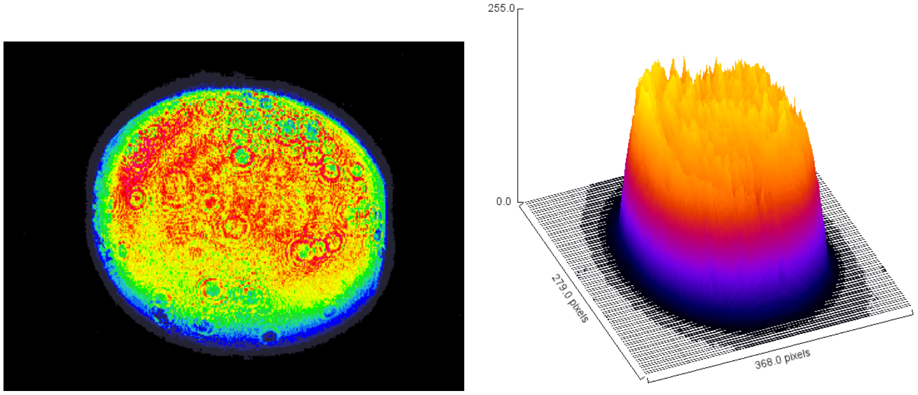

(a) **(b)**

Figure 3.4 (a) This picture shows the spatial profile of the Powerlite laser pulse averaged over 8 laser pulses. (b) Surface plot of the spatial profile.

3.3.1 Laser Energy Adjustment

An important capability of LAPeX is the ability to vary laser pulse energy. Several approaches can be taken to vary the laser pulse energy output from the Powerlite. One method adjusts the delay between the Q-switch trigger and the flashlamp trigger. The laser cavity can be dumped at a lower flashlamp light intensity at a different trigger delay time. Significant shot-to-shot jitter is introduced with this approach. Q-switch triggering occurs on a timing pulse slope when the delay is changed from the optimal flashlamp plateau.

A better approach takes the laser pulse output and reduces the energy using optical polarizers. The laser pulse energy was precisely varied, and a specific polarization was produced, by introducing a $\lambda\backslash2$ waveplate, an adjustable polarizer, and windows set at Brewster's angle. Laser light that did not match the polarization from the $\lambda\backslash2$ waveplate was passed to a laser beam dump from the polarizer. Any remaining polarizations, besides the one chosen to transmit through the Brewster's windows, were deflected downward. The laser light which reached the target had a very clean polarization with an extinction ratio, ϵ, of $\sim$100:1.

3.4 Experimental Chamber, Vacuum System, and Gas Handling

All of the LAPeX experiments were conducted in a vacuum chamber. Experiments were carried out in both vacuum and gaseous environments. The basic experimental chamber consisted of a sphere manufactured by the Kurt J. Lesker company. Optical windows, feedthroughs for fiber optics and electric signals, and valves were installed on the chamber to facilitate the experiments. A Varian V-250 turbomolecular pump was connected to the bottom of the chamber with a pneumatic gate valve separating the two components. A Pfeifer Duo 20 roughing pump was used as the backing pump for the turbo pump.

Vacuum pressure was monitored in the chamber using a Varian ion gauge. Four MKS capacitance manometers were used to measure gas pressure for experiments involving a gas background. These four gauges allowed pressures to be measured from atmosphere to ultra-high vacuum. Table 3.2 shows the range of each gauge. An over-pressure relief valve was installed on the chamber to prevent pressurizing the chamber above atmospheric pressure. LAPeX was designed to carry out experiments at or below atmospheric pressure. All chamber components were designed to operate in vacuum and cannot be safely pressurized above atmospheric pressure.

All windows on the experimental chamber were made from high quality fused silica and are optically flat. The ablation laser input port used a Thorlabs 1,064 nm anti-reflection coated wedge window. A debris shield mounted at Brewster's angle was placed after the wedge window. The wedge and the debris shield both prevented the back reflection of high energy laser light into the optical train.

Laser ablation experiments require the target to be moved at regular intervals between shots to prevent inconsistencies in the data due to ablation from irradiating craters instead of a flat surface. Factors including laser pulse energy and laser spot size determine the amount of damage the target sustains during each shot. High laser intensity shots (1×10^{14} W/cm^2) required the target to be moved to a fresh surface after each shot. Lower laser intensity shots ($\leq 10^{10}$ W/cm^2) required the target to be moved after 10 shots. A Newport 3-axis stage sat upside down in the chamber. A rod connected the target holder to the stage. Three vacuum compatible motors moved the 3-axis stage. The target was moved along the horizontal axis to produce a row of shots. The target was then moved along the vertical axis to start a new row.

Gauge	Range (Torr)
MKS 626A	1000
MKS 626A	100
MKS 626A	1
MKS 627	0.05
Varian Ion Gauge	10^{-10}

Table 3.2 This chart shows the pressure range measured by each of the gauges in the LAPeX vacuum and gas handling system.

3.5 ICCD Imaging

Fast imaging of plumes and spectra was performed with ICCD cameras in this dissertation. Intensified Charged Coupled Device (ICCD) cameras permit the imaging of events which occur on very short time scales. The ability to switch the camera on and off quickly is called fast-gating. Most current ICCD's are capable of gating down to 10^{-9} seconds, or ns. Andor iStar and Princeton Instruments PI-MAX ICCD cameras were used with the LAPeX apparatus. The PI-MAX ICCD camera was used for spectroscopy. Two separate iStar ICCD cameras were used for imaging and spectroscopy.

Photons impact the photocathode and liberate electrons that enter the applied

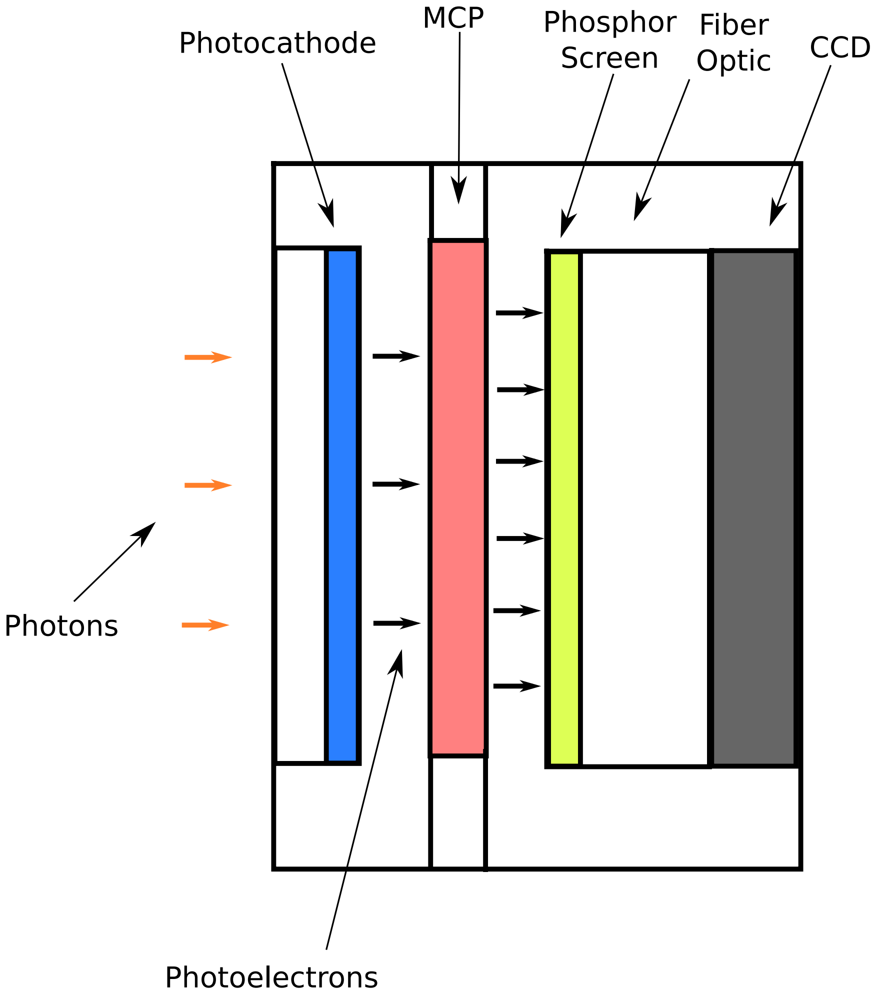

Figure 3.5 Diagram showing the essential components of an ICCD camera.

voltage in the micro-channel plate (MCP). The electrons enter the micro-channels at a slight angle. Each electron then collides with the wall of the channel and liberates additional electrons. This process continues down the length of the channels creating an avalanche effect. One electron entering the MCP can be multiplied to 1×10^6 electrons at the output. This avalanche process produces amplification of the signal entering the ICCD.

The number of electrons emitted from the wall of the channel at each collision is governed by the voltage applied across the MCP. The electrons exiting the MCP strike a phosphor screen. The striking electrons impart kinetic energy to the phosphor molecules and excite electronic states. The emission produced by the de-excitation of the states creates light that is transported by a fiber optic and imaged by a high-quality CCD chip. The resolution of an ICCD camera is governed by the CCD pixel size and the MCP channel density.

3.6 Optical Spectroscopy

Optical spectroscopy provides an important tool for studying plasmas and gases. Optical spectroscopy played an important role in the LAPeX apparatus for the measurement of temperature and density. Three spectrometers with two different ICCD detectors were employed in this system. Table 3.3 shows the specifications for two spectrometers used in the experiments described in this dissertation. A Chromex 500is 0.5 m imaging spectrometer and an Acton SP2500i 0.5 m imaging spectrometer were used. The Andor iStar served as the detector for the Chromex spectrometer. The Princeton Instruments PI-MAX was the detector used with the Acton spectrometer.

Light for each spectrometer was transported from the plume to the instrument using lenses (see Fig. 3.8). All optics used to carry the emitted light to the spectrometer are coated with a broadband anti-reflection coating, and broadband metallic mirrors are used. All spectrometers that were used in this experiment were imaging types that used an ICCD as a detector. The combination of imaging spectrometers and ICCD's provided spatial, temporal, and energy resolution. The spatial field of view of the plume was governed by the spectrometers' entrance slit width. Fig. 3.6 shows the two different imaging configurations used in the experiments. Image B shows spatial resolution along the plume expansion direction. This is useful for observing the effects of background gas on the plume and shock waves. The Acton system was used in this configuration. Image C shows the cross-section view provided by the Chromex system. The variation across the plume in cross section is much less than along the expansion direction. This makes the cross-section view useful for binning over a large number of pixels.

Spectrometer	Chromex	Acton
Gratings	3	3
Grating Specs	1: 100 lines/mm Blazed at 450 nm 2: 2400 lines/mm Holographic 3: 3600 lines/mm Holographic	1: 150 lines/mm 2: 1200 lines/mm 3: 2400 lines/mm
Detector	Andor iStar	Princeton Instruments PI-MAX

Table 3.3 Summary of spectrometer features.

3.6.1 Calibration and Characterization of Spectroscopic Systems

Wavelength calibration was performed before each experimental data set was collected. All fits for wavelength (energy) calibration were calculated using data collected from a Thorlabs HeNe tunable laser, Ar-ion laser, or Newport/Oriel pencil lamp calibration source. Obtaining quantitative data from spectrometers provides a way to measure the temperature and density of the constituent species in the plume. The proper characterization of the components in the system must be known so that it is possible to correct for any problems in the instrumentation. A proper characteriza-

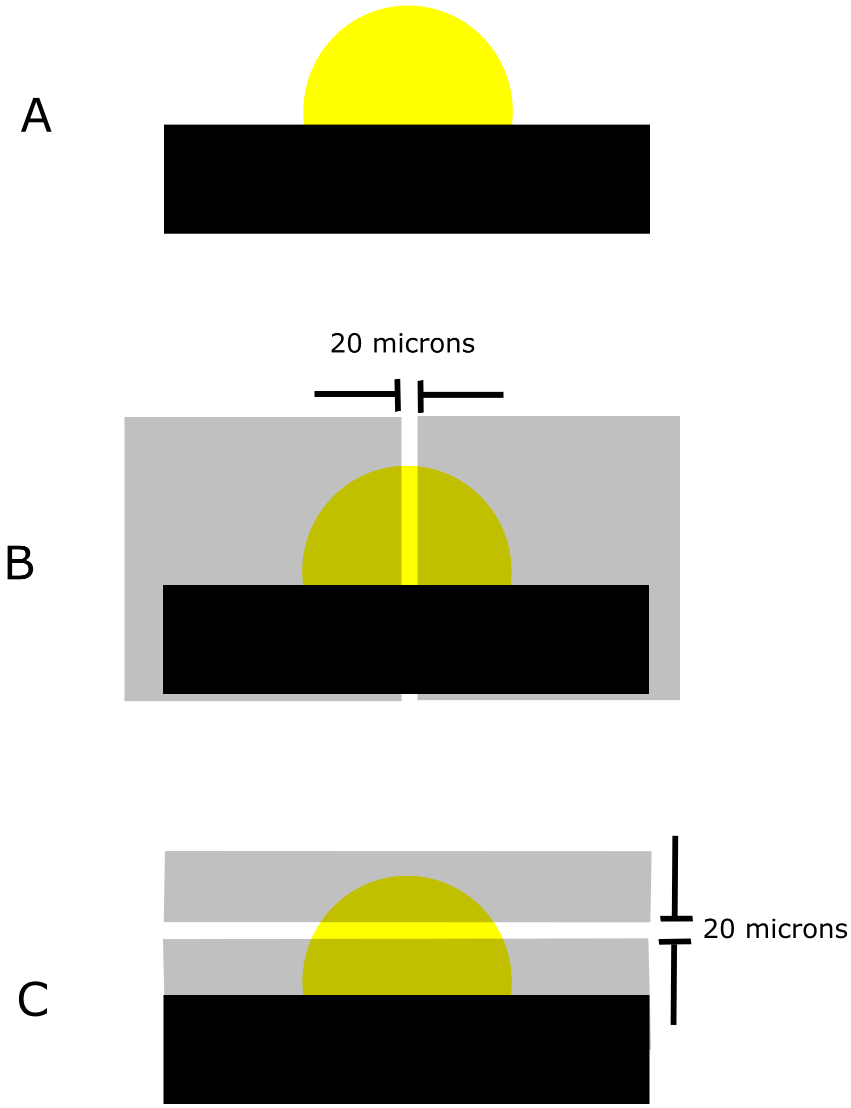

Figure 3.6 Diagram of the plume position on the spectrometer slits: A) shows the plume, B) shows the Acton configuration, and C) shows the Chromex configuration.

tion of a spectroscopic system includes the characterization of the responsivity of the lenses, mirrors, grating, and camera. Light intensity is affected by each of these optical components as a function of wavelength, $I(\lambda)$. Eq. (3.1) shows the relationship between the intensity emitted at the plume and the intensity measured:

$$I_m(\lambda) = R(\lambda)I_e(\lambda). \tag{3.1}$$

I_m is the measured intensity, I_e is the emitted intensity, and R is a responsivity function that is often non-linear.

Measurements of the power at the input and output of the spectroscopic system as a function of wavelength provided the responsivity of the system. This process worked well for a fully fiber-coupled spectrometer. The power of light collected and passed through a fiber optic was measured. That fiber optic was then connected to the spectrometer to make the intensity measurement from the camera. A correlation between the input power and the count intensity measured with the ICCD was then made.

One approach to the flat-field correction, outlined by Williams and Shaddix, finds a polynomial fit for intensity as a function of transmission strength for each pixel [64]. This process flattens the image pixel-by-pixel. The Andor iStar ICCD used in these experiments shows a non-linear response to light intensity. A process similar to the one discussed by Williams and Shaddix was employed to try to correct the iStar's output. This process involved collecting flat-field images using a lamp and integrating sphere. Neutral density (ND) filters were mounted between the output of the integrating sphere and the ICCD. A set of 50 images was collected at each of 11 different ND strengths. The use of the ICCD with no ND filters saturated the image. ND filters were inserted until the counts per pixel came close to the maximum without exceeding it and becoming saturated. The proper attenuation of the light was measured at

ND=0.5. The ND strength was converted to transmission percentage, T, according to Eq. (3.2):

$$T = 10^{-ND}. \tag{3.2}$$

Ideally, the maximum number of counts would correspond to ND = 0. The ND would be increased until the measured number of counts goes to 0. ND=0.5 was subtracted from each ND step to give a shifted ND which gives T = 1.0 at the largest count step. The 50 images for each step were averaged over at each pixel to generate a single image. The following expression is used to average the intensity values of the pixel located at the position (i,j) over the 50 images:

$$I_{ij} = \frac{\sum_{k=1}^{50} I_{i,j,k}}{50}. \tag{3.3}$$

Eq. (3.3) generates a single file for each ND strength. An array of 11 images at 11 different transmission strengths allowed for a set of polynomials to be generated. A polynomial was fit at each pixel with the intensity measured in counts on the x-axis and the transmission measured on the y-axis. A 1,024 x 1,024 pixel CCD chip has 1,048,576 separate polynomials. Any image that requires a correction is adjusted pixel-by-pixel. The counts at each pixel are entered into the polynomial for that pixel location which generates an effective transmission for that pixel. Flattening of the image can be done once this adjustment for non-linearity is completed for each pixel. Eq. (3.4) shows the normalization method used to flatten the image at each pixel:

$$F_i = T_i/T_{max}. \tag{3.4}$$

T_i is the transmission at the i^{th} pixel, T_{max} is the maximum transmission measured in the image, and F_i is the flattened i^{th} pixel.

The method outlined by Williams and Shaddix is able to account for non-linearity in the flat-field of ICCD cameras. ICCD's acting as detectors for spectrometers need additional correction for the efficiency of the diffraction grating and optics. A source with a known and NIST traceable spectrum was used to determine the correction factor needed to adjust experimental data. A quartz tungsten halogen (QTH) 200-Watt lamp (model number 63355), manufactured by Oriel Instruments, was used as the broad spectrum source. This lamp was installed immediately outside of the chamber. All optics, except for the chamber window, which is optically flat UV grade fused silica with a well characterized flat response at measured wavelengths, remained in place to account for all possible sources of variation. A spectrum was collected at the same ICCD gain and center wavelength as the experimental data. The gate window needed to be varied to collect sufficient light from the lamp.

An example of the raw data collected from the QTH lamp is shown in Fig. 3.7. The data is background subtracted, vertically binned, and wavelength calibrated. The resulting spectrum was normalized to its maximum value. See Eqs. (3.5) - (3.8):

$$I_{ij} = I_{ij} - B_{avg}, \tag{3.5}$$

$$I_i = \sum_{j=1}^{N} I_{ij}, \tag{3.6}$$

$$I(\lambda) = P_\lambda(I_i), \tag{3.7}$$

$$I_{norm}(\lambda) = I_i(\lambda)/I_{max}. \tag{3.8}$$

I_{ij} is the intensity at each pixel of the QTH spectral image, B_{avg} is the average background value, and P is the polynomial fit for the wavelength calibration.

The polynomial fit to the NIST traceable values provided by Oriel was normalized to its maximum value ($NIST_{norm}$). The normalized collected spectrum was divided by the normalized NIST spectrum. The resulting curve gives the correction factor as a function of wavelength. A polynomial fit is made to the correction curve to

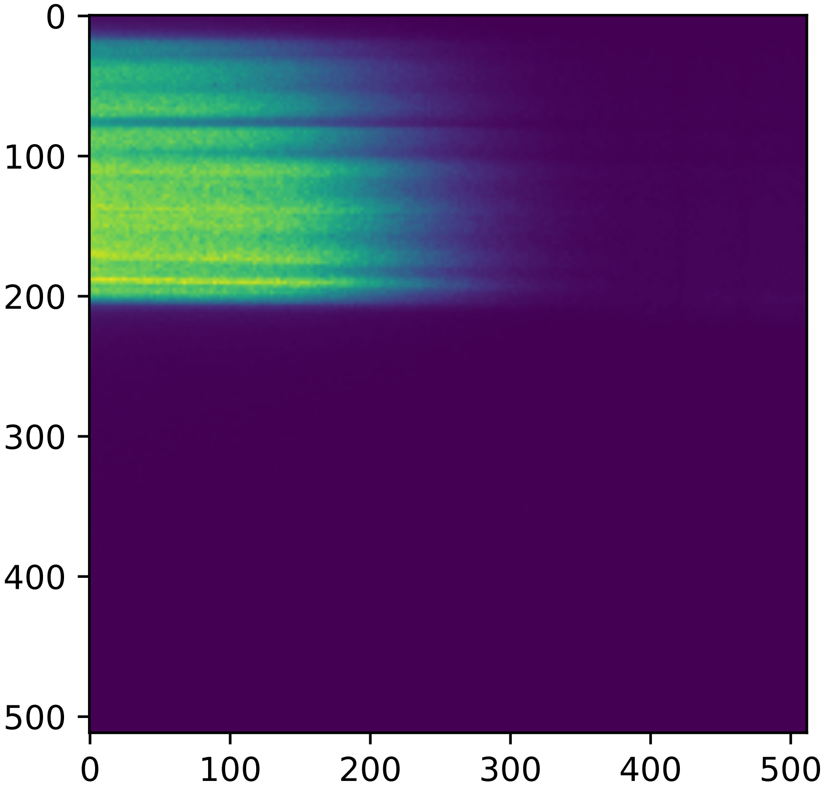

Figure 3.7 This diagram shows the QTH raw spectrum.

yield $C(\lambda)$. Experimental data is then divided by the correction curve polynomial to provide the corrected spectrum. Eqs. 3.9 and 3.10 show the final steps of the correction process:

$$C(\lambda) = Fit(I_{norm}(\lambda)/(NIST_{norm})), \tag{3.9}$$

$$Data_{corrected} = Data/C(\lambda). \tag{3.10}$$

3.7 Optical Density Diagnostics

Electron density is a quantity of critical importance to properly characterize a plasma. Electron density can be measured by using the effect that electrons have on electromagnetic radiation. The index of refraction with a negligible magnetic field is:

$$N^2 = 1 - \omega_p^2/\omega^2, \tag{3.11}$$

with ω as the frequency of light and ω_p as the plasma frequency.

Shadowgraphy and interferometry were employed to measure electron density and to image the plume. A Mach-Zehnder interferometer was constructed. The laser used for both shadowgraphy and interferometry was a “Continuum Minilite” laser. This laser is related to the Powerlite used for ablation. It is an Nd:YAG laser with ~ 5 ns pulses and a maximum energy of 60 mJ per pulse at the fundamental wavelength (1,064 nm). Most data collected with this system used this laser with its frequency doubled to 532 nm. The laser path is shown in Fig. 3.8.

3.7.1 Shadowgraphy

Shadowgraphy is the optical technique of back-lighting a fluid, such as a plasma, gas, or liquid, and looking at how variations in the density and index of refraction of

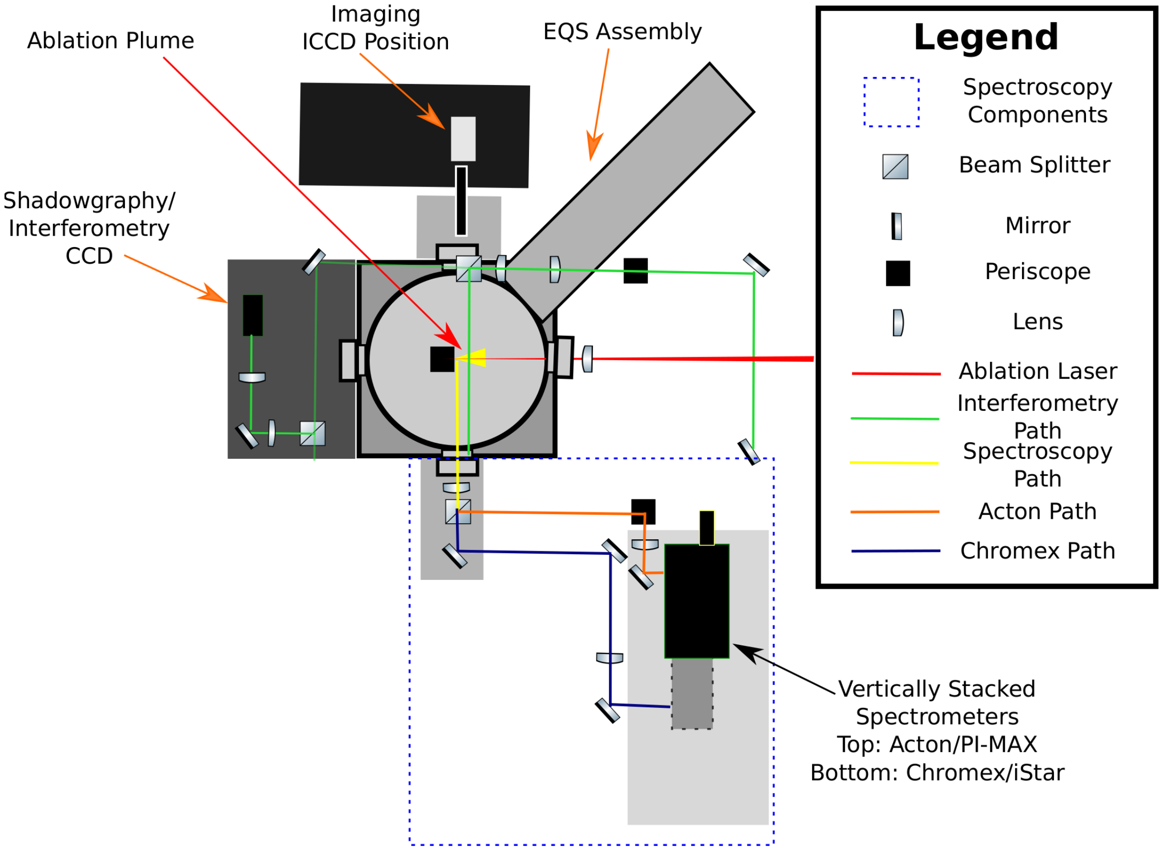

Figure 3.8 Optical path showing components and interaction region for spectroscopy, ICCD imaging, shadowgraphy, and interferometry.

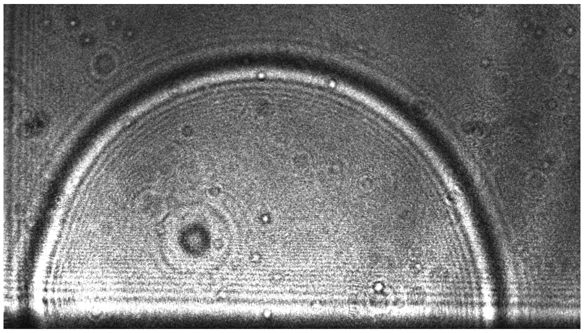

Figure 3.9 Shock wave produced in 99.8 Torr O_2 at t = 5 μs.

the fluid alter the optical rays of the light creating brighter and darker regions. Fig. 3.9 shows an example of a shock wave passing through a rarefied gas background. Shadowgraphy provides a primarily qualitative description of the dynamics of the fluid.

3.7.2 Mach-Zehnder Interferometer

The most direct refractive index density measurement is made using interferometry. The typical densities encountered in the plasmas generated by LAPeX permit the use of a Mach-Zehnder interferometer. The general design of a Mach-Zehnder interferometer is shown in Fig. 3.10. A laser beam is split into two arms with a beam splitter. The electric field, with angular frequency ω, of each arm can be represented as [59]:

$$E_1 = E_0 e^{i\omega t}, \tag{3.12}$$

$$E_2 = E_0 e^{i(\omega t+\phi)}. \tag{3.13}$$

E_1 represents the reference arm and is undisturbed. The second arm passes through the plasma and is represented by E_2. The plasma inserts an additional phase delay, ϕ, into E_2. The two arms are recombined at a second beam splitter. The addition of

E_1 and E_2 gives the total electric field [59]:

$$E_t = (E_1 + E_2 e^{i\phi})e^{i\omega t}, \tag{3.14}$$

and

$$|E_t|^2 = [E_1^2 + E_2^2]\left[1 + \frac{2E_1E_2}{E_1^2 + E_2^2}cos\phi\right]. \tag{3.15}$$

Eq. (3.15) is proportional to the detected power. The $cos\phi$ component varies periodically producing the alternating light and dark interference pattern. The second beam splitter has two separate interference patterns that are 180° out of phase from one another.

The difference in the phase produced by the arm with the plasma is given by [59]:

$$\Delta\phi = \int (k_{plasma} - k_0)dl = \int (N-1)\frac{\omega}{c}dl, \tag{3.16}$$

$$k = N\frac{\omega}{c}. \tag{3.17}$$

The phase is ϕ, l is the path length, N is the index of refraction, ω is the angular frequency of the light, c is the speed of light, and $k_0 = \omega/c$. The integral is limited to the path length through the plasma. Eq. (3.11) can be rewritten as [59]:

$$N^2 = 1 - \omega_p^2/\omega^2 = 1 - n_e/n_c. \tag{3.18}$$

The cutoff density is n_c, and the electron density is n_e. The cutoff density is [59]:

$$n_c = \omega^2 m\epsilon_0/e^2. \tag{3.19}$$

The phase shift at the interferometer is:

$$\Delta\phi = \frac{\omega}{c} \int \left[\left(1 - \frac{n_e}{n_c} \right)^{1/2} - 1 \right] dl. \tag{3.20}$$

Eq. (3.20) simplifies if $n_e \ll n_c$ to:

$$\Delta\phi = \frac{-\omega}{2cn_c} \int n_e dl. \tag{3.21}$$

Light propagates through the plasma if n_e is less than n_c. The interference pattern observed at the output of the second beam splitter will look similar to that seen in Fig. 3.13. The fringes will be shifted by an amount that is proportional to the phase shift, $\Delta\phi$, if a plasma is inserted into one of the arms of the interferometer.

The shadowgraphy/interferometry system in use for LAPeX is highlighted in Fig. 3.8. Figs. 3.11 and 3.12 show the Minilite path through the chamber. The Minilite laser operated at 532 nm. This light was expanded before entering the chamber to fill the vacuum port window. The light passed through a Thorlabs BS-2, a two-inch beam splitting cube, and enters the chamber from the top diagonal port. The beam then passes through the plume and exits through the bottom diagonal port. Both ports had debris shields mounted on the inside of the chamber. Light exited the beam splitter and formed the reference arm. This beam followed a path similar to the diagnostic arm, but passed behind the chamber. The two arms recombined at the lower beam splitter and passed through two lenses to allow adjustment of magnification. A Finger Lakes Instruments CCD camera imaged the interference pattern generated by the recombined beams. The Mach-Zehnder simplifies down to a shadowgraphy system when arm 2 is blocked.

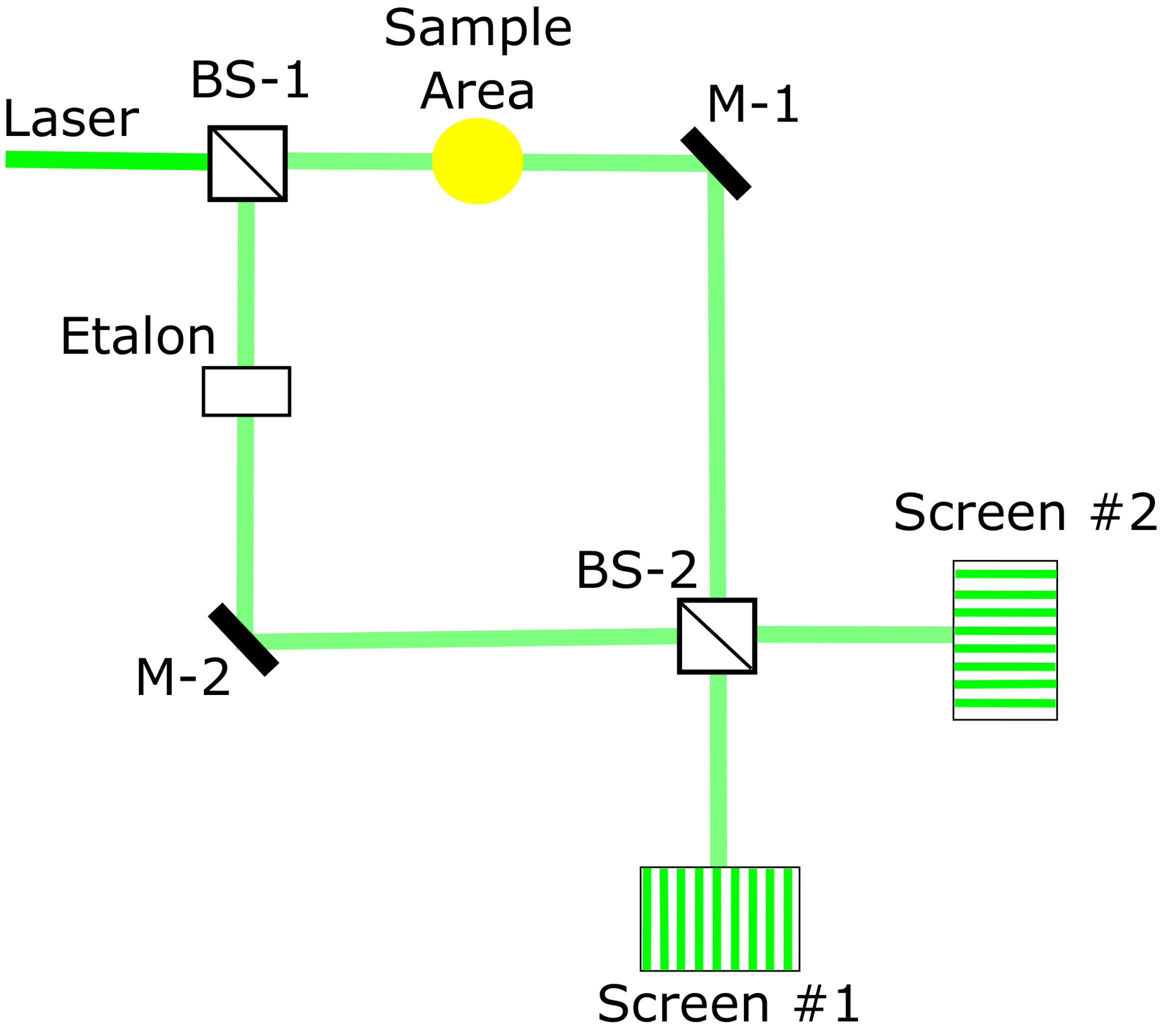

Figure 3.10 This diagram shows a Mach-Zehnder interferometer. BS-1 is the beam splitter which splits the beam, and BS-2 is the beam splitter which recombines the beams. The two recombined beams are 180° out of phase and produce an interference pattern.

Figure 3.11 This diagram shows the path of the Minilite pulse for shadowgraphy/interferometry experiments.

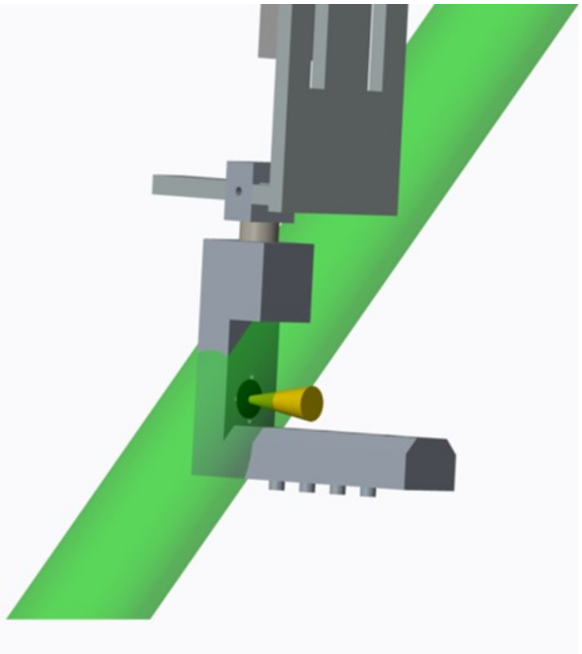

Figure 3.12 This diagram shows the target holder and ablation plume being illuminated by the Minilite pulse for shadowgraphy/interferometry experiments.

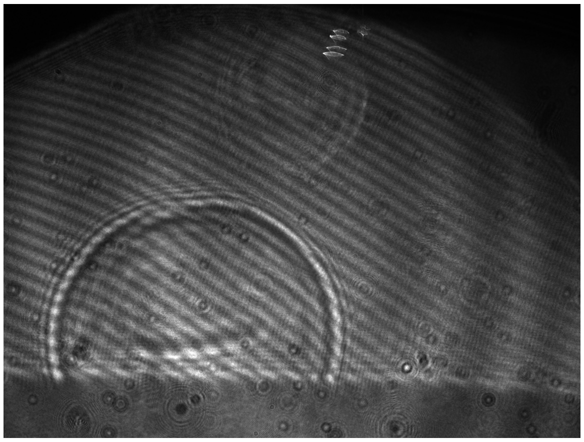

Figure 3.13 This image shows an interferometric measurement of a plume expanding into a rarefied gas background at $t = 200$ ns.

3.8 Charge Measurement

An early experiment carried out with laser ablation involved measuring the replacement current flowing to the target holder after laser irradiation [65]. This experiment involved measuring the voltage on a shielded wire connected to the target holder. That wire was connected to a BNC feedthrough on the vacuum chamber. The signal was then connected to an oscilloscope with a 50 Ω impedance BNC cable. The input impedance of the oscilloscope was set to 50 Ω.

The main difficulty with this measurement was the analysis of the circuit to determine the current due to the characteristic frequency dependence of the impedance as is shown in Eqs. (3.22)-(3.24):

$$V = IZ, \tag{3.22}$$

where

$$Z_L = jL\omega, \tag{3.23}$$

$$Z_C = \frac{1}{j\omega c}. \tag{3.24}$$

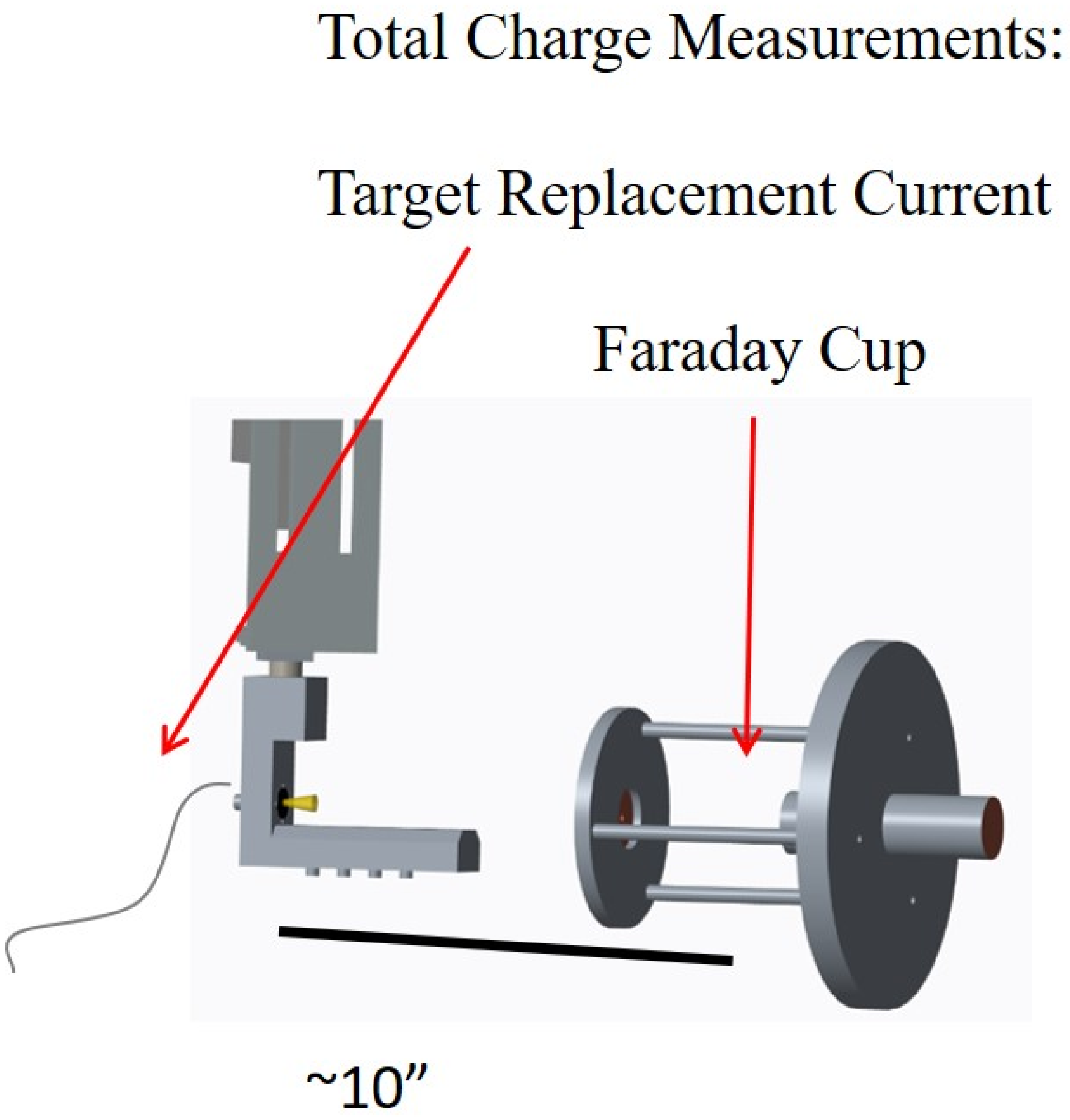

Figure 3.14 This figure shows the typical configuration of the target holder and Faraday cup for current measurements.

V is the voltage, I is the current, and Z is the total impedance. Z_L is the impedance due to inductance, and Z_C is impedance due to capacitance. The frequency dependence is shown as ω. Circuit simulations over a range of characteristic frequencies is needed to determine the current and total charge.

Additional current measurements of the plume were made using a Faraday cup. Typical data from each measurement is shown in Fig. 3.15.

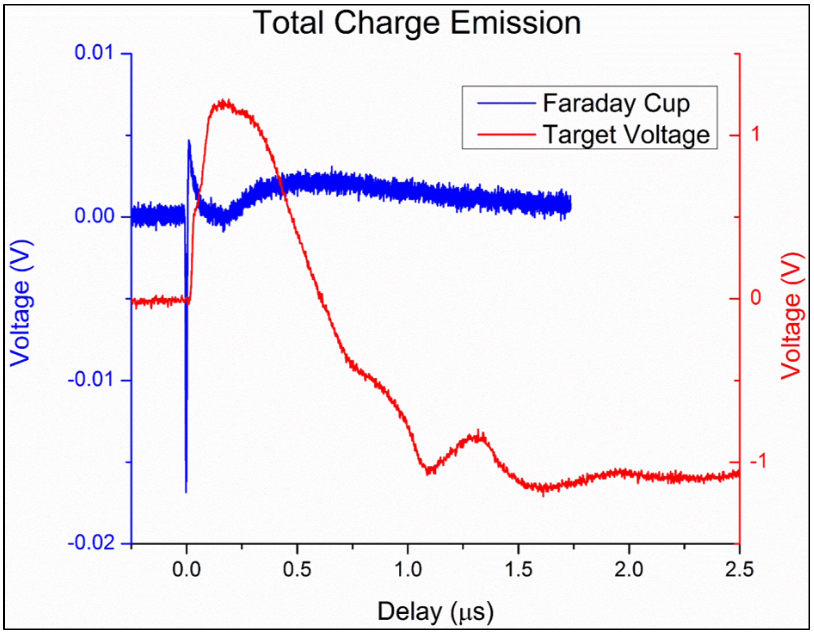

Figure 3.15 Typical data from the target replacement current and Faraday cup measurements.

3.9 Electric Quadrupole Mass Spectroscopy

Mass spectroscopy can be performed on the LAPeX apparatus with an Electric Quadrupole Mass Spectrometer (EQS) system developed by Hiden Analytics. The Hiden HPR-60 MBMS is designed to measure atmospheric plasma and gas phase intermediaries [66]. The system is capable of measuring atoms/molecules with mass up to 300 amu with 1 amu resolution. The 1 amu resolution makes this system ideal for differentiating atomic species and molecular species.

This Hiden system is capable of operating with the inlet pressure at full atmospheric pressure. The system uses the process known as differential pumping to ensure that the pressure at the detector is at 10^{-9} Torr. Differential pumping for this Hiden system uses three separate sections with pinholes along the line of sight from the inlet to the main EQS region. The pinholes limit the gas entering each of the three vacuum pumping stages to ensure that the section with the detector operates at a safe pressure. The vacuum system for the main LAPeX chamber is separated from the vacuum system for the Hiden EQS system by a gate valve.

Examples of data produced by the EQS system when a carbon target was ablated can be seen in Figs. 3.16 and 3.17. The data shown in these figures was collected with the minimum instrumental gate width of 3 ms. The data was collected in 0.1 amu steps with 2 shots per step.

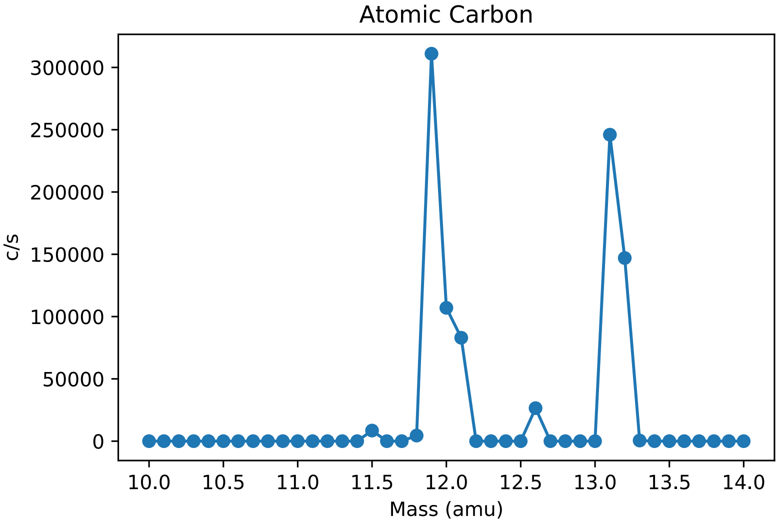

Figure 3.16 Hiden EQS data showing atomic carbon.

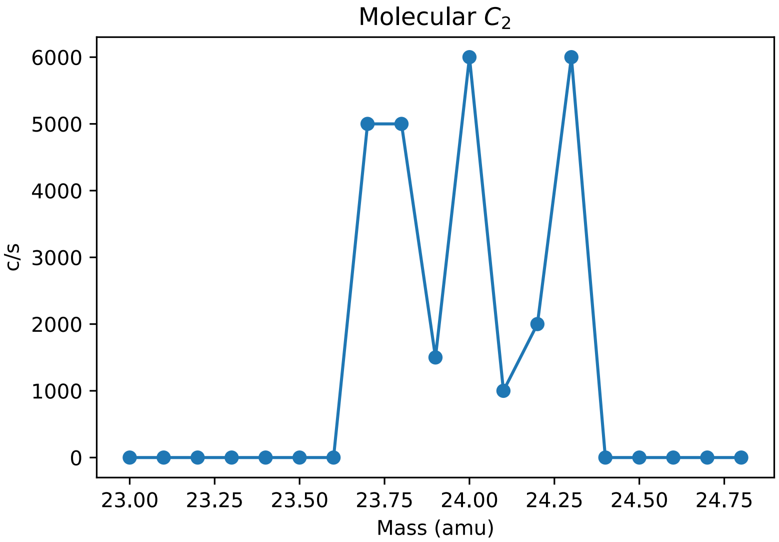

Figure 3.17 Hiden EQS data showing diatomic carbon.

3.10 Timing

The requirement for fast-gating for laser ablation experiments required care in tracking the timing of triggers to the laser and various diagnostics to provide for a t_0. A central triggering scheme was implemented to send triggers at the proper times. LAPeX used the time that the laser irradiated the target as t_0. The measurement of cable delays and light travel times were necessary to know when to trigger each diagnostic. Digital delay generator settings for each imaging diagnostic were determined by capturing an image of the laser pulse irradiating the target. Tables 3.4 and 3.5 show the delays programmed into the digital delay generators. A Stanford Research Systems DG645 digital delay generator was set to an internal trigger at a repetition rate of 10 Hz, or one pulse every 100 ms. That delay generator triggered the flash-lamps of both lasers. A hand-held trigger switch was installed between the first DDG and a second DG645 and was used to trigger the diagnostics. Fig. 3.18 shows the interconnection between the DDG's and the diagnostics that were triggered.

Channel	Diagnostic	Delay
A	Powerlite Q-Switch On	t + 305 μs
B	Powerlite Q-Switch Off	A + 10 μs
C	Minilite Q-Switch On	E - 140 ns
D	Powerlite Q-Switch Off	C + 50 ns
E	Andor ICCD (Chromex)	A + 110ns
F	Andor ICCD (Imaging)	E - 123 ns
G	FLI CCD	A - 40 ms
H	PIMAX ICCD (Acton)	E - 357 ns

Table 3.4 This table gives the delays programmed into the digital delay generator for each diagnostic.

Channel	Diagnostic	Delay
A	Powerlite Flashlamp On	0 μs
B	Powerlite Flashlamp Off	A + 10 μs
C	Minilite Flashlamp On	125 μs
D	Powerlite Flashlamp Off	C + 15 μs

Table 3.5 This table gives the delays programmed into the digital delay generator for the flashlamps in the Powerlite and Minilite lasers.

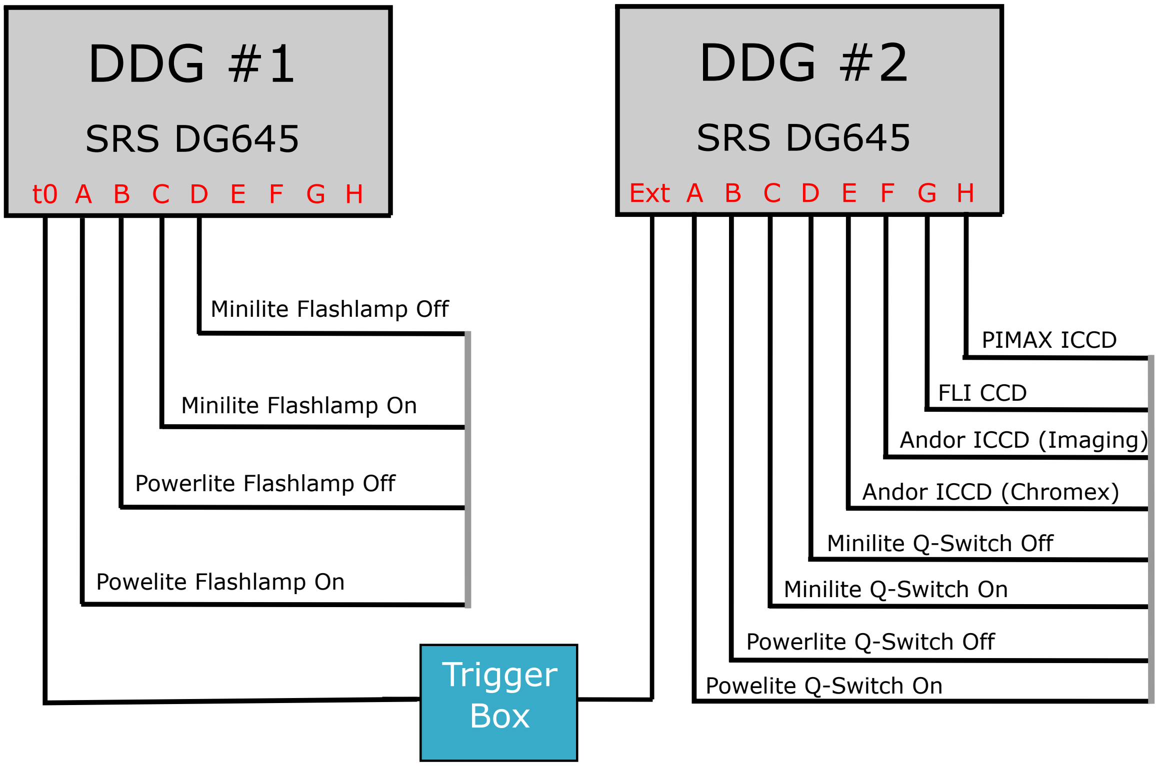

Figure 3.18 This figure shows the cable connections for the digital delay generators.

Chapter 4

Molecular Carbon Absorption Spectroscopy

4.1 Introduction

Carbon is a common element in the universe with a long history of research. Carbon plasma has been generated using carbon-arc lamps and lasers. Laser ablation generates carbon plasma from targets such as graphite and plastics. The popularity and importance of carbon has generated a large number of research papers looking at its emission spectrum [32,67–71]. Diatomic carbon, or C_2, has been studied using optical spectroscopy. The Swan band system shows up in the visible part of the spectrum, and one of the more prominent vibrational transitions ($\Delta v = 0$) exists in the blue-green part of the spectrum. Swan bands have been studied for over a century and a half and play a prominent role in research in astrophysics and combustion chemistry [72]. LIBS is used to identify carbon molecules in test samples, and LAMIS is used to determine the isotopic ratios between carbon isotopes for radiocarbon dating [31,32,73,74]. Swan bands have been observed in the tails of comets, such as Halley's Comet, and in stellar atmospheres [75]. DQp white dwarfs have a carbon rich atmosphere [76].

The Swan bands correspond to the $d^3\Pi_g - a^3\Pi_u$ transition of C_2. The lower state in this transition is not the ground state but is a state with slightly higher energy. Other band systems can be found in the near-infrared and near-UV.

Emission spectroscopy is one of the most important tools available to astronomers, chemists, and physicists. An object of interest can be studied using emission spectroscopy if it is emitting light. A detailed knowledge of populated state distributions becomes important to understanding and analyzing the spectra. Another tool that can be used is absorption spectroscopy. Absorption spectroscopy studies the lines of a continuum spectrum that are missing instead of looking for spectral lines emitted by a radiating plasma, liquid, or gas. The value of such a diagnostic tool is the ability to detect atomic and molecular species even if they are in the ground state and are not radiating.

Absorption spectroscopy is used extensively in astronomy and astrophysics. A plasma or gas is back-lit with a broad spectrum light source, usually a star, and absorbs wavelengths according to what atoms, ions, and molecules are present. Absorption spectroscopy is also used for studying chemical solutions. One of the primary difficulties with using absorption spectroscopy with laser ablation is the transient nature of the plume compared to most light sources used as a probe. Creating a pulsed white light probe for absorption spectroscopy requires a large amount of optical power. Xenon and halogen lamps will provide the proper spectrum, but they are usually not able to be switched on and off quickly enough and with sufficient intensity to be useful on the nanosecond to microsecond scale.

One solution to the optical power problem is the use of a supercontinuum white light laser. The supercontinuum (SC) effect is generated when a short pulse laser irradiates a transparent material. The laser excites a large number of states in the

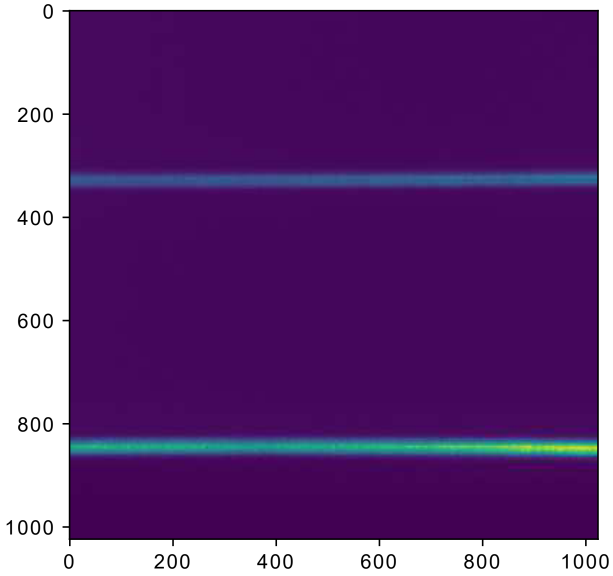

Figure 4.1 This picture shows an example of the output from the spectrometer. This image is taken with no plume present. The top beam is Beam 1, and the bottom beam is Beam 2.

material and generates a quasi-white continuum. Laser light is sent through a fiber in an SC laser. The output of the fiber is a spectrally broad and coherent beam of light. The beam can have high optical power due to its coherence. An SC laser makes a perfect probe for use in laser ablation plume absorption spectroscopy.

NKT Photonics offered to provide a SuperK EXTREME supercontinuum laser as a demo for this experiment [77]. This laser is not pulsed, but it was decided that a combination of this SC laser and an ICCD camera for gated imaging of the absorption spectrum would work to test the concept. This chapter will describe the use of a quasi-CW SC laser to generate a probe beam for the absorption spectroscopy of a carbon laser ablation plume.

4.2 Experimental Design

This experiment used the LAPeX apparatus with the addition of an NKT Photonics SuperK EXTREME supercontinuum laser [77]. The SC laser was capable of producing a continuous spectrum for wavelengths greater than ∼480 nm. The SC laser's spectral range matched the spectral range that could be detected with the spectrometers on LAPeX. Laser ablation targets consisted of 1 mm thick sheets of DFP semi-conductor grade graphite attached to the target holder using cyanoacrylate adhesive. The Continuum Powerlite laser operated at the fundamental Nd:YAG wavelength of 1,064 nm.

Energy	3.0 J
Pulse Width	9 ns
Spot Size	1 cm
Intensity	4.2×10^8 W/cm^2

Table 4.1 Ablation laser parameters.

Spectroscopy was conducted using the Chromex/Andor iStar system. Low resolution surveys were conducted to determine the best experimental parameters including ICCD gate width, ICCD gain, and the SC laser's stability. The first experimental measurements were made by using a single beam from the SC laser. This beam was steered through the ablation plume and into the spectrometer. An image was captured with the plume present, and a second image was collected without a plume present to provide for a subtraction of the SC light from the absorption spectrum. Shot-to-shot variation of the spectral power was too large to have a good subtraction with this approach.

The SC beam was split using a 1-inch non-polarizing cube beam splitter to correct the shot-to-shot variation. One beam was sent through the plume to the spectrometer while the other beam passed below the plume to the spectrometer undisturbed (see Fig. 4.2). The only spectral difference between the two beams was the presence of the plume in the top beam which created absorption lines. The two beams were offset by ∼8 cm and were positioned ∼1 cm in front of the target surface. The two beams were imaged onto the entrance slit of the Chromex imaging spectrometer. This setup provided two separate spectra in a single ICCD image. Plume self-emission was captured in parallel. Post-processing of the images was necessary to cutout the two regions with supercontinuum light, and the region where the self-emission of the plume was observed.

Total pulse-to-pulse power output of the SC laser was found to be consistent as is shown in Fig. 4.3. Wavelength dependent pulse-to-pulse power output was found to vary widely at any single wavelength. The SC laser oscillator operated at 80 MHz. A measurement of the oscillation frequency can be seen in Fig. 4.3. The oscillation frequency was measured from the voltage output of a Thorlabs DET025A photodiode. Increasing the ICCD gate width to 500 ns for each ablation shot became necessary to ensure a proper averaging over many pulses. Approximately 71 SC pulses were collected during the 500 ns collection time. The 500 ns gate reduced the temporal resolution of the spectra, but this reduction was not a major restriction since the molecules under study exist for at least several microseconds.

Low resolution surveys showed that it was difficult to observe atomic absorption spectra even when atomic emission was easily observed. The 500 ns collection time provided sufficient time for the atomic species to evolve from ions to neutral atoms to molecules. Any particular ion, or neutral atom, would only exist and interact with the probe beam photons for a fraction of the 500 ns window. The photons at those wavelengths would not be absorbed after that time and would be detected at the spectrometer. The atomic absorption lines were then filled in, which made discerning

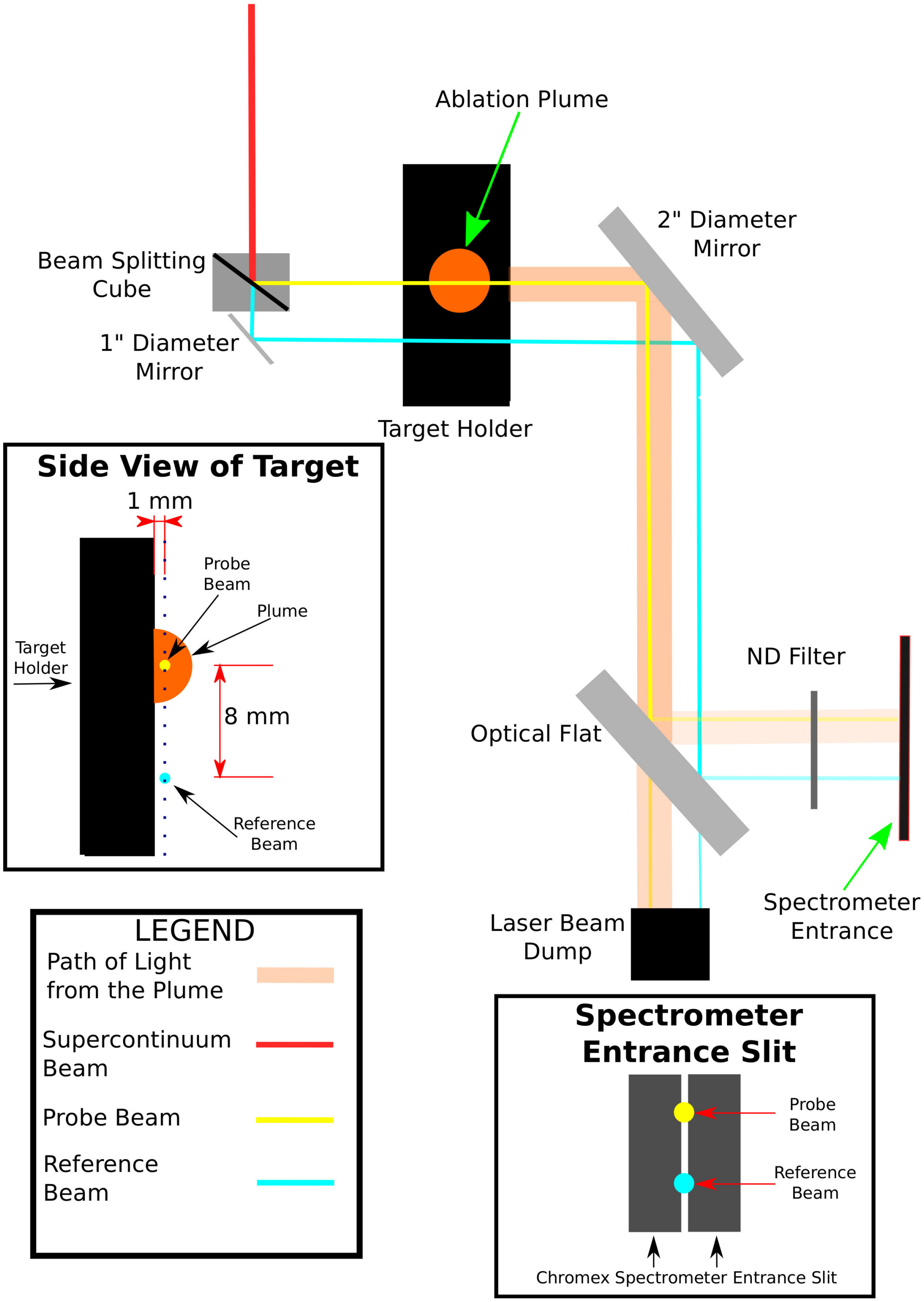

Figure 4.2 This is a schematic of the optical paths of the supercontinuum beams.

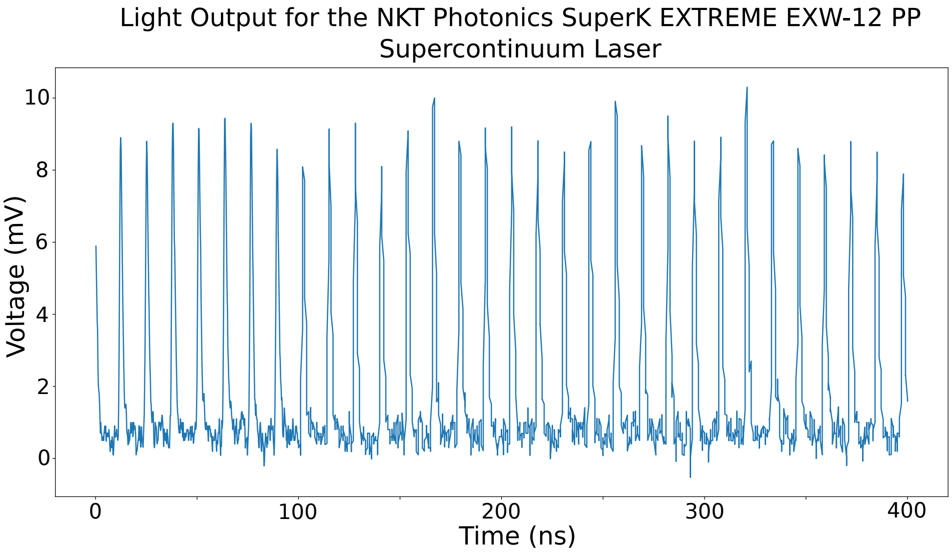

Figure 4.3 This plot shows the oscillation frequency of the NKT Photonics SuperK EXTREME oscillator as measured on a Thorlabs DET025A photodiode. This laser oscillates at 80 MHz which produces a 5 ns pulse of light every ∼12 ns.

atomic absorption lines difficult.

Delay	500 ns
Gate	500 ns
Gain	255
CCD Exposure	2 ms

Table 4.2 Andor iStar ICCD parameters for C_2 data.

Molecular spectra were much easier to observe. Molecules existed for all of the 500 ns collection window and had a much higher density of states. The final focusing lens for the ablation laser was driven 5 cm closer to the target to de-focus the laser spot on target to reduce the laser intensity on target. Previous emission spectroscopy experiments had shown that C_2 molecules could be “chipped” off from the laser target with laser intensities on the order of 1.0×10^8 W/cm^2. Laser intensities larger than that created a hotter plasma, and C_2 molecules were broken apart. The 1-cm focal spot also produced a larger plume that made it easier to align the SC laser beam. A 500 ns ICCD trigger delay was used to ensure that any atomic spectra produced early in the ablation process had time to evolve and die out. The absorption spectrum was collected from 500 ns to 1,000 ns (1 μs). Fig. 4.4 shows the position of the shock wave as a function of time for a carbon ablation plume. The absorption data collected from 500 ns to 1,000 ns was collected in a region of the plume where the shock wave had already passed. Counting statistics were improved by accumulating the data over 30 separate laser ablation shots.

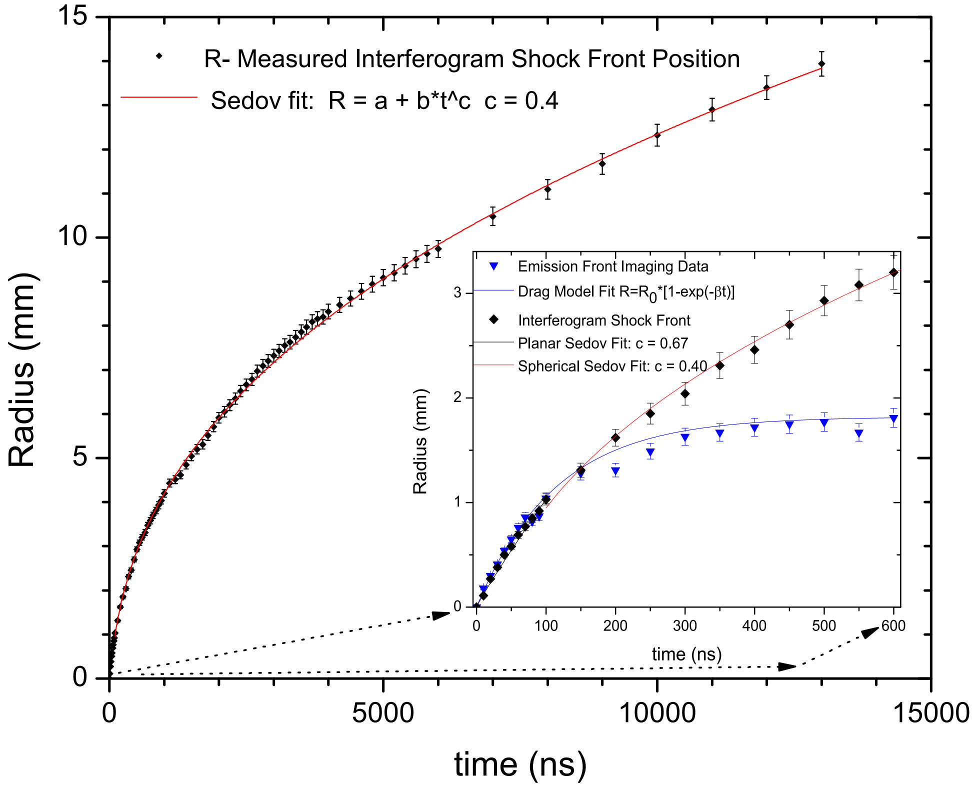

Figure 4.4 This is a plot of the position of a carbon ablation shock wave front as a function of time.

Fig. 4.2 shows a schematic of the elements in the optical line of the SuperK EXTREME SC laser. The SC laser was set to emit at approximately 1 W. The cube beam splitter split the light such that the top beam that passed through the ablation plume had 32% of the original beam power, and the bottom beam had 68% of the original power. This power split worked out to approximately 312 mW for the top beam and 664 mW for the bottom beam. The beam was attenuated two different times to reduce the power incident on the spectrometer. Some power loss was experienced due to debris shields in the vacuum chamber and the chamber windows. An optical flat was used as a mirror after the chamber to steer the beams into the spectrometer. This optical flat was uncoated and reflected approximately 10% of the beam power. The remaining 90% of the power passed through the optical flat into a laser beam dump. The reflected beams then passed through an ND filter with an optical density of 1.6 (2.5% transmission). The combination of the reflection off of the optical flat and the transmission through the ND filter reduced the laser power to 0.25% of the power that was incident on the optical flat.

4.3 Analysis

Data collected by the Chromex spectrometer required multiple data reduction steps to obtain a final result. Each spectral data image contained regions with the supercontinuum beams and the plume self-emission. All programs for analysis were written and carried out using Python. The Python modules Numpy, Scipy, and Matplot were used.

High resolution spectroscopic data was collected in 8 separate steps. Each step corresponded to a different center wavelength with an overlap of $\sim$ 2.5 nm with the previous step. The steps began at a center wavelength of 470 nm and ended at 519 nm. Each step was approximately 8 nm wide. These steps fully covered the $\Delta v = 0$ transition and part of the $\Delta v = 1$ transition. A background image, undisturbed supercontinuum reference image, self-emission image, and absorption image were taken at each step. Fig. 4.5(a) shows an example of an undisturbed reference image. No plume was present. The reference image was used to compare the power from the two beams. The absorption image was the image taken with a plume present. The top SC beam passed through the plume, and the bottom beam was the spectral reference. The self-emission image had no SC light and showed only the emission from the plume. Fig. 4.5(b) shows an example of absorption data. Fig. 4.5(c) shows an emission image.

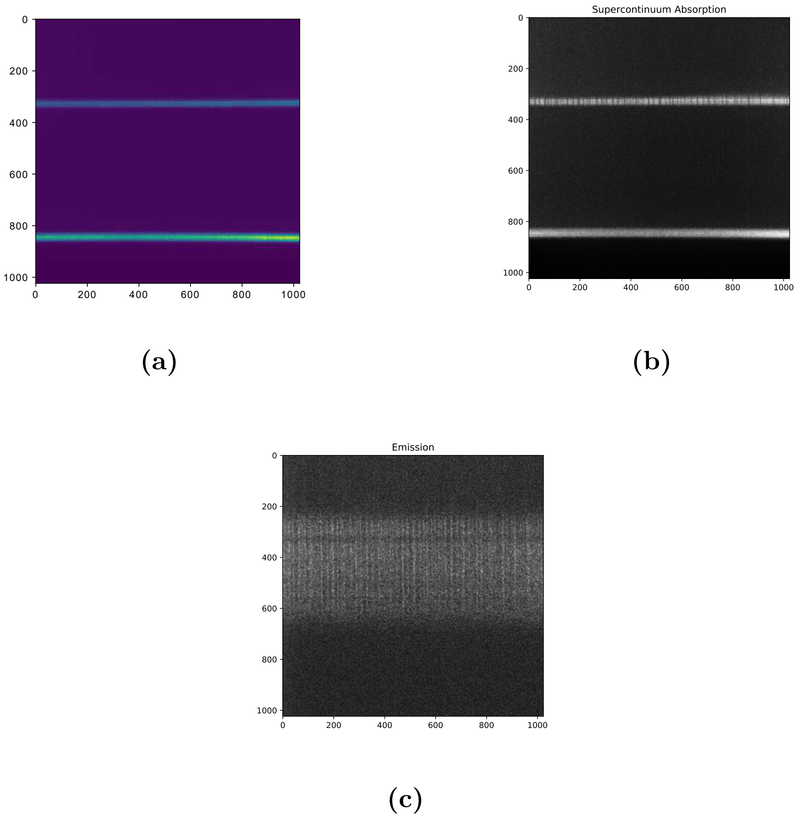

(a)

(b)

(c)

Figure 4.5 (a) Reference image with no plume present. (b) Absorption image showing molecular absorption in the top beam. (c) Emission image showing molecular emission.

Four separate images of spectra at each center wavelength were used in the analysis process:

A. **Background**: The background image taken by the ICCD with no light present.

B. **Reference**: Image with both SC beams and no plume (Fig. 4.5(a)).

C. **SC**: Image with both SC beams and the plume (Fig. 4.5(b)). The top beam is the absorption beam. The bottom beam is the reference beam.

D. **Emission**: Plume emission only (Fig. 4.5(c)).

The data analysis process for each center wavelength followed the following steps:

1. The average background pixel value was calculated from the **Background** image and was subtracted pixel-by-pixel from the other 3 images.
2. A 50-pixel tall section was cut from the **SC** and **Reference** images at both the top and bottom beams.
3. A 50-pixel tall section was cut from the **Emission** image in a region between the SC beams.
4. A wavelength calibration was applied using a linear polynomial fit to Ne and Xe lamp data.
5. A ratio between the top region and the bottom region was found for the **Reference** image. This ratio compensates for the laser beam splitting cube ratio and any sensitivity variations between the top and bottom of the camera. At this stage, each region was vertically binned to generate 3 separate 1-D arrays of length 1,024.
6. The ratio was applied to the **SC** image data.
7. A polynomial fit of the undisturbed **SC** image reference spectrum was produced. This polynomial fit was substituted for the SC reference spectrum to reduce noise introduced into the final data.

8. The final absorption spectrum was found using Eq. (4.1).

$$Absorption = SC\ \ Absorption - SC\ \ Reference\ \ Polynomial - Emission \tag{4.1}$$

Equation (4.1) is appropriate because the plume was optically thin during the data collection window from 500-1,000 ns after irradiation. The full radiation transfer equation is given by Eq. (2.150) in Chapter 2 [59, 61–63]:

$$\mu \frac{dI_{\nu\mu}}{dz} = -\kappa_\nu(z) I_{\nu\mu}(z) + j_\nu(z), \quad \mu = cos\theta. \tag{4.2}$$

$I_{\nu\mu}$ is the intensity at frequency ν, and j_ν is the emissivity of the material at frequency ν. The opacity at frequency ν, κ_ν, of a material approaches 0 ($\kappa_\nu \to 0$) if the material is optically thin. The plume can be considered optically thin if the optical depth is less than 1, $\tau_\nu < 1$. Eqs. (4.3)-(4.4) describe the optical depth [63]:

$$\tau_\nu = \int \kappa_\nu dx, \tag{4.3}$$

$$\tau_\nu = \frac{L}{d_\nu}. \tag{4.4}$$

L is the total length integrated over dx, and d_ν is the mean-free path of a photon. The optical depth can also be described as [63]:

$$\tau_\nu = \frac{\pi e^2}{mc} N_i f_{ij} \phi_\nu L = \sigma_\nu N_i L = \kappa_\nu L, \tag{4.5}$$

where N_i is the species density, f_{ij} is the transition oscillator strength, ϕ_ν is the line shape, and σ_ν is the absorption cross section.

Mach-Zehnder interferometry collected for similar ablation events in vacuum yielded electron densities at or below $n_e \sim 2.0 \times 10^{18}$ cm^{-3} for time steps at 100 ns, 150 ns, 200 ns, 250 ns after laser irradiation. All Mach-Zehnder analysis was completed using the IDEA (Interferometrical Data Evaluation Algorithms) package of codes, version 1.730, developed at the Graz University of Technology [78–80]. IDEA was used to calculate the phase shift between the interference pattern collected with a plume present and a second reference interference pattern collected with no plume present. IDEA reduced the data down to a two-dimensional phase map and a two-dimensional areal density map. The width of the plume at the location of the SC beam at these time steps was $L \sim 0.5$ cm. An average volumetric density was then calculated at each time step. Fig 4.6 shows the density at each time step. The primary source of error came from noise generated by slight differences in fringe position between the reference image and the data image. The percentage error increased as t increased because the shift of the interference fringes due to electrons in the plume decreased and became closer in magnitude to the noise.

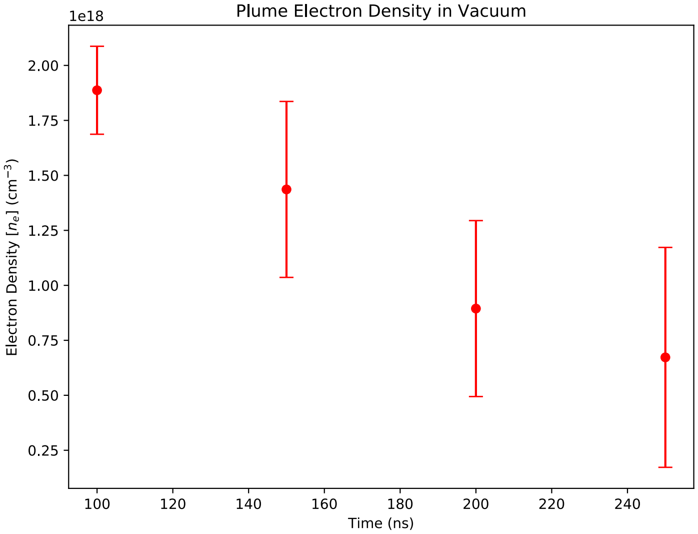

Figure 4.6 The electron density, n_e, at t=100, 150, 200, and 250 ns in vacuum.

The optical depth was calculated by using Eq. (4.5), $\tau_\nu = \sigma_\nu N_i L$. A maximum absorption cross section, σ_ν, for the Ballik-Ramsay C_2 bands was used for the calculation due to difficulty finding the cross section for the Swan band transitions [81]. A maximum optical depth of 0.38 ($\tau = 0.38$) was found at $t = 100$ ns. The plumes observed with SC absorption spectroscopy expanded more slowly reaching $L = 0.3$ cm by $t = 1,000$ ns. Calculating the optical depth with $L = 0.3$ cm yielded a maximum of $\tau = 0.23$. Fig. 4.7 shows the maximum optical depth at each time step.

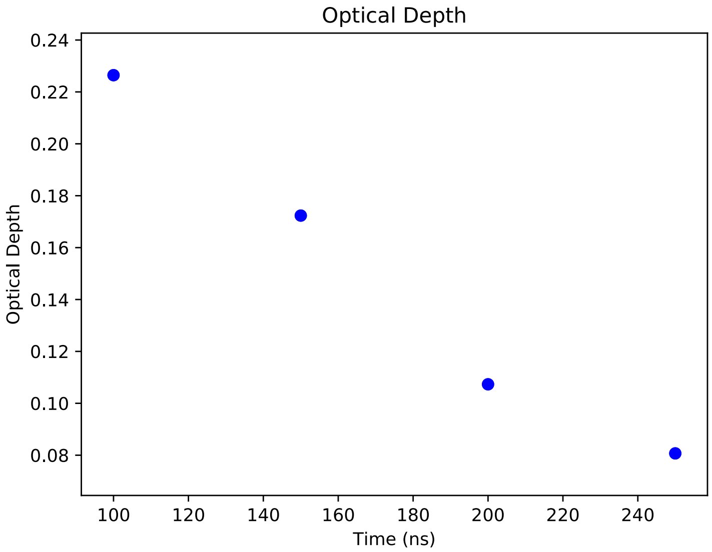

Figure 4.7 The optical depth for $L = 0.3$ cm at t=100, 150, 200, and 250 ns in vacuum.

The density calculated using the Mach-Zehnder interferometer is slightly higher than $n_e \sim 3.5 \times 10^{17}$ cm^{-3}, which was calculated by Harilal et al. under similar experimental conditions [82]. Harilal et al. used a greater laser intensity ($\sim 10^{-10}$ W/cm^2), but their density measurement was made using Stark broadening of the C II line at 391.9 nm. The Mach-Zehnder interferometer detects all electrons present in the plume. Some electrons were produced by the ionization of C atoms while others were produced by thermal emission from the hot target surface. The Mach-Zehnder interferometer density measurement provided an upper limit for the density in the plume. The optical depth was less than 1.0 for $t \geq 100$ ns. The density and optical depth both decrease as the time after laser irradiation increases, which demonstrates that the plume is optically thin and that the opacity does not need to be included in the radiation transfer equation for $t = 500 - 1,000$ ns. Only the emission term, j_ν, remains. Eq. (4.1) only needs to account for the plume's emission and the SC reference to calculate the final absorption spectrum. Eq. (4.2) can be solved analytically to give Eq. (4.6) in the case of radiation incident on the plume:

$$I_\nu = I_{0_\nu} e^{-\kappa_\nu L} + \frac{j_\nu}{\kappa_\nu}(1 - e^{-\kappa_\nu L}). \tag{4.6}$$

The term $I_{0_\nu} e^{-\kappa_\nu L}$ describes the incident probe radiation, and the term $\frac{j_\nu}{\kappa_\nu}(1 - e^{-\kappa_\nu L})$ describes the emission and opacity effects of the plume. The second term may be simplified in the optically thin limit [63],

$$\frac{j_\nu}{\kappa_\nu}(1 - e^{-\kappa_\nu L}) = \frac{j_\nu}{\kappa_\nu}[1 - (1 - \kappa_\nu L + ...)] = \frac{j_\nu}{\kappa_\nu}[\kappa_\nu L + ...] = \frac{j_\nu}{\kappa_\nu}\kappa_\nu L = j_\nu L, \tag{4.7}$$

to give Eq. (4.8):

$$I_\nu = I_{0_\nu} e^{-\kappa_\nu L} + j_\nu L. \tag{4.8}$$

$I_{0_\nu} e^{-\kappa_\nu L}$ becomes I_{0_ν} in the optically thin case ($\kappa_{nu} = 0$). The emergent intensity from the plume in the optically thin case is:

$$I_\nu = I_{0_\nu} + j_\nu L. \tag{4.9}$$

The term $j_\nu L$, in Eq. (4.9), is equivalent to the *Emission* term in Eq. (4.1). $I_{0_\nu} > I_\nu$ where absorption occurs since I_{0_ν} is the SC reference beam intensity. The absorption with the intensity contributed by the SC probe laser subtracted away is defined as

Absorption in Eq. (4.1) and is given by Eq. (4.10),

$$Absorption = I_\nu - (I_{0_\nu} + j_\nu L), \tag{4.10}$$

which is equivalent to Eq. (4.1):

$$Absorption = SC\ \ Absorption - SC\ \ Reference\ \ Polynomial - Emission. \tag{4.11}$$

Extensive effort was employed to apply the proper corrections for ICCD camera irregularities. Attempts included applying non-linear flat-field corrections to the data and producing polynomial fits to the flat-field data. These methods introduced noise and artifacts into the data. The subtraction of the SC reference spectrum from the absorption SC spectrum was found to provide a sufficient correction to the data for any flat-field irregularities. The flat-field for the Andor iStar camera was reviewed to confirm that any variations from left to right on the camera were the same for the top and bottom cutout regions.

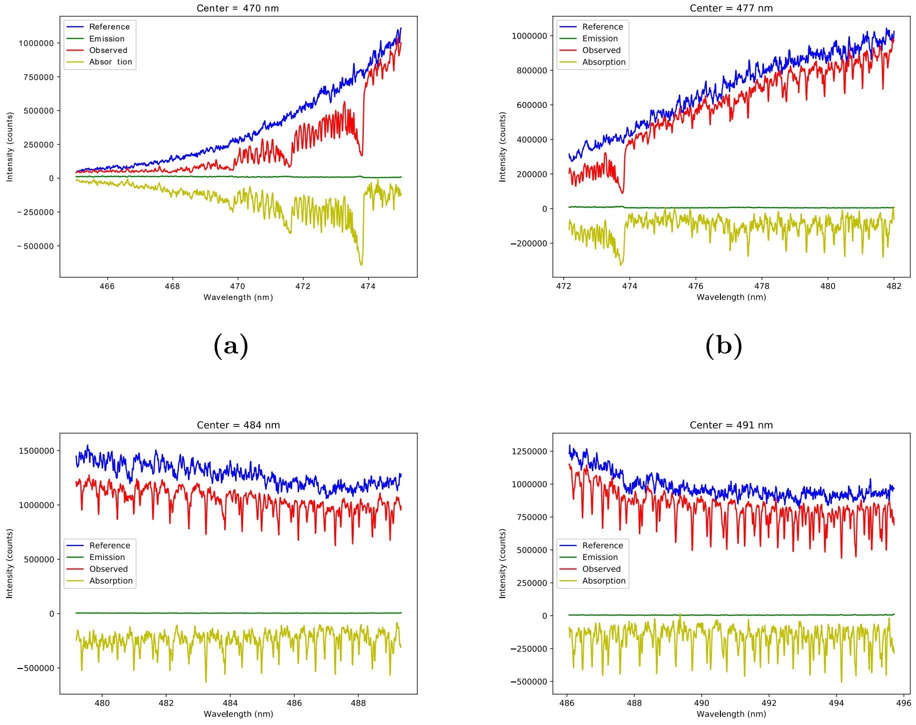

(a)

(b)

(c)

(d)

Figure 4.8 Plots of the first four of eight total separate center wavelength positions showing the observed spectrum, reference, self-emission, and the final calculated absorption spectrum.

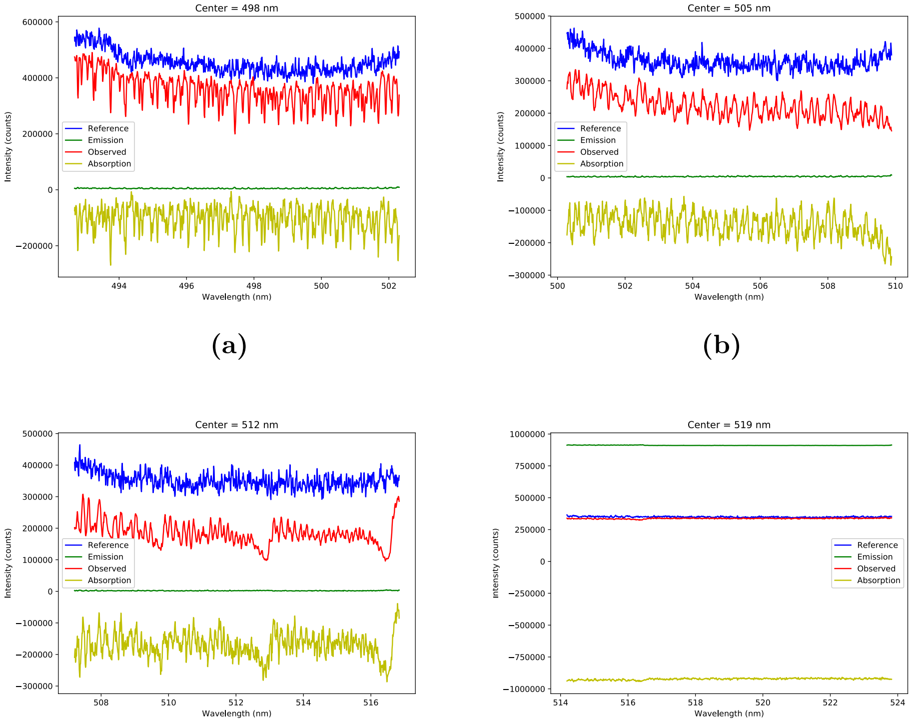

(a)

(b)

(c)

(d)

Figure 4.9 Plots of the remaining four separate center wavelength positions showing the observed spectrum, reference, self-emission, and the final calculated absorption spectrum.

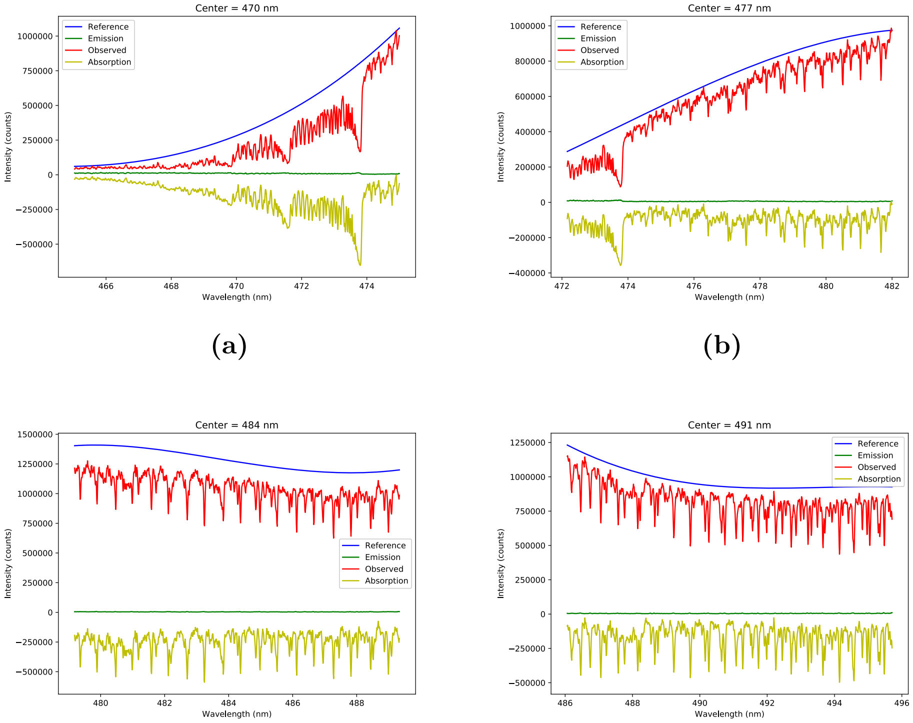

(a) **(b)**

(c) **(d)**

Figure 4.10 Plots of the first four of eight total separate center wavelength positions showing the smoothed observed spectrum, reference, self-emission, and the final calculated absorption spectrum.

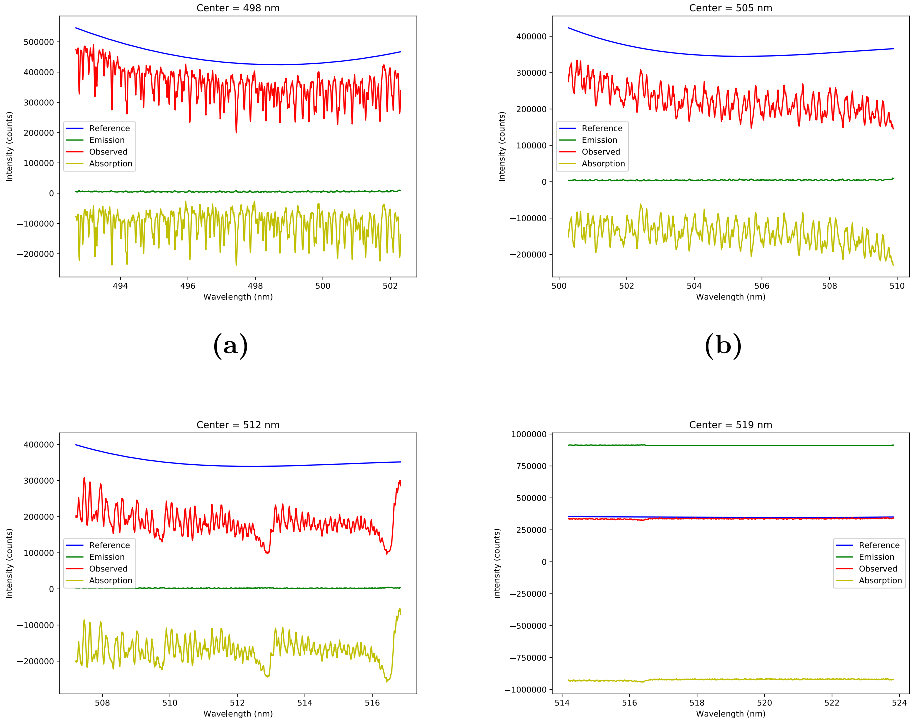

(a) **(b)**

(c) **(d)**

Figure 4.11 Plots of the remaining four separate center wavelength positions showing the smoothed observed spectrum, reference, self-emission, and the final calculated absorption spectrum.

4.4 Spectroscopic Modeling

Modeling of the C_2 Swan bands was important to bound the temperature measurements. PGOPHER was used to model the molecular spectra. PGOPHER is a general-purpose program developed by Colin Western at The University of Bristol's School of Chemistry to model a range of molecules [83, 84]. The reader is directed to the website maintained by Professor Western, as well as several journal articles, for a complete discussion of PGOPHER [83, 84].

PGOPHER is capable of modeling linear molecules, as well as symmetric and asymmetric tops. A large number of different interactions can be included in the simulations including allowed and forbidden transitions, multiphoton and Raman spectra, and external electric and magnetic fields. Electric dipole transitions were used for the simulations in this dissertation. PGOPHER calculates the energies and wavefunctions for the excited and ground states, then calculates the transition parameters. Molecular constants are entered into the simulation to generate the state energies. PGOPHER calculates the Hamiltonians for each transition.

PGOPHER requires that S, the overall electron spin, as well as the vibronic symmetry (Σ^+, Σ^-, Π, etc.), and gerade (g) or ungerade (u) symmetry be specified for each vibronic state [84]. The projection of the angular momentum on the molecular z-axis, $N = J - S$, is implicitly given by the molecule's symmetry. PGOPHER uses a Hund's case (a) basis. The standard basis contains $2S + 1$ values of Ω, the projection of J on the z-axis. Inclusion of both possible signs of Λ generates $2 * (2S + 1)$ primitive basis functions $|nl\Lambda\Omega >$.

All constants for modeling the C_2 molecule were collected from Tanabashi et al. [85]. See Tables 4.3, 4.4, and 4.5 for the constants used in the C_2 simulations. Additional constants came from Brooke et al. [86]. Broadening of the spectral lines was examined by convolving instrumental broadening, temperature broadening, and pressure broadening. Instrumental broadening was found to be the primary broadening mechanism responsible for broadening the molecular spectra. Temperature and pressure broadening contributed little to the broadening due to the mass of the C_2 molecule.

State	**v**	**Origin (eV)**	**B** (s^{-1})	**A**	λ_S	**D**
$a^3\Pi_u$	0	0	1.624045	-15.2691	-0.1549	6.451×10^{-6}
$d^3\Pi_g$	0	19378.46	1.74557	-14.0011	0.03303	6.821×10^{-6}
$d^3\Pi_g$	1	21132.14	1.725401	-13.8744	0.03018	6.965×10^{-6}

Table 4.3 PGOPHER Constants 1: Constants used for modeling C_2 with PGOPHER [85].

State	**v**	**H**	λ_d	A_d	o	p
$a^3\Pi_u$	0	6.74×10^{-12}	–	2.388×10^{-4}	0.67539	2.465×10^{-3}
$d^3\Pi_g$	0	–	–	4.803×10^{-4}	0.61085	3.947×10^{-3}
$d^3\Pi_g$	1	–	–	5.495×10^{-4}	0.61703	4.181×10^{-3}

Table 4.4 PGOPHER Constants 2: Additional constants used for modeling C_2 with PGOPHER [85].

State	**v**	**q**	o_d	p_d	q_d
$a^3\Pi_u$	0	-5.32×10^{-4}	-7.87×10^{-6}	6.3×10^{-8}	-9.5×10^{-9}
$d^3\Pi_g$	0	-7.76×10^{-4}	–	–	–
$d^3\Pi_g$	1	-8.31×10^{-4}	–	–	–

Table 4.5 PGOPHER Constants 3: Constants used for modeling C_2 with PGOPHER [85].

Simulations were run for combinations of vibrational and rotational temperature. The vibrational and rotational temperatures were simulated from 500 K to 5,000 K in 500 K increments. The vibrational temperature of 2,000 K provided the best fit. Additional simulations varied the rotational temperature up to 8,000 K. Figs. 4.12 and 4.13 show the final result of the analysis of the experimental spectra at each center wavelength. Figs. 4.14 and 4.15 show the results of the simulations for a vibrational temperature of 2,000 K, and a rotational temperature of 5,000 K.

T (K)	**$\Delta\lambda_{1/2}$ (nm)**
1000	0.0022
1500	0.0027
2000	0.0031
2500	0.0035
⋮	⋮
5000	0.0049

Table 4.6 Doppler broadening widths for $\lambda \approx 474$ nm.

Broadening mechanisms were examined to determine their effect on the simulated spectrum. Four different broadening mechanisms were examined. Gaussian contributions originated from instrumental broadening and Doppler broadening. Instrumental broadening was calculated by measuring the $\lambda = 514.5$ nm Ar-ion laser line. The FWHM of that line was calculated to be $\lambda_{1/2} = 0.039$ nm. The spectroscopic resolution was determined to be $\lambda/\Delta\lambda \approx 13192$.

Eq. (2.144) was used to calculate the Doppler broadening:

$$\Delta\nu_{1/2} = \sqrt{\frac{8kT\ln 2}{mc^2}}\,\nu_0. \tag{4.12}$$

Table 4.6 shows the computed Doppler $\lambda_{1/2}$ for the band head near 474 nm at five different temperatures. The difference in $\lambda_{1/2}$ over the temperature range is 0.0027 nm. Table 4.6 shows that the Doppler broadening over the range of possible temperatures is an order of magnitude less than the instrumental broadening. Summing the Gaussian line widths in quadrature ($\sqrt{\lambda_{1/2}^2 + \lambda_{1/2}^2}$) yields a total Gaussian line width of $\Delta\lambda_{1/2} =$ 0.039 nm.

The v=0 and v=1 $d^3\Pi_g$ states of C_2 have a lifetime of $\tau \sim 100$ ns [87]. The Lorentzian natural broadening FWHM line width is $\Delta\lambda_{1/2} = 2.38\times10^{-6}$ nm according to Eq 2.139. The Swan band transition is $d^3\Pi_g - a^3\Pi_u$. The state $a^3\Pi_u$ is not the ground state, but it is slightly more energetic than the ground state and is long lived. A transition to the ground state ($X^1\Sigma_g^+$) violates the $g \leftrightarrow u$ symmetry. By comparison, the transition $A^1\Pi_u - X^1\Sigma_g^+$ gives rise to spectral bands known as the Phillips bands. The lifetimes of this transition are on the order of 10-15 μs [88]. The natural line width contributes a very small amount to the overall line width for simple molecules in this type of environment.

Limited cross section data for the collisions between C_2 and N_2 in the literature prevented a direct calculation of the pressure broadening contribution. There is cross section data available for NO. Using NO data and Eq. 2.146, with T = 2,000 K, yields $\Delta\lambda_{1/2} = 1 \times 10^{-4} - 1 \times 10^{-5}$ nm at 100 Torr and $\Delta\lambda_{1/2} = 0.03$ nm for 60 atm [60]. PGOPHER suggests a Lorentzian line width of $\Delta\lambda_{1/2} = 0.03$ nm as is shown in Figs. 4.16 and 4.17. The individual contributions from each broadening mechanism are summarized here.

A. **Instrumental**: $\Delta\lambda_{1/2} = 0.039$ nm.

B. **Doppler**: $\Delta\lambda_{1/2} = 0.0031$ nm.

C. **Pressure**: $\Delta\lambda_{1/2} = 1 \times 10^{-4} - 1 \times 10^{-5}$ nm at 100 Torr; $\Delta\lambda_{1/2} = 0.03$ nm for 60 atm.

D. **Natural Line Width**: $\Delta\lambda_{1/2} = 4.66 \times 10^{-6}$ nm.

A comparison of the FWHM for the experimental data and the simulations, at a center wavelength of 470 nm, is shown in Fig. 4.18.

An additional possible source of apparent broadening in the absorption spectrum near the band heads might be attributable to a loss of dynamic signal range. This loss may have occurred where the strong band heads absorbed a large percentage of available photons. The number of C_2 molecules would have been greater than the number of photons. This would have led to an artificially shortened absorption peak and a broader FWHM. The relative amplitude of the band head to other J-states would have also been reduced.

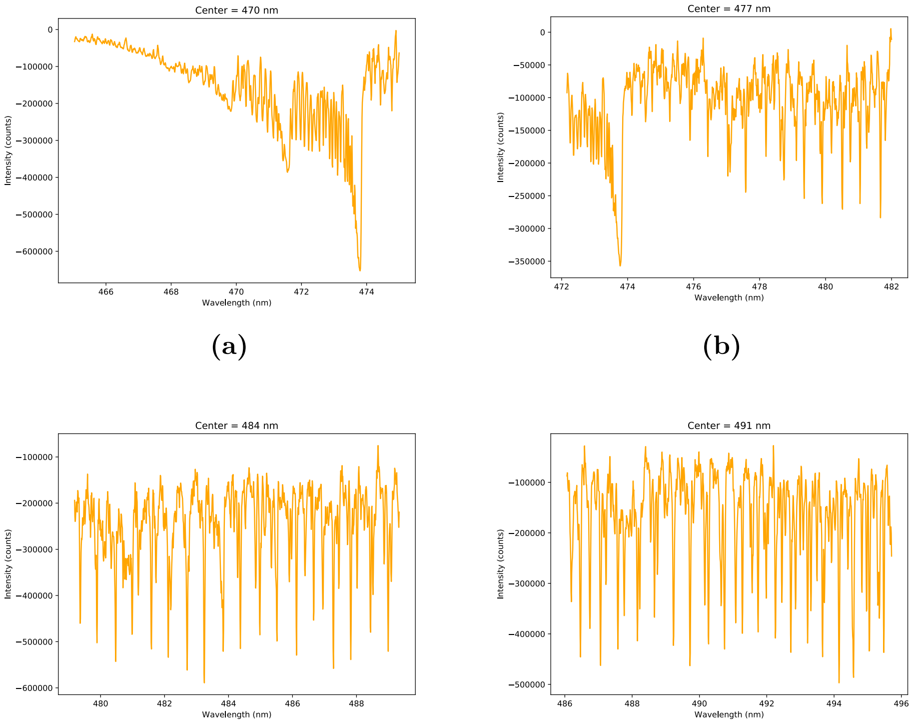

(a) **(b)**

(c) **(d)**

Figure 4.12 Plots of the absorption observed at the first four center wavelength positions.

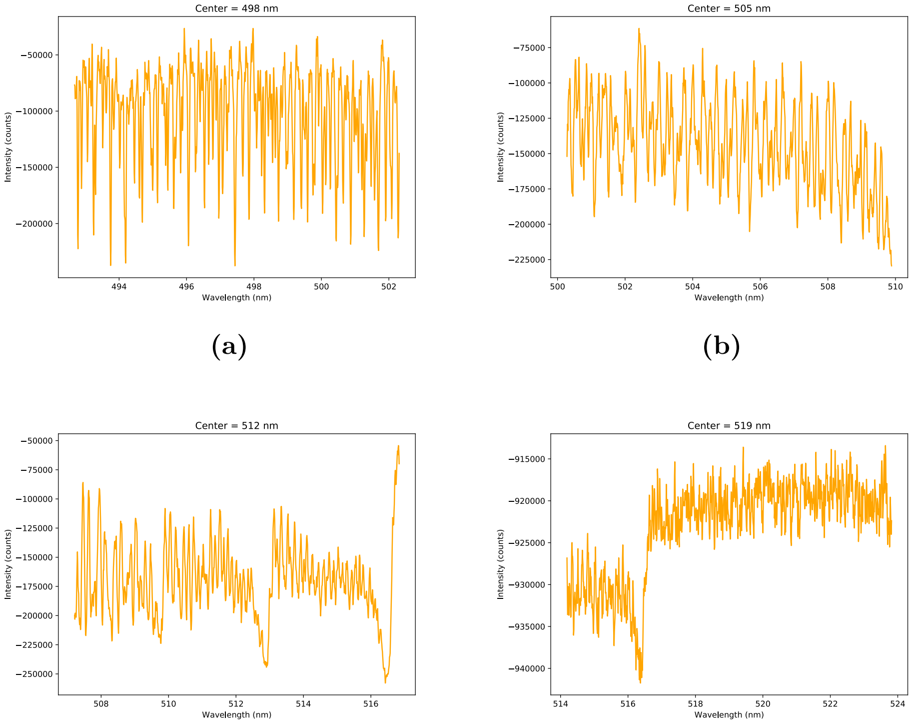

(a) **(b)**

(c) **(d)**

Figure 4.13 Plots of the absorption observed at the remaining four center wavelength positions.

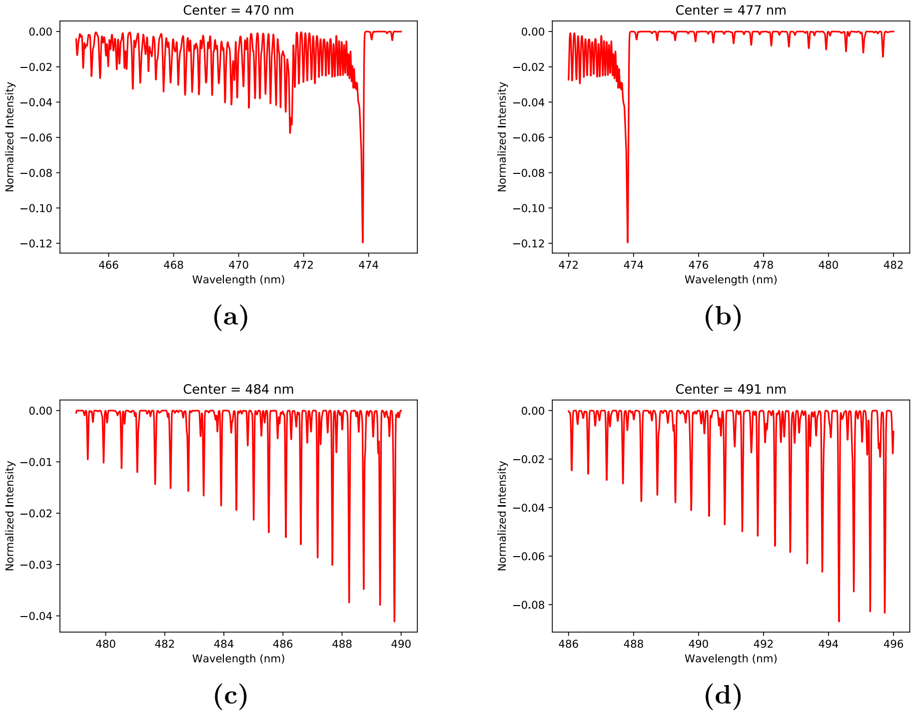

(a) **(b)** **(c)** **(d)**

Figure 4.14 Plots of the simulated data for $T_v = 2000$ K and $T_r = 5000$ K at the first four center wavelength positions with only Gaussian line width components.

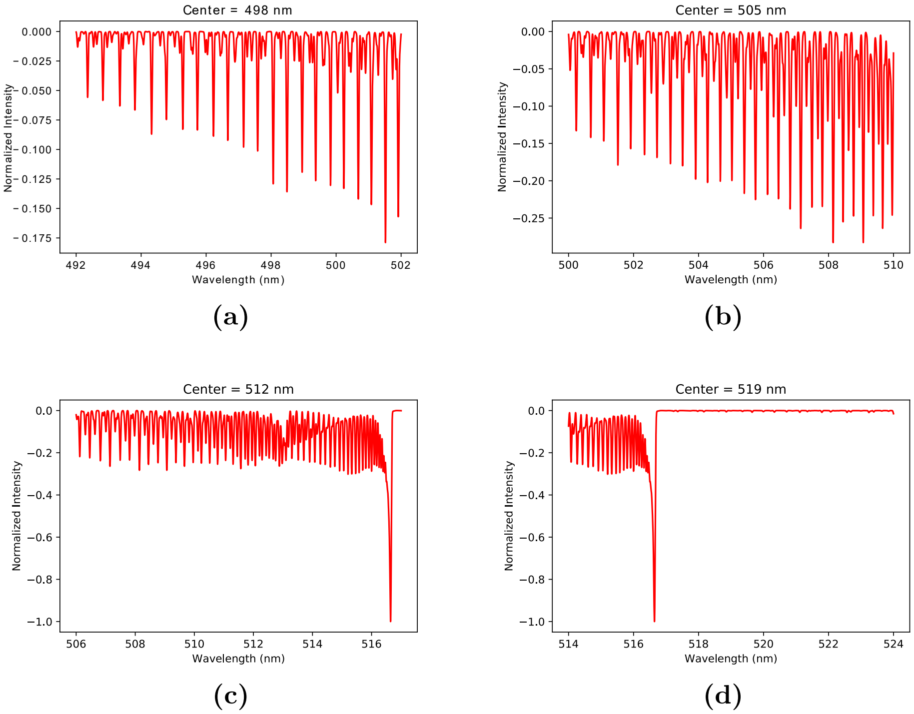

(a) **(b)** **(c)** **(d)**

Figure 4.15 Plots of the simulated data for $T_v = 2000$ K and $T_r = 5000$ K at the remaining four center wavelength positions with only Gaussian line width components.

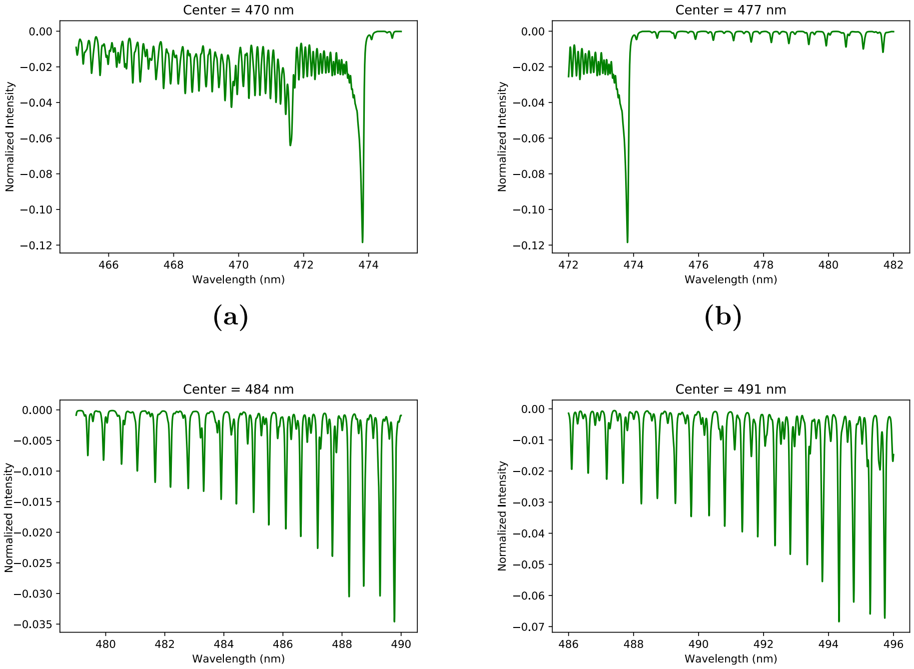

(a) **(b)**

(c) **(d)**

Figure 4.16 Plots of the simulated data for $T_v = 2000$ K and $T_r = 5000$ K at the first four center wavelength positions with Gaussian and hypothetical Lorentzian components.

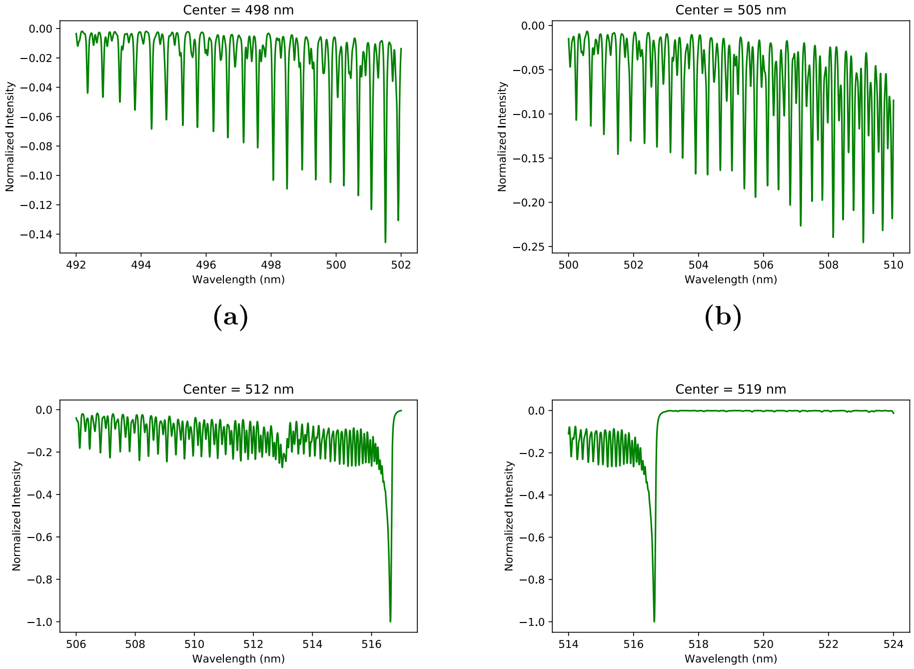

(a) **(b)**

(c) **(d)**

Figure 4.17 Plots of the simulated data for $T_v = 2000$ K and $T_r = 5000$ K at the remaining four center wavelength positions with Gaussian and hypothetical Lorentzian components.

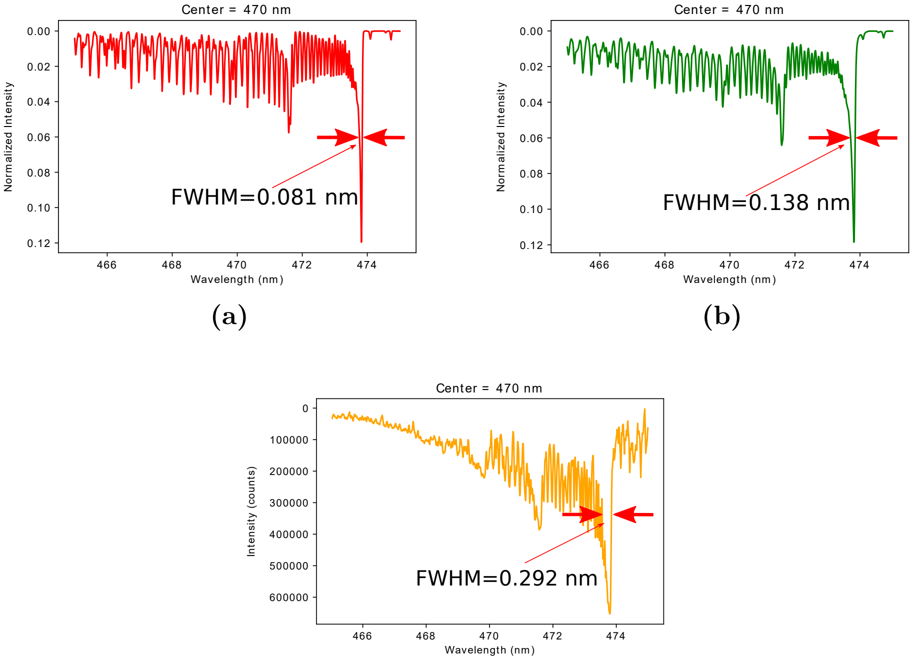

(a) **(b)**

(c)

Figure 4.18 These plots compare the FWHM of the data at a center wavelength of 470 nm with the simulations. (a) PGOPHER simulation with only Gaussian $\Delta\lambda_{1/2} = 0.039$ nm, (b) PGOPHER simulation with Gaussian $\Delta\lambda_{1/2} = 0.039$ nm and Lorentzian $\Delta\lambda_{1/2} = 0.030$ nm, and (c) Data.

This experiment demonstrated the use of a supercontinuum laser for absorption spectroscopy of laser ablation plumes. The quasi-CW nature of the SuperK EXTREME laser worked best when observing molecular carbon. A pulsed SC laser would provide faster time gating and better data quality. A pulsed system would also make the study of atomic species accessible. Simulations with PGOPHER extracted approximate temperatures for the C_2 molecules in the plume: $T_v = 2000$ K and $T_r = 5000$ K. Noise in the data makes an exact fit difficult to obtain. The different temperature for the rotational and vibrational degrees of freedom indicated that the gas was not in thermal equilibrium. Despite these challenges, this experiment successfully captured analyzable high-resolution absorption data for C_2 and demonstrated a promising new technique for probing laser ablation plumes.

Chapter 5

Titanium Monoxide

5.1 Introduction

Titanium monoxide (TiO) is an important molecule in astrophysics. TiO has been studied in astrophysics for many years and is typically seen in brown dwarfs and late stage stars such as red giants and yellow hypergiants. Hypergiants are a special type of Luminosity Class Ia supergiants. Hypergiants often have broader absorption lines than other Ia stars, have Hα emission, and have one or more broadened emission lines due to an extended atmosphere or large mass loss [89]. Hypergiants have significant dust envelopes. Enhanced mass ejection has been observed in hypergiants including the yellow hypergiant star ρ Cassiopeiae (ρ Cas). Yellow hypergiants are cool luminous stars and are post-red supergiants evolving to the blue hypergiant phase [90,91]. Mass loss rates exceed 10^{-5} $\mathrm{M}_{\odot}\mathrm{yr}^{-1}$ [91].

It has been observed that ρ Cas has had large mass ejections on several occasions over the last century. Lobel et al. observed V brightness dim by approximately a full magnitude between June and September in 2000, with an effective temperature decrease of 3,000 K [92]. TiO absorption was observed during the summer months of 2000, and TiO formation occurred before the greatest dimming took place. Supersonic driving of the TiO shell with a mass loss rate of $M \approx 5.4 \times 10^{-2}$ $M_\odot$ yr^{-1} has been modeled by Lobel et al. as being driven by the release of hydrogen recombination energy [92]. An optically thick circumstellar gas shell at a low temperature with a mass of 3×10^{-2} $M_\odot$ was created by the dynamic instability of the upper atmosphere as the star pulsated [92]. The brightness of ρ Cas recovered by April 2001. The minimum gas density in the TiO formation region is believed to be on the order of $\rho_{min} = 10^{-10}$ g cm^{-3} based on the observed spectra [92]. Mean TiO envelope expansion velocity was -35 km s^{-1}, and the distance that the envelope traveled over 200 days was $d_s = 869$ $R_\odot$ (6.046×10^{13} cm) [92]. Other large mass loss events were observed for ρ Cas in 1945-1947 and 1985-1986.

5.2 Experiment

An experiment was designed to explore the formation of the TiO molecule due to the expansion of a Ti ablation plume in a rarefied O_2 environment. This experiment investigated whether the shock wave produced by the laser ablation of Ti into an O_2 background gas contributed to the formation of TiO molecules. Specifically, the experiment involved the ablation of a Ti target into a 100 Torr O_2 background. Shots ablating Ti into N_2 gas background were used as control sets. Fast ICCD imaging, optical spectroscopy, and shadowgraphy were used to observe the plume.

Harilal et al. discussed an experiment which explored the role of shock waves in the formation of AlO when an Al target was ablated into air at 1 atm [93]. Their conclusion was that most AlO formation occurred after the shock wave collapsed and air rolled up near the surface into the back of the plume. Mixing between Al and O_2 in the air then occurred. Harilal et al. observed the coexistence of atomic Al and AlO in the plume with optical spectroscopy. Plume hydrodynamics and plasma chemistry both played a role in the formation of AlO [93].

The TiO experiment was conducted with the Powerlite laser at 1,064 nm. Laser energy was reduced from 3.0 J to 0.5 J using the beam energy reducer described in Chapter 3. Ti produced by Goodfellow with a purity of 99.9% was used as the target. Welding grade oxygen, with $> 99.5\%$ (industry standard) purity, was used as the back-fill gas for the oxygen shots. N_2 was used for the control shots.

Experiments began with an Andor iStar ICCD for fast imaging of the plumes at different delay times after laser irradiation. Data was collected with a Thorlabs FB700-40 40±8 nm FWHM bandpass filter centered at 700±8 nm that was positioned in from of the camera. A Newport Optics FSQ-OD200 neutral density filter with OD=2.0 was positioned between the band-pass filter and the telescope. The band-pass filter centered at 700 nm was chosen to coincide with TiO molecular emission in a spectral region where atomic Ti or O_2 emission was not present. The 40 nm spectral window included emission from the TiO $A^3\Phi$-$X^3\Delta$ state with $\Delta v = 0$ and $\Delta v = 1$ (γ bands). Data was also collected with only the neutral density filter to observe the overall visible light emission from the plume. The gate width for each image was set at 1 μs. Camera gain was set at 100. Each shot sequence consisted of 10 separate shots at 1 target position. Minimal target deformation was observed after 10 shots indicating little impact on plume characteristics.

Evaluation of the imaging data determined that the greatest TiO emission occurred at t=5 μs and t=9 μs after target irradiation. The intensity of the light diminished at time delays larger than 1 μs. The next stage of the experiment consisted of measuring spectra. Spectroscopic measurements confirmed the observed emission species and provided a way to measure the plume temperature. The Acton/PI-MAX system was used to collect the data. The 150 l/mm grating was used to collect low resolution data suitable for line identification and temperature calculations using the Boltzmann plot method. The gate width was set to 1 μs, and 5 μs and 9 μs delays were used. The grating was centered at 700 nm. Each shot sequence in this phase was comprised of 30 shots. Each spot on the target received 10 shots before being moved to a new surface. These 30 shots were integrated into a single image by the Acton WINSPEC software to improve the signal-to-noise ratio. Individual laser shots had a poor signal-to-noise ratio ($\sim$ 1:1-2:1).

The final phase of the experiment involved capturing shadowgraphy data to determine the shock wave position. Data was collected at 5 μs and 9 μs. Ten separate shots at each time step were collected. All shadowgraphy was collected with a 532 nm probe beam.

The validity of scaling between laboratory size experiments and astrophysical objects is always an important consideration. It is often useful to find dimensionless quantities to scale between laboratory experiments and astrophysical observations. Column density is a quantity that was used to quantify the scale of this experiment. Distances were measured on the cm scale, and densities were on the order of 10^{-3} g cm^{-3} in this experiment yielding a column density on the order of 10^{-3} g cm^{-2}. A minimum column density of approximately 6×10^{3} g cm^{-2} was calculated for ρ Cas based on the observations and calculations made by Lobel et al. from the 2000-2001 mass outburst. The astronomically observed TiO spectrum was produced from the absorption of light from ρ Cas which is a continuous and extended source. The experimentally measured TiO spectrum was generated by self-emission from an excited and short-lived plume. The scaling difference between laboratory and astronomical sources is extreme, but this does not preclude phenomenological tests for molecular formation mechanisms.

Laser Wavelength	1064 nm
Laser Energy	500 mJ
Laser Spot Diameter	1.00 mm
Laser Intensity	7.07×10^9 W/cm^2

Table 5.1 Laser parameters for the TiO experiment.

5.3 Imaging Analysis

The analysis of the images collected with the 700 nm filter in place involved observing at what location and time the strongest TiO features appeared. Fig. 5.1 shows plume images collected at t=5 μs with the filter in place. A new quantity has been introduced to make the analysis of these images more quantitative. The center of emission (CoE) is found by summing the pixels along the vertical axis and taking the center of mass of the intensity of the light. This process is summarized in Eq. (5.1) where I_c is the center of intensity, I_j is the number of counts at pixel j, and x_j is the position of the pixel:

$$I_c = \frac{\sum_j I_j x_j}{\sum_j I_j}. \tag{5.1}$$

The CoE shows the region along the expansion axis where the greatest emission of light in the λ = 680-720 nm region of the optical spectrum was observed. This part of the spectrum corresponds to TiO emission. The mean position of the CoE in the O_2 background is pixel 271 ± 9 (3.26 ± 0.12 mm). A mean position at pixel 262 ± 2 (3.15 ± 0.03 mm) was found for the N_2 atmosphere. The greater standard deviation in the mean position of the CoE for the O_2 atmosphere can be understood by looking at a couple of different plumes, each observed with a 5 μs delay. Fig 5.1 shows plume emission at 5 μs after laser irradiation. The locations in the plume where TiO emission occurred varied greatly during the experiments.

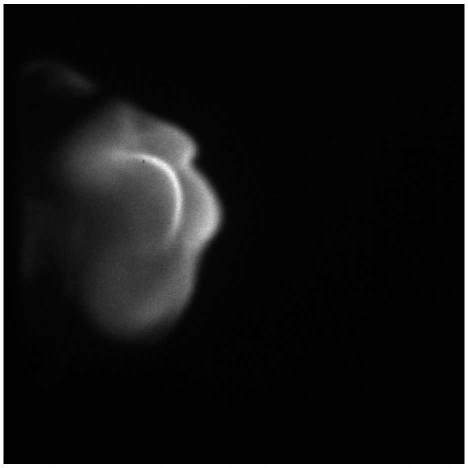

(a)

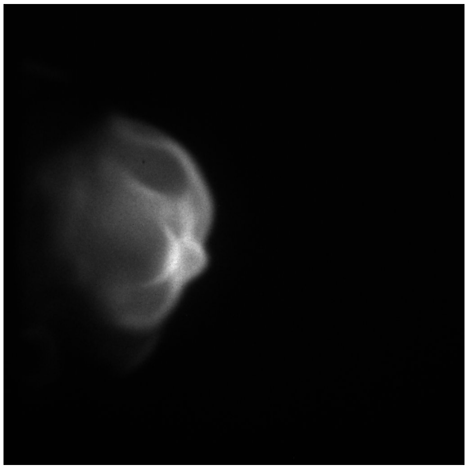

(b)

Figure 5.1 TiO emission in 2 separate plumes in an O_2 atmosphere at $t = 5\ \mu s$.

Fig. 5.2 shows the result of vertically binning the image data. Note the significantly lower number of counts for the O_2 background as compared to the N_2 background. Table 5.2 shows the CoE for 10 separate shots taken at 1 target position in an O_2 background. Table 5.3 provides the CoE for 7 shots taken at 1 target position in an N_2 background. The difference between the CoE for the N_2 background and the O_2 background was small, but the CoE is calculated over the full height of the image (1,024 pixels/∼6 mm). Fig. 5.2 shows that the plumes expanding into the N_2

background have a more uniform emission than the plumes in the O_2 background. A sharper emission peak is observed for the plumes expanding into O_2 which may indicate that the proper thermodynamic conditions for TiO formation are present. The sharper emission peak was a general observation since shot-to-shot variability can be large due to turbulent mixing.

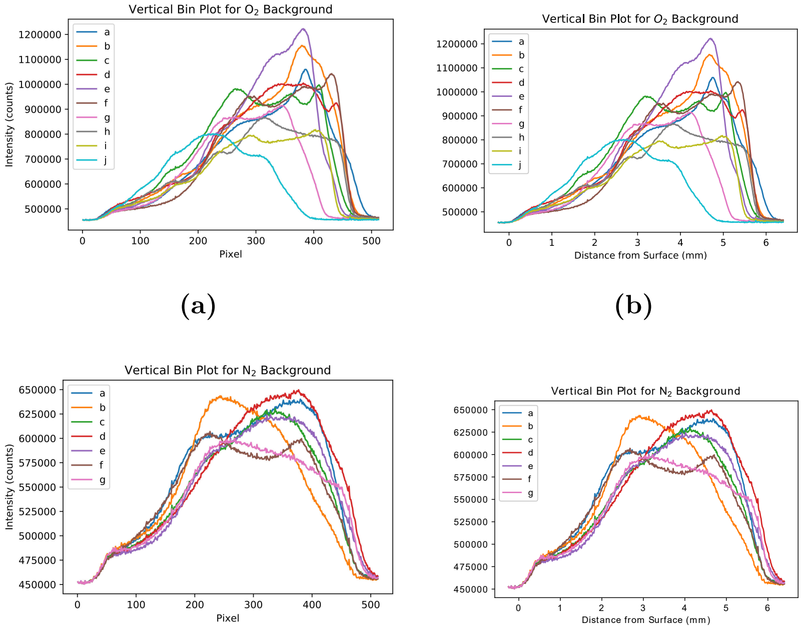

(a) **(b)**

(c) **(d)**

Figure 5.2 Vertical bin plot of the ICCD images: (a),(c) show the pixel position, and (b),(d) show the physical distance from the target surface.

ICCD imaging was performed at 5, 7, 9, 11, 13, 15, 17, and 19 μs after laser irradiation. Significant TiO emission was not observed at delays of less than 5 μs due to strong atomic Ti emission in the same wavelength region from Ti I transitions including the $b^3F_4 - y^3D_3^0$ transition [94]. Spectroscopic observations were targeted at 5 and 9 μs based on the strong TiO emission at these times. Figs. 5.3, 5.4, 5.5, 5.6, and 5.7 provide a sample of the images for different delay times.

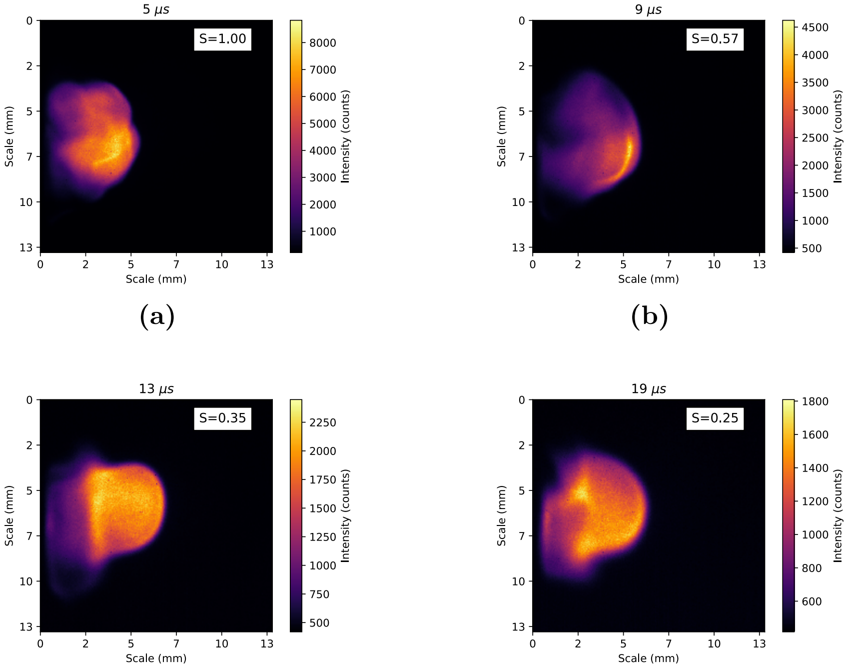

(a) **(b)**

(c) **(d)**

Figure 5.3 Sequence of ICCD images with no band-pass filter. The intensity scale factor is shown in the box in the upper right corner and corresponds to: $I = S * I_{5\mu s}$.

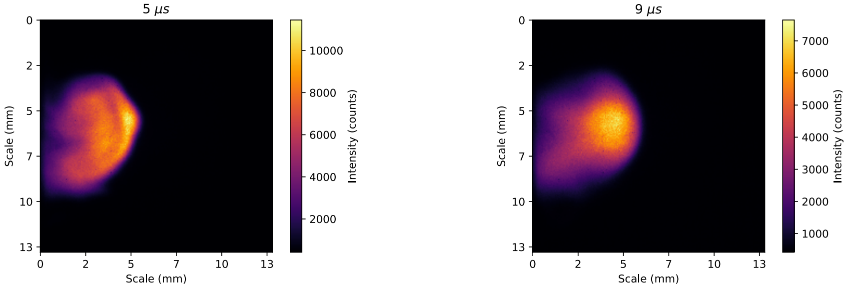

(a) **(b)**

Figure 5.4 N_2 with no filter.

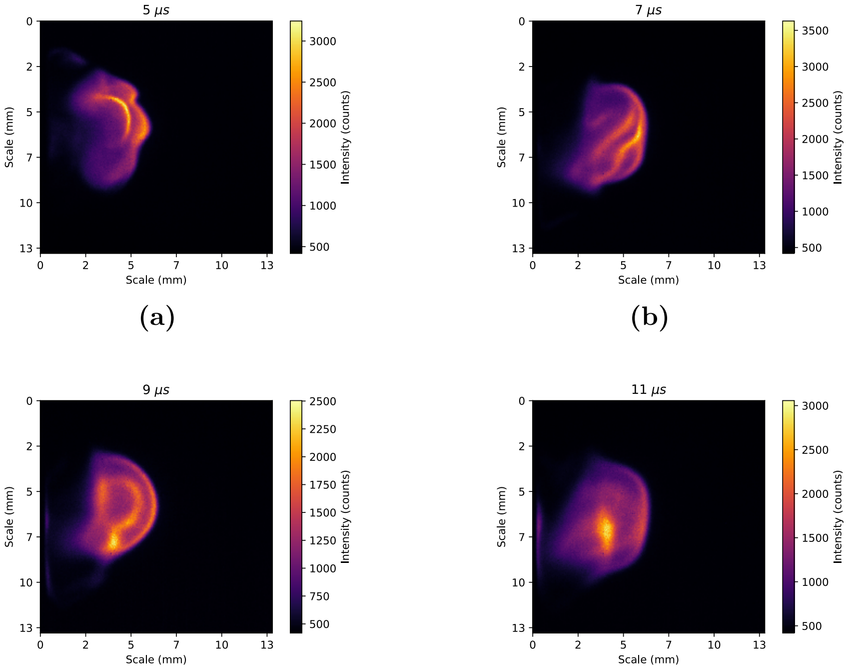

(a) **(b)**

(c) **(d)**

Figure 5.5 ICCD fast imaging of the plume in O_2. Delays: (a) 5 μs, (b) 7 μs, (c) 9 μs, and (d) 11 μs.

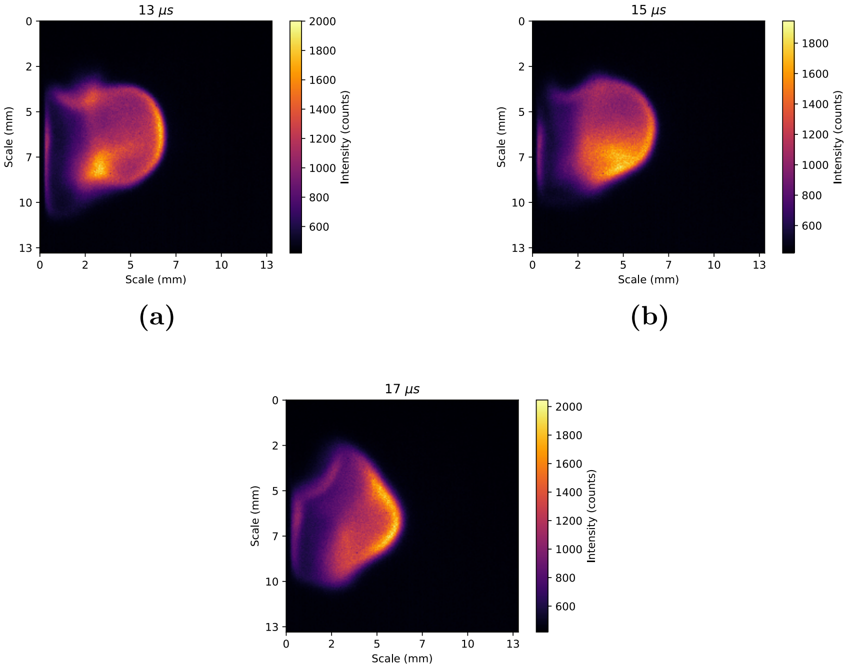

(a)

(b)

(c)

Figure 5.6 ICCD fast imaging of the plume in O_2. Delays: (a) 13 μs, (b) 15 μs, and (c) 17 μs.

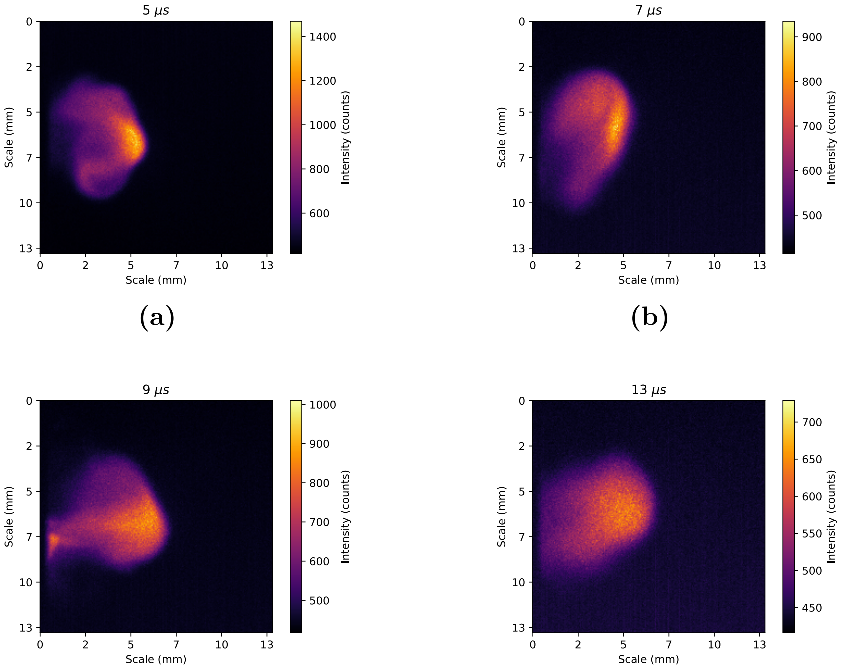

(a) **(b)** **(c)** **(d)**

Figure 5.7 ICCD fast imaging of the plume in N_2. Delays: (a) 5 μs, (b) 7 μs, (c) 9 μs, and (d) 13 μs.

Shot	**Pixel Position**	**Distance from Surface (mm)**
a	278	3.35
b	280	3.38
c	270	3.25
d	277	3.34
e	275	3.32
f	281	3.39
g	262	3.15
h	270	3.25
i	266	3.20
j	249	2.98
Mean	**271**	**3.26**
Standard Deviation	**9**	**0.12**

Table 5.2 O_2 CoE image data.

Shot	**Pixel Position of CoE**	**Distance from Surface (mm)**
a	263	3.16
b	259	3.11
c	262	3.15
d	266	3.20
e	264	3.17
f	260	3.12
g	262	3.15
Mean	**262**	**3.15**
Standard Deviation	**2.17**	**0.03**

Table 5.3 N_2 CoE image data.

Shadowgraphy was employed to determine the position of the shock wave at the t=5 μs and t=9 μs delay times. Fig. 5.8 shows an example of a shock imaged at 5 μs. Fig. 5.9 shows 4 additional shocks at t=5 μs. The position of the shock wave is remarkably stable. Any shot-to-shot variation is difficult to observe. The distance of the radius from the target to the center of the shock front region is approximately 8.2 mm.

Shadowgraphy at t=9 μs shows a very stable shock wave with a radius of 11 mm. Fig. 5.10 shows a shock wave at t=9 μs. The distance traveled by the shock wave

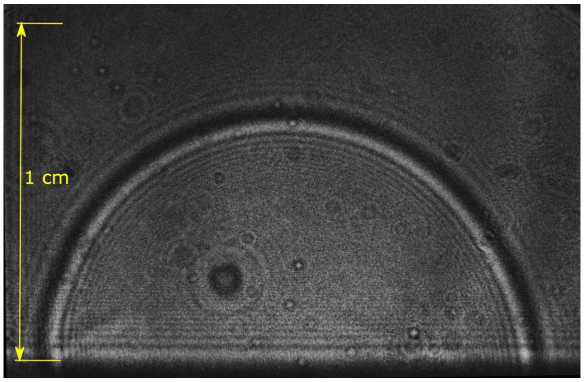

Figure 5.8 Shock wave at t=5 μs.

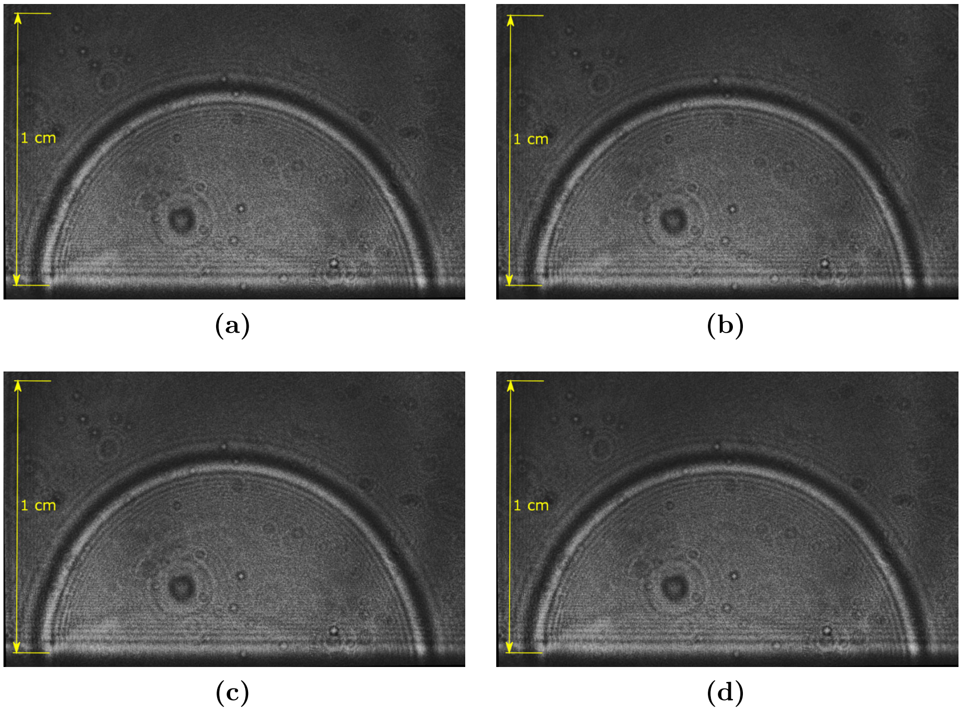

(a) (b) (c) (d)

Figure 5.9 Additional shadowgrams of the shock wave from separate laser ablation shots captured at 5 μs.

between t=5 μs and t=9 μs was 2.8 mm, giving an average shock velocity of 700 m/s between t=5 μs and t=9 μs.

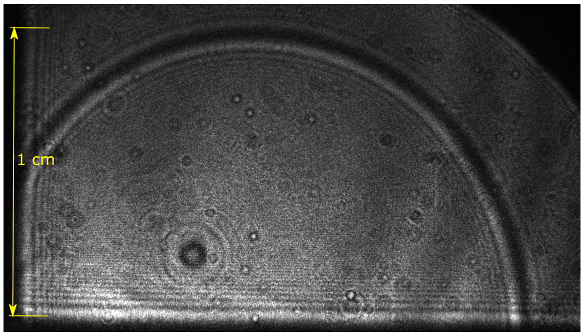

Figure 5.10 Shadowgraphy showing the shock wave at 9 μs. The left side of the shock in this view is colliding with the top of the target holder.

5.4 Spectroscopy

Low resolution spectroscopy collected with the Acton/PI-MAX system yielded 6 data sets. Table 5.4 provides a breakdown of the shots.

Shot Sequence	**Atmosphere (Torr)**	**Delay (μs)**
1	O_2=103.8	5
2	O_2=103.8	9
3	O_2=100.2	5
4	O_2=100.2	9
5	N_2=100.9	5
6	N_2=100.9	9

Table 5.4 Description of the spectroscopic shot sequences.

One challenge in attempting to make quantitative measurements with the TiO spectrum is the mixing of atomic and molecular spectra in a spectrum as active as Ti and TiO. Poor signal-to-noise ratio data made the use of the TiO spectrum found near 700 nm difficult to analyze. Emission from strong atomic lines was instead used to calculate the temperature of the plume material. An assumption of thermodynamic equilibrium between the atomic states of Ti and the molecular states of TiO was made so that the temperature of the TiO could be calculated using Ti atomic emission.

The plume was imaged onto the entrance slit of the spectrometer so that the plume expanded downward along the slit. Fig. 5.11 shows a sample data set. The vertical axis provided spatial resolution along the expansion direction. The horizontal axis is the dispersion axis and provides wavelength resolution. Data was extracted from 3 separate locations along the plume expansion direction. Fig. 5.11 shows the three locations with distances from the target surface of 0.86 mm, 2.90 mm, and 4.08 mm. A 10-pixel vertical bin was completed at each location to generate the plots of the collected spectrum. Figs. 5.13 and 5.14 show the plots of the spectra for the O_2 and N_2 shot sequences, respectively. These data sets are calibrated for wavelength but have

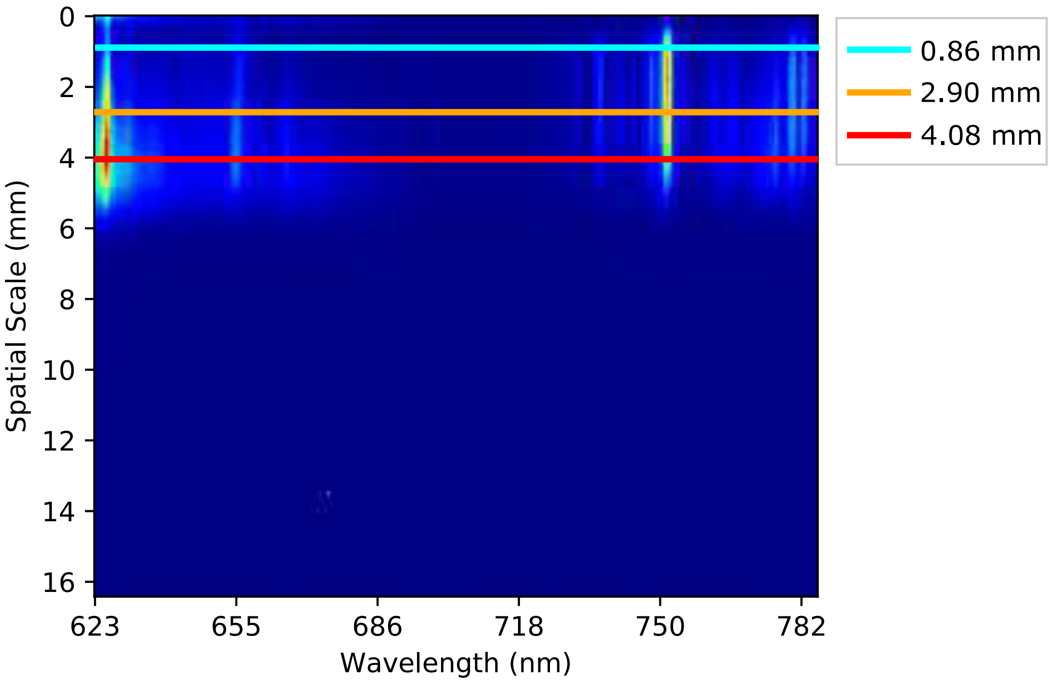

Figure 5.11 Low resolution spectroscopic data captured with the Acton/PI-MAX system. The three lines show where data was extracted at different distances from the target surface.

not been corrected for instrumental efficiency. Wavelength calibration was obtained using a Ne Newport/Oriel pencil calibration lamp (Lamp 6032). The calibration fit is shown in Fig. 5.12.

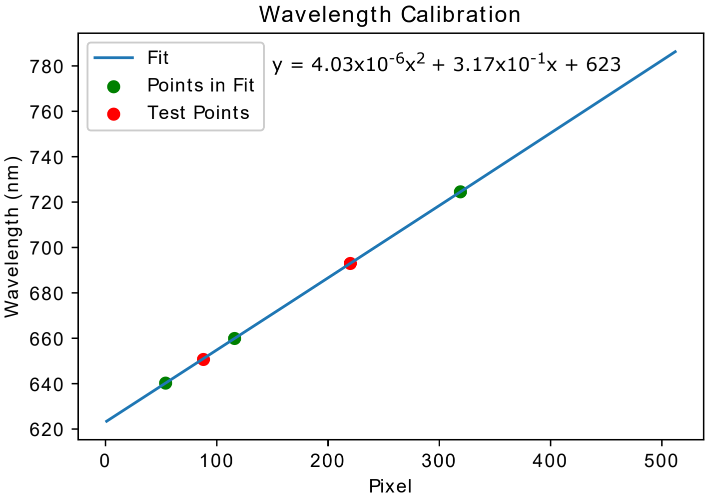

Figure 5.12 This diagram shows the points used in the fit to calibrate the spectroscopic wavelength.

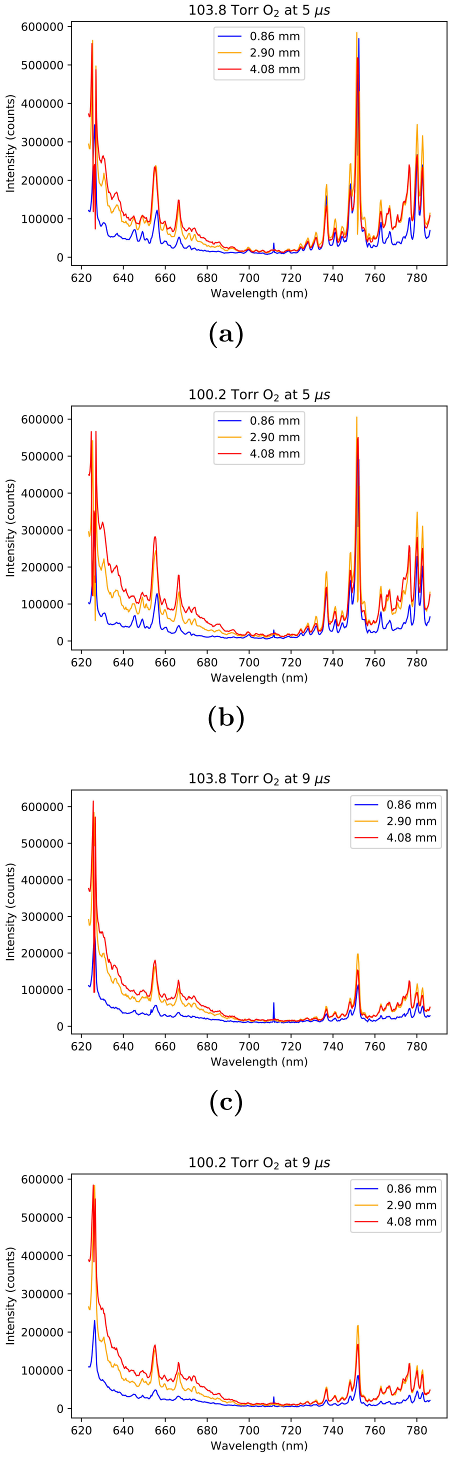

(a)

(b)

(c)

(d)

Figure 5.13 Low-resolution spectroscopy of a Ti plume expanding into O_2. Delay: (a)-(b) 5 μs and (c)-(d) 9 μs.

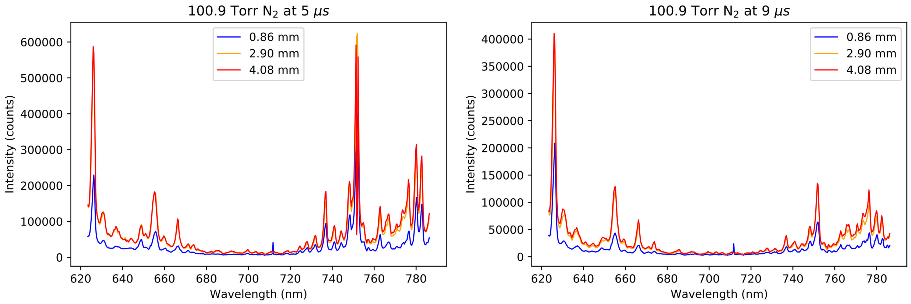

(a) **(b)**

Figure 5.14 Low-resolution spectroscopy of a Ti plume expanding into N_2. Delay: (a) 5 μs and (b) 9 μs.

The process outlined in Section 3.6.1 describes how the QTH lamp was used to obtain a proper correction of the spectroscopic data. Fig. 5.16 (a) shows the uncorrected spectrum. Fig. 5.16 (b) shows the corrected spectrum. The upper wavelength of the corrected spectra is cut off slightly above 740 nm because the correction polynomial, C_λ in Eqs. (3.9) and (3.10), was not valid for wavelengths above 740 nm. The sensitivity of the spectrometer dropped to nearly zero above 740 nm and forced the correction factor to oscillate between small positive and negative values. The spectra in Figs. 5.13 and 5.14 were divided by the QTH polynomial correction factor to give the spectra in Figs. 5.17 and 5.18.

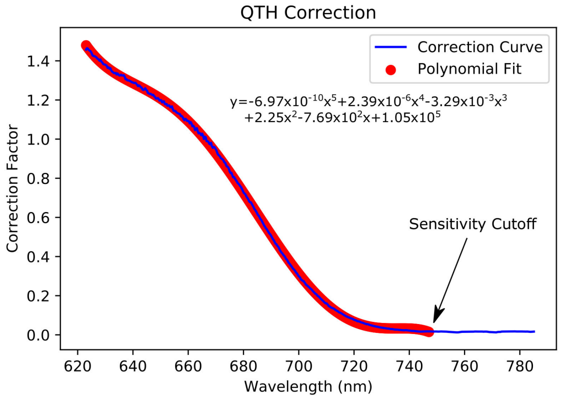

Figure 5.15 QTH correction polynomial.

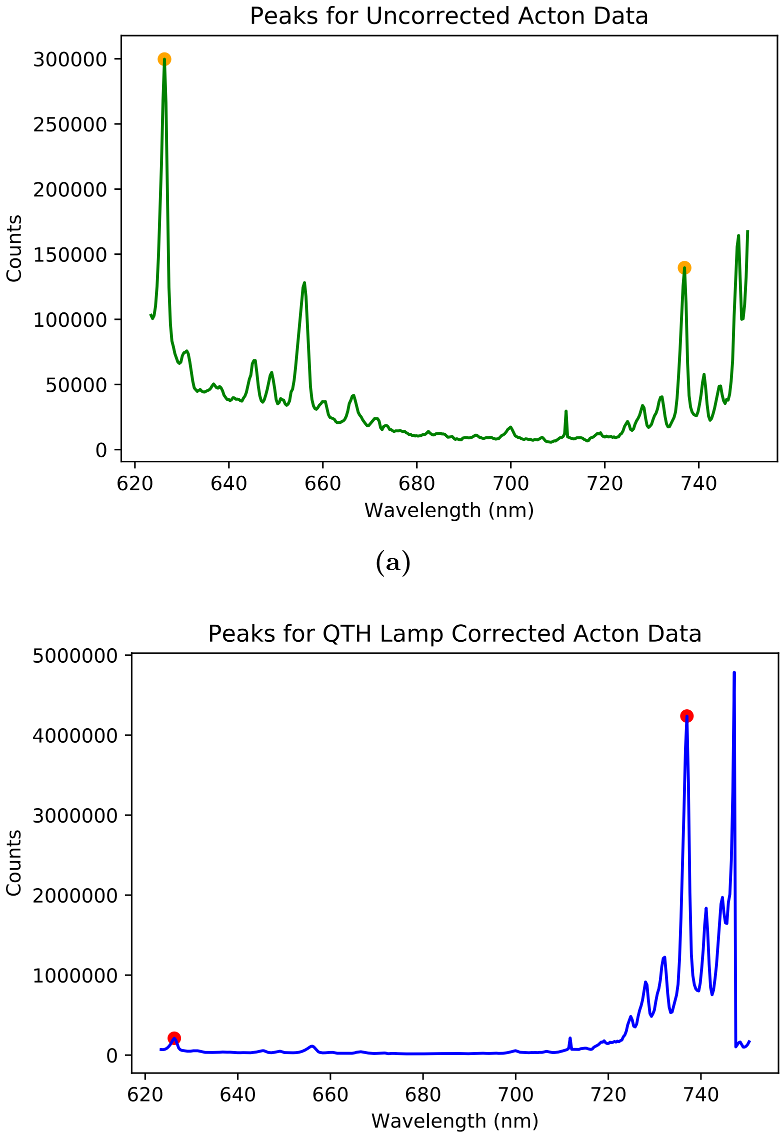

(a)

(b)

Figure 5.16 Instrumental correction of low-resolution spectroscopy of a Ti plume expanding into N_2: (a) uncorrected and (b) corrected. The red and orange circles highlight the lines of interest.

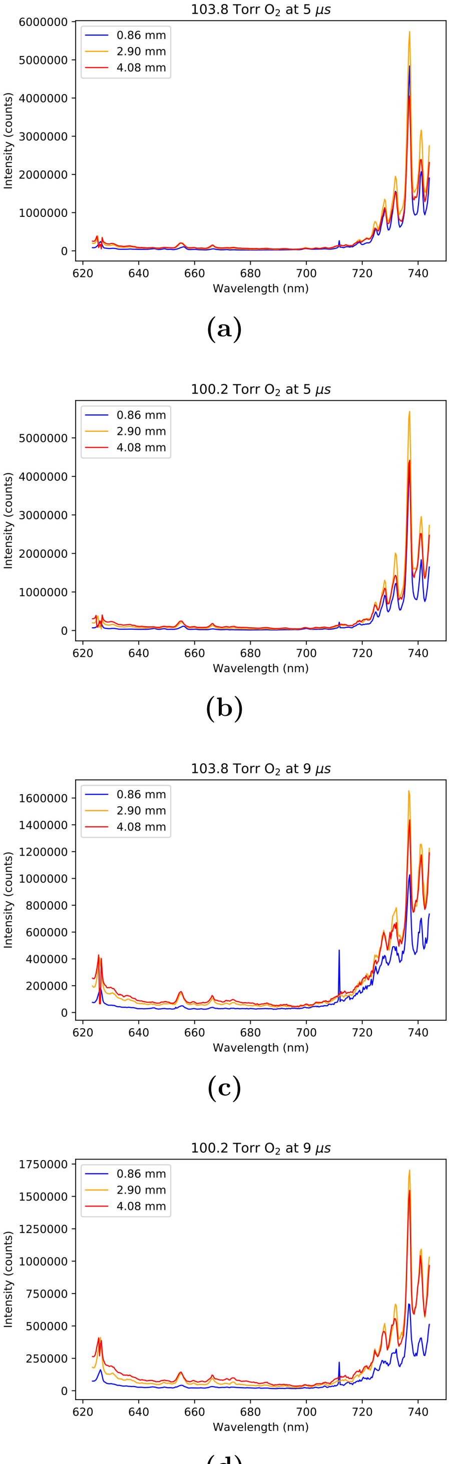

(a)

(b)

(c)

(d)

Figure 5.17 Instrumental correction of low-resolution spectroscopy of Ti plume expanding into O_2. Delay: (a)-(b) 5 μs and (c)-(d) 9 μs.

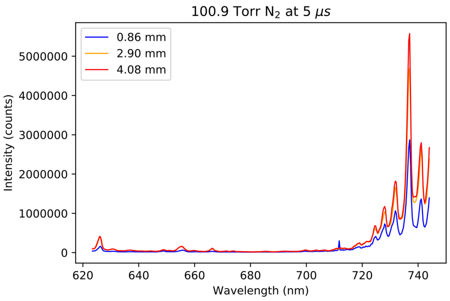

(a)

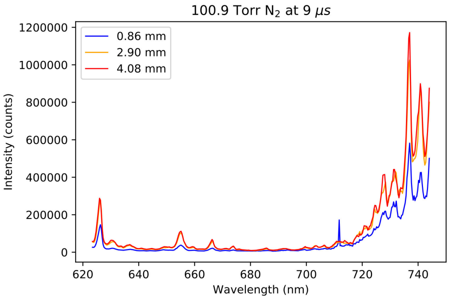

(b)

Figure 5.18 Instrumental correction of low-resolution spectroscopy of Ti plume expanding into N_2. Delay: (a) 5 μs and (b) 9 μs.

Comparing the physical location of the spectral and shock features from the ICCD imaging, shadowgraphy, and spectroscopy produced a map of the area where TiO emission is greatest. Fig. 5.19 shows a map produced for t=5 μs. The general emission region exists from 3.0 mm to 7.7 mm. The shock wave was consistently located at 8.0 mm. The compiled data showed that TiO emission always lags behind the shock front.

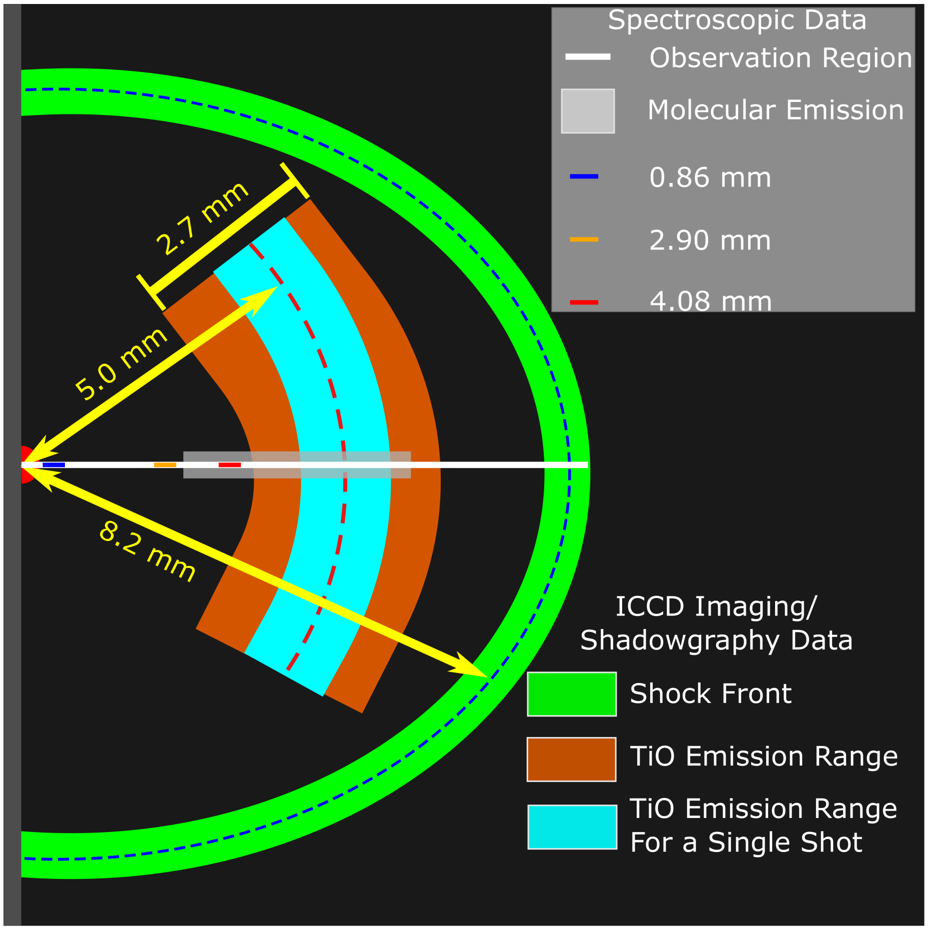

Figure 5.19 This diagram shows a schematic of the relative position of the shock wave to the region where TiO emission is observed with ICCD imaging and spectroscopy.

Spectroscopic analysis of the plumes was conducted to measure the temperature and density of the plume. Low-resolution data was used to calculate the temperature of the neutral atomic Ti. Direct molecular temperature measurements were difficult to make due to the difficulty in obtaining clear high-resolution spectra of the strong TiO bands amid the atomic Ti spectrum. The TiO bands located in the atomically quiet region near 700 nm were too weak to get strong statistics from.

The Boltzmann plot method, described in Section 2.5.1, was used to calculate the temperature of Ti I. Plotting Eq. 2.106 as a function of E_j gives the slope. The intensity of two separate triplets was measured near 625 nm and 734 nm. A modification to the process outlined in Section 2.5.1 was needed since both lines are unresolved triplet states. Eqs. (2.105) and (2.106) assume a single well-defined line. Low-resolution spectroscopy on singlet states provides the best results for the Boltzmann plot method. The triplet could be fully resolved with high resolution spectroscopy, but the line intensities taken from states with a large energy separation provide a better temperature. Eqs. (2.105) and (2.106) can be rewritten as:

$$I_k \lambda_k = g_k A_k C exp(-E_{k_j}/T), \tag{5.2}$$

for each component state of the triplet, k. A single intensity from the unresolved triplet, I, must be used. The energy difference between the three states in a single triplet is small. The energy, E_j, and wavelength, λ, for the center state of each triplet was used. The product of the statistical weights, g_k, and the Einstein spontaneous emission coefficients, A_k, are summed to give the final equation:

$$(I_1 + I_2 + I_3)\lambda = (g_1 A_1 + g_2 A_2 + g_3 A_3) * C * exp\left(\frac{-E}{T}\right), \tag{5.3}$$

giving,

$$I\lambda = (\sum_{k=1}^{3} g_k A_k) C exp(-E/T), \tag{5.4}$$

which becomes,

$$(I\lambda)/(\sum_{k=1}^{3} g_k A_k) = C exp(-E/T). \tag{5.5}$$

Shot Seq.	**Wavelength (nm)**	E_k **(eV)**	A_k (s^{-1})	g_f
Triplet 1:				
	625.8099	3.42	8.36×10^6	9
	625.8705	3.44	8.90×10^6	11
	626.1096	3.41	8.07×10^6	7
Triplet 2:				
	734.46952	3.15	1.40×10^6	9
	735.7726	3.13	1.33×10^6	7
	736.4099	3.11	1.60×10^6	5

Table 5.5 Constants used in the Boltzmann plot calculations for Ti I [95].

All constants used in the Boltzmann plot calculation are listed in Table 5.5. The temperature calculation was made at each of the 3 distances shown in Fig. 5.11. The results of the calculation are shown in Table 5.6.

Shot Seq.	**Atmosphere (Torr)**	**Delay (μs)**	**0.86 mm**	**2.90 mm**	**4.08 mm**
1	O_2=103.8	5	699 K	743 K	797 K
2	O_2=103.8	9	923 K	1009 K	1065 K
3	O_2=100.2	5	698 K	739 K	789 K
4	O_2=100.2	9	1003 K	1002 K	1028 K
5	N_2=100.9	5	715 K	780 K	755 K
6	N_2=100.9	9	1014 K	1037 K	1007 K

Table 5.6 Temperatures calculated with the Boltzmann plot method.

5.5 Spectroscopic Modeling

Spectroscopic modeling was completed to compare with the spectroscopic data collected in the experiment. PrismSPECT was used to model the Ti atomic spectra. PGOPHER was used to study the TiO diatomic spectrum [83,84]. The regime studied for the formation of TiO consisted of neutral Ti and TiO. PrismSPECT was used to model the atomic Ti spectrum. PrismSPECT is a proprietary collisional-radiative atomic spectroscopy modeling program produced by Prism Computational Sciences, Inc. [96]. PrismSPECT is used primarily to model the spectra of atoms/ions found in plasmas. PrismSPECT uses built-in atomic data tables to calculate spectroscopic energy states for the atoms and ions of interest. PrismSPECT includes line shape analysis for Stark broadening and Doppler broadening. Input parameters include ion species, ion temperature, electron density, gas pressure, and plasma geometry. Conditions ranging from neutral species to fully ionized plasma can be modeled. Local thermodynamic equilibrium may be chosen. Time dependent rate equations may also be used.

Low temperature spectroscopy was chosen for modeling the Ti lines since the plume was known to be a hot gas at t=5 μs. LTE was chosen for the thermodynamic equilibrium condition. The geometry of the plume was chosen to be spherical with a radius of 1 cm. Temperature and pressure were allowed to vary in a parameter search. The spectroscopic resolution of the lines was also incorporated into the simulation. A comparison of the ratio of the line intensity of the unresolved Ti triplets in the experimental data and the PrismSPECT simulation was performed. Fig. 5.16 shows a sample of where the peak intensity was taken from the intensity corrected experimental data. The simulation from a specific temperature and pressure with the closest match to that ratio was chosen (see Tables 5.7-5.9). Tables 5.10-5.12 show the results of these simulations for each of the three sample positions in the 6 data sets. Fig. 5.20 shows a comparison of modeled spectra from PrismSPECT at 20 Torr and 1,400 K. The experimental spectrum was located 0.86 mm in front of the target surface and was imaged at 5 μs in O_2.

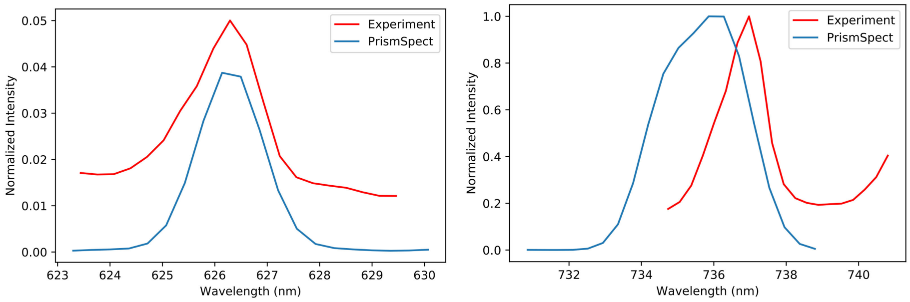

(a) **(b)**

Figure 5.20 These plots show a comparison between two sets of Ti I triplets simulated by PrismSPECT and measured experimentally.

Shot Seq.	**Exp. Ratio**	**Sim. Ratio**	**Percent Error**
1	0.0500	0.0584	16.75
2	0.1771	0.1786	0.87
3	0.0497	0.0584	17.45
4	0.2419	0.2274	6.00
5	0.0562	0.0584	4.00
6	0.2520	0.2274	9.78

Table 5.7 Ratios at 0.86 mm.

Shot Seq.	**Exp. Ratio**	**Sim. Ratio**	**Percent Error**
1	0.0683	0.0584	14.54
2	0.2476	0.2274	8.18
3	0.0663	0.0584	11.93
4	0.2411	0.2274	5.68
5	0.0859	0.0795	7.46
6	0.2728	0.2274	16.65

Table 5.8 Ratios at 2.90 mm.

Shot Seq.	**Exp. Ratio**	**Sim. Ratio**	**Percent Error**
1	0.0950	0.0982	3.31
2	0.2991	0.2274	23.98
3	0.0908	0.0982	8.09
4	0.2640	0.2274	13.88
5	0.0737	0.0795	7.85
6	0.2455	0.2274	7.38

Table 5.9 Ratios at 4.08 mm.

Shot Seq.	**Temp. (K)**	**Pres. (Torr)**
1	1400	30
2	1400	110
3	1400	30
4	1400	200
5	1400	30
6	1400	200

Table 5.10 Temperatures at 0.86 mm.

Shot Seq.	**Temp. (K)**	**Pres. (Torr)**
1	1400	30
2	1400	200
3	1400	30
4	1400	200
5	1400	40
6	1400	200

Table 5.11 Temperatures at 2.90 mm.

Shot Seq.	**Temp. (K)**	**Pres. (Torr)**
1	1400	50
2	1400	200
3	1400	50
4	1400	200
5	1400	40
6	1400	200

Table 5.12 Temperatures at 4.08 mm.

Simulations of the TiO spectrum with PGOPHER were completed to show that TiO did emit in the wavelength window probed with the fast imaging. The constants used to model TiO are shown in Tables 5.13 and 5.14. Fig. 5.21 shows the results of the simulation for the γ and γ' bands. This simulation accurately reflects the instrumental resolution of the Acton spectrometer and the grating used in the TiO experiments.

State	**v**	**Origin (eV)**	**B (s^{-1})**	**A**	λ_S	**D**
$X^3\Delta$	0	0	0.5339	50.6512	1.7473	6.012×10^{-7}
$A^3\Phi$	0	14092.84	0.505815	57.957	-0.515184	6.907×10^{-7}
$A^3\Phi$	1	14952.74	0.50265	57.854	-0.512816	6.884×10^{-7}
$A^3\Phi$	2	15804.75	0.499465	57.75	0.510816	6.86×10^{-7}
$B^3\Pi$	0	16145.49	0.506174	—	—	6.859×10^{-7}

Table 5.13 Constants used for modeling TiO with PGOPHER [97,98]

State	**v**	**H**	λ_d	A_d
$X^3\Delta$	0	2.814×10^{-14}	6.801×10^{-7}	-2.65×10^{-5}
$A^3\Phi$	0	8.25×10^{-14}	-4.22×10^{-6}	-4.18×10^{-5}
$A^3\Phi$	1	2.8×10^{-14}	-3.67×10^{-6}	-4.16×10^{-5}
$A^3\Phi$	2	6.01×10^{-14}	-3.09×10^{-6}	-4.14×10^{-5}
$B^3\Pi$	0	—	—	—

Table 5.14 Additional constants used for modeling TiO with PGOPHER [97,98].

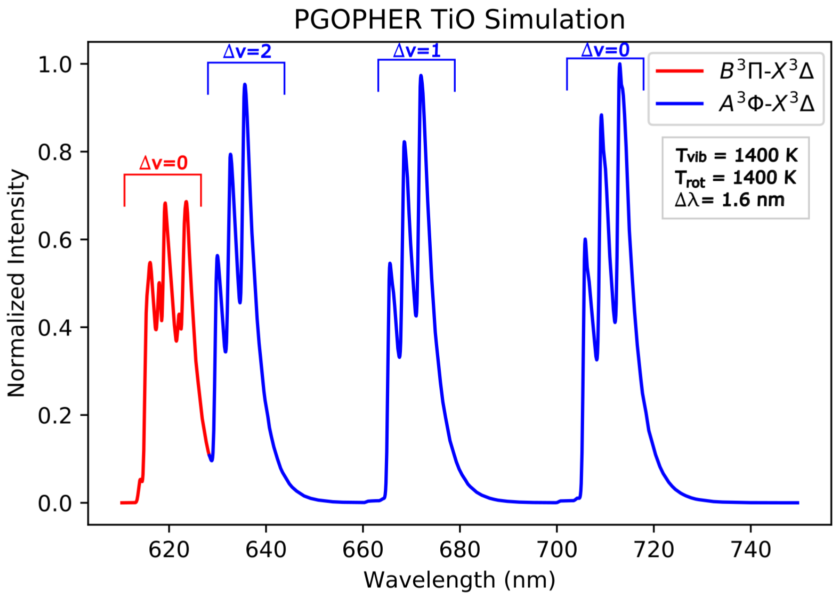

Figure 5.21 PGOPHER simulation of the TiO γ ($A^3\Phi \rightarrow X^3\Delta$) and γ' ($B^3\Pi \rightarrow X^3\Delta$) bands.

The Gibbs free energy and enthalpy of various possible chemical reaction pathways for Ti and O provides the likelihood of TiO formation. The enthalpy is defined as:

$$H = E_{int} + PV, \tag{5.6}$$

with the internal energy, E_{int}, the pressure, P, and volume, V. The Gibbs free energy is defined as:

$$G = H + TS. \tag{5.7}$$

T is temperature and S is entropy. The change in enthalpy and Gibbs free energy can be calculated for these reactions using data from the NIST-JANAF Thermochemical tables [99].

Two pathways of interest at 1 atm and 1,000 K are:

$$Ti + O_2 \longleftrightarrow TiO + O : \qquad \Delta H = 300.9\ \ kJ/mol, \qquad \Delta G = 146.1\ \ kJ/mol; \quad (5.8)$$

$$Ti + O + M \longleftrightarrow TiO + M : \qquad \Delta H = -204.5\ \ kJ/mol, \qquad \Delta G = -229.3\ \ kJ/mol. \quad (5.9)$$

A full analysis of the thermodynamic and equilibrium conditions is needed to properly evaluate the reaction pathways. Each calculation would need to be adjusted for the rarefied environments used in this experiment. The density in the plume behind the shock wave would need to be accurately known to properly adjust for the reduced pressure environment.

The data from this series of experiments showed that TiO formation occurred 1-3 mm behind the shock wave. TiO emission was observed to occur more strongly in the O_2 environment than in the N_2 environment. Weak TiO emission may be present in the light emitted by the plume in the N_2 environment from oxides on the target surface. The signal is extremely weak and may have also been broadband background. Analysis of neutral Ti emission spectroscopy indicated a temperature range of 700-800 K at the 5 μs delay time. The temperature was slightly higher at 9 μs and ranged from 920-1,060 K. Simulations with PrismSPECT showed a consistent temperature of 1,400 K with gas pressure in the plume varying from 30-200 Torr.

Chapter 6

Conclusion

This dissertation has described the design, building, characterization, and metrology of the LAPeX apparatus and its use in two novel experiments. The first experiment involved the study of absorption spectroscopy of C_2 in carbon plumes. The second experiment examined formation of TiO in titanium plumes expanding into oxygen. Laser ablation is a versatile experimental method for investigating plasmas, materials properties, shock physics, laboratory astrophysics, and other topics. Laser ablation also has many applications including thin film production and LIBS/LAMIS.

The processes involved in laser ablation are not studied by a single specialty or even a single scientific discipline. A complete description of laser ablation requires physics, chemistry, and materials science. The processes that can be modeled using laser ablation span subjects from particle physics to astrophysics. A full understanding of the mechanisms underlying the laser ablation process has not yet been achieved in the scientific community. The careful study of laser ablation is critical to better understand and characterize the processes involved in the various applications of laser ablation.

Experiments involving laser ablation cover a large parameter space. The LAPeX apparatus was designed to measure the variables in that space. Design concepts for LAPeX included flexibility and complete coverage of the experimental parameter space. The LAPeX design concept of measuring a large portion of the laser ablation parameter space led to the development of an experimental platform that incorporates traditional diagnostics and applies them in new combinations and new use configurations. LAPeX provides a robust platform for studying laser ablation plumes and provides the experimenter the ability to expand to add new diagnostics or ablation lasers. Spectroscopic diagnostics, optical density diagnostics, fast imaging, and mass/charge analyzers were methodically aligned, calibrated, and tested during the building of the LAPeX apparatus.

Proper calibration and characterization are required to obtain physically meaningful data from experimental work. Extensive effort was applied to properly characterize the diagnostic elements of the LAPeX apparatus. The spectroscopic diagnostics were carefully calibrated for wavelength and detector response using a variety of tools. LAPeX successfully collected spatially and temporally resolved data from ablation plumes produced at various laser intensities and in various gas backgrounds. The experiments presented in this dissertation provide an example of the diverse research applications of the LAPeX apparatus.

Absorption spectroscopy of simple molecules provides a new method for probing laser ablation plumes. Useful information about the formation and evolution of molecules can be obtained by observing the region of the plume which is no longer emitting light. Information about plume composition, temperature, and pressure can be deduced from the spectral data with proper spectroscopic modeling. The data shown in Chapter 4 demonstrates the usefulness of supercontinuum absorption spectroscopy for observing simple molecules such as C_2. The combination of a high-power supercontinuum laser and a time gated ICCD provide the ability to capture time resolved data from the plume at times when collecting emitted light is difficult and requires long gate windows (10's of μs). The data collected in this experiment from the carbon plumes required a 500 ns gate.

A data reduction analysis program was written to extract the absorption spectrum from the total spectrum collected with the ICCD detector. Spectroscopic modeling was required to determine the C_2 molecular temperatures and spectral broadening. PGOPHER simulations and spectral line width analysis of the absorption data showed $T_{rot} \sim 5,000$ K and $T_{vib} \sim 2,000$ K for the C_2 molecules. Challenges in analyzing the pressure broadening included the paucity of sufficient cross section data for C_2. A 500 ns gate is too long to observe the atomic/ionic species present in the plume but does permit the observation of molecular species. Shorter gate windows are possible with a pulsed supercontinuum laser allowing for better atomic/ionic data. The detector would be exposed to the supercontinuum light for a shorter period of time reducing the danger to the intensifier and CCD chip.

Understanding the formation mechanisms of TiO, SiO, FeO, and other simple molecules is a critical step to understanding the evolution of matter from the atoms in stars to the molecules that make up dust and rock in the universe. TiO has a particularly interesting formation path near the hypergiant ρ Cassiopeiae. The specific conditions needed to form TiO from Ti and O/O_2 appear to occur as the shock wave of material ejected from ρ Cas passes through oxygen rich clouds. The LAPeX apparatus served as an experimental platform to create a scaled down version of the environment TiO is formed in near ρ Cas. Fast imaging showed strong TiO emission at 5 μs. Spectroscopic analysis at three separate locations along the propagation axis at a delay of 5 μs determined the Ti I temperature to be near 1,000 K. Spectroscopic modeling to determine the pressure in the plume showed a range of pressures from 30 Torr to 200 Torr.

Ablation plume spectroscopy, using a supercontinuum laser to probe the plume, successfully captured C_2 Swan band absorption. TiO formation, behind a propagating shock wave produced by laser ablation, was demonstrated. By integrating the new use of various components of the new LAPeX apparatus in these two experiments, the stated purpose, which was to better understand and measure the evolution and energy partitioning of an ablation plume, from the warm dense plasma stage to the cool neutral gas stage, was accomplished.

Bibliography

[1] T. H. Maiman, "Stimulated optical radiation in ruby," *Nature*, vol. 187, no. 4736, pp. 493–494, 1960.

[2] A. L. Schawlow and C. H. Townes, "Infrared and optical masers," *Phys. Rev.*, vol. 112, pp. 1940–1949, Dec 1958.

[3] J. L. Bromberg, "A Historian's View of the Gould Laser Patent Controversy." `https://history.aip.org/history/exhibits/laser/pdf/BrombergExcerpt.pdf`.

[4] F. McClung and R. Hellwarth, "Giant optical pulsations from ruby," *Journal of Applied Physics*, vol. 33, no. 3, pp. 828–829, 1962.

[5] F. J. McClung and R. W. Hellwarth, "Characteristics of giant optical pulsations from ruby," *Proceedings of the IEEE*, vol. 51, pp. 46–53, Jan 1963.

[6] J. F. Ready, *Effects of High-Power Laser Radiation.* United States: Academic Press, Inc., 1971.

[7] C. R. Phipps, *Laser ablation and its applications*, vol. 129. New York, NY: Springer, 2007.

[8] M. Capitelli, A. Casavola, G. Colonna, and A. D. Giacomo, "Laser-induced plasma expansion: theoretical and experimental aspects," *Spectrochimica Acta Part B: Atomic Spectroscopy*, vol. 59, no. 3, pp. 271 – 289, 2004.

[9] S. E. Black, *Laser Ablation: Effects and Applications.* Lasers and Electro-optics Research and Technology, Nova Science Publishers, Inc, 2011.

[10] J. C. Miller and R. F. J. Haglund, *Laser Ablation and Desorption*, vol. 30. San Diego: Academic Press, 1998.

[11] S. Georgiou and A. Koubenakis, "Laser-induced material ejection from model molecular solids and liquids: Mechanisms, implications, and applications," *Chemical Reviews*, vol. 103, no. 2, pp. 349–394, 2003. PMID: 12580635.

[12] R. Russo, X. Mao, H. Liu, J. Yoo, and S. Mao, "Time-resolved plasma diagnostics and mass removal during single-pulse laser ablation," *Applied Physics A*, vol. 69, no. 1, pp. S887–S894, 1999.

[13] R. Russo, X. Mao, C. Liu, and J. Gonzalez, "Laser assisted plasma spectrochemistry: laser ablation," *Journal of Analytical Atomic Spectrometry*, vol. 19, no. 9, pp. 1084–1089, 2004.

[14] P. R. Willmott and J. R. Huber, "Pulsed laser vaporization and deposition," *Rev. Mod. Phys.*, vol. 72, pp. 315–328, Jan 2000.

[15] M. Koenig, A. Benuzzi-Mounaix, A. Ravasio, T. Vinci, N. Ozaki, S. Lepape, D. Batani, G. Huser, T. Hall, D. Hicks, A. MacKinnon, P. Patel, H. S. Park, T. Boehly, M. Borghesi, S. Kar, and L. Romagnani, "Progress in the study of warm dense matter," *Plasma Physics and Controlled Fusion*, vol. 47, pp. B441–B449, nov 2005.

[16] C. Kerse, H. Kalaycıoğlu, P. Elahi, B. Çetin, D. K. Kesim, Ö. Akçaalan, S. Yavaş, M. D. Aşık, B. Öktem, H. Hoogland, *et al.*, "Ablation-cooled material removal with ultrafast bursts of pulses," *Nature*, vol. 537, no. 7618, pp. 84–88, 2016.

[17] H. M. Smith and A. F. Turner, "Vacuum deposited thin films using a ruby laser," *Appl. Opt.*, vol. 4, pp. 147–148, Jan 1965.

[18] D. H. Lowndes, D. B. Geohegan, A. A. Puretzky, D. P. Norton, and C. M. Rouleau, "Synthesis of novel thin-film materials by pulsed laser deposition," *Science*, vol. 273, p. 898, Aug 16 1996. Copyright - Copyright American Association for the Advancement of Science Aug 16, 1996; Last updated - 2017-10-31; CODEN - SCIEAS.

[19] D. B. Chrisey and G. K. Hubler, *Pulsed Laser Deposition of Thin Films.* New York: J. Wiley, 1994.

[20] R. Wood, J. Leboeuf, K. Chen, D. Geohegan, and A. Puretzky, "Dynamics of plume propagation, splitting, and nanoparticle formation during pulsed-laser ablation," *Applied Surface Science*, vol. 127-129, pp. 151 – 158, 1998.

[21] C. Phipps, M. Birkan, W. Bohn, H.-A. Eckel, H. Horisawa, T. Lippert, M. Michaelis, Y. Rezunkov, A. Sasoh, W. Schall, *et al.*, "Laser-ablation propulsion," *Journal of Propulsion and Power*, vol. 26, no. 4, pp. 609–637, 2010.

[22] H. Horisawa, M. Kawakami, and I. Kimura, "Laser-assisted pulsed plasma thruster for space propulsion applications," *Applied Physics A*, vol. 81, pp. 303–310, Jul 2005.

[23] I. Levchenko, K. Bazaka, Y. Ding, Y. Raitses, S. Mazouffre, T. Henning, P. J. Klar, S. Shinohara, J. Schein, L. Garrigues, M. Kim, D. Lev, F. Taccogna, R. W. Boswell, C. Charles, H. Koizumi, Y. Shen, C. Scharlemann, M. Keidar, and S. Xu, "Space micropropulsion systems for cubesats and small satellites: From proximate targets to furthermost frontiers," *Applied Physics Reviews*, vol. 5, no. 1, p. 011104, 2018.

[24] NASA, “CubeSats.” `https://www.nasa.gov/mission_pages/cubesats/overview`.

[25] The CubeSat Program, *CubeSat Design Specification*. California Polytechnic State University, 13 ed., Apr. 2015.

[26] G. Colonna, A. Casavola, and M. Capitelli, “Modelling of LIBS plasma expansion,” *Spectrochimica Acta Part B: Atomic Spectroscopy*, vol. 56, no. 6, pp. 567 – 586, 2001.

[27] D. W. Hahn and N. Omenetto, “Laser-induced breakdown spectroscopy (LIBS), part I: Review of basic diagnostics and plasma—particle interactions: Still-challenging issues within the analytical plasma community,” *Applied Spectroscopy*, vol. 64, no. 12, pp. 335A–336A, 2010. PMID: 21144145.

[28] S. V. Shabanov and I. B. Gornushkin, “Modeling chemical reactions in laser-induced plasmas,” *Applied Physics A*, vol. 121, pp. 1087–1107, Nov 2015.

[29] R. E. Russo, A. A. Bol’shakov, X. Mao, C. P. McKay, D. L. Perry, and O. Sorkhabi, “Laser ablation molecular isotopic spectrometry,” *Spectrochimica Acta Part B: Atomic Spectroscopy*, vol. 66, no. 2, pp. 99 – 104, 2011.

[30] R. E. Russo, X. Mao, J. J. Gonzalez, V. Zorba, and J. Yoo, “Laser ablation in analytical chemistry,” *Analytical Chemistry*, vol. 85, no. 13, pp. 6162–6177, 2013. PMID: 23614661.

[31] A. A. Bol’shakov, X. Mao, J. J. Gonzalez, and R. E. Russo, “Laser ablation molecular isotopic spectrometry (LAMIS): current state of the art,” *J. Anal. At. Spectrom.*, vol. 31, pp. 119–134, 2016.

[32] A. A. Bol’shakov, X. Mao, J. Jain, D. L. McIntyre, and R. E. Russo, “Laser ablation molecular isotopic spectrometry of carbon isotopes,” *Spectrochimica Acta Part B: Atomic Spectroscopy*, vol. 113, pp. 106 – 112, 2015.

[33] S. Jacquemot, “Inertial confinement fusion for energy: overview of the ongoing experimental, theoretical and numerical studies,” *Nuclear Fusion*, vol. 57, p. 102024, Aug 2017.

[34] B. A. Remington, “High energy density laboratory astrophysics,” *Plasma Physics and Controlled Fusion*, vol. 47, pp. A191–A203, Apr 2005.

[35] É. Falize, C. Michaut, and S. Bouquet, “Similarity properties and scaling laws of radiation hydrodynamic flows in laboratory astrophysics,” *The Astrophysical Journal*, vol. 730, p. 96, Mar 2011.

[36] M. Von Allmen and . Blatter, Andreas, *Laser-Beam Interactions with Materials: Physical Principles and Applications*, vol. 2. New York;Berlin;: Springer, second update ed., 1995.

[37] B. E. A. Saleh and M. C. Teich, *Fundamentals of Photonics.* New York: Wiley, 1991.

[38] P. W. Milonni and J. H. Eberly, *Laser Physics.* Hoboken: John Wiley & Sons, 2010.

[39] S. Amoruso, R. Bruzzese, N. Spinelli, and R. Velotta, "Characterization of laser-ablation plasmas," *Journal of Physics B: Atomic, Molecular and Optical Physics*, vol. 32, no. 14, p. R131, 1999.

[40] B. N. Chichkov, C. Momma, S. Nolte, F. von Alvensleben, and A. Tünnermann, "Femtosecond, picosecond and nanosecond laser ablation of solids," *Applied Physics A*, vol. 63, pp. 109–115, Aug 1996.

[41] I. A. B. Zel'dovich, I. U. P. Raĭzer, W. D. Hayes, and R. F. Probstein, *Physics of Shock Waves and High-Temperature Hydrodynamic Phenomena.* New York: Academic Press, 1966.

[42] A. D. Giacomo and J. Hermann, "Laser-induced plasma emission: from atomic to molecular spectra," *Journal of Physics D: Applied Physics*, vol. 50, no. 18, p. 183002, 2017.

[43] F. Chen, *Introduction to Plasma Physics and Controlled Fusion: Volume 1: Plasma Physics.* Springer US, 2013.

[44] R. Goldston and P. Rutherford, *Introduction to Plasma Physics.* CRC Press, 1995.

[45] R. Hippler, *Low Temperature Plasma Physics: Fundamental Aspects and Applications.* Berlin: Wiley-VCH, first ed., 2001.

[46] D. Margarone, *Ion Acceleration and Diagnostics in Laser-Genereated Plasmas.* Ph.D. Thesis, Universita de gli Studi di Messina Scuola di Dottorato in Fisica, 2007.

[47] G. Cristoforetti, A. D. Giacomo, M. Dell'Aglio, S. Legnaioli, E. Tognoni, V. Palleschi, and N. Omenetto, "Local thermodynamic equilibrium in laser-induced breakdown spectroscopy: Beyond the McWhirter criterion," *Spectrochimica Acta Part B: Atomic Spectroscopy*, vol. 65, no. 1, pp. 86 – 95, 2010.

[48] G. Cristoforetti, E. Tognoni, and L. Gizzi, "Thermodynamic equilibrium states in laser-induced plasmas: From the general case to laser-induced breakdown spectroscopy plasmas," *Spectrochimica Acta Part B: Atomic Spectroscopy*, vol. 90, pp. 1 – 22, 2013.

[49] P. Kundu, I. Cohen, and H. Hu, *Fluid Mechanics.* Elsevier Science, 2001.

[50] A. V. Gusarov and I. Smurov, “Gas-dynamic boundary conditions of evaporation and condensation: Numerical analysis of the Knudsen layer,” *Physics of Fluids*, vol. 14, no. 12, pp. 4242–4255, 2002.

[51] H. Griem, *Principles of Plasma Spectroscopy.* Cambridge Monographs on Plasma Physics, Cambridge University Press, 2005.

[52] R. Cowan, *The Theory of Atomic Structure and Spectra.* Los Alamos Series in Basic and Applied Sciences, University of California Press, 1981.

[53] G. Herzburg, *Molecular Spectra and Molecular Structure*, vol. I. Spectra of Diatomic Molecules. D. Van Nostrand Company, Inc., 2nd ed., 1950.

[54] M. Weissbluth, *Atoms and Molecules.* Elsevier Science, 2012.

[55] J. McHale, *Molecular Spectroscopy.* Prentice Hall, 1999.

[56] N. OHNO, M. A. RAZZAK, H. UKAI, S. TAKAMURA, and Y. UESUGI, “Validity of electron temperature measurement by using Boltzmann plot method in radio frequency inductive discharge in the atmospheric pressure range,” *Plasma and Fusion Research*, vol. 1, pp. 028–028, 2006.

[57] J. Steinfeld, *Molecules and Radiation: An Introduction to Modern Molecular Spectroscopy. Second Edition.* Dover Books on Chemistry, Dover Publications, 2005.

[58] R. Kakkar, *Atomic and Molecular Spectroscopy: Basic Concepts and Applications.* Cambridge University Press, 2015.

[59] I. Hutchinson, *Principles of Plasma Diagnostics.* Cambridge University Press, 2005.

[60] R. K. Hanson, “Quantitative Laser Diagnostics for Combustion Chemistry and Propulsion Lecture 6: Spectral Lineshapes.” `https://cefrc.princeton.edu/sites/cefrc/files/2018_hanson_plecture6.pdf`, 2018.

[61] M. E. Sherrill, *Spectroscopic Modeling and Characterization of a Laser-Ablated Lithium-Silver Plasma Plume.* Ph.D. Dissertation, University of Nevada, Reno, May 2003.

[62] M. E. Sherrill, R. C. Mancini, J. Bailey, A. Filuk, B. Clark, P. Lake, and J. Abdallah, “Spectroscopic modeling and characterization of a collisionally confined laser-ablated plasma plume,” *Phys. Rev. E*, vol. 76, p. 056401, Nov 2007.

[63] R.C. Mancini, “HED Plasma Atomic Spectroscopy Lecture 11.” Private Communication, 2020.

[64] T. C. Williams and C. R. Shaddix, “Simultaneous correction of flat field and nonlinearity response of intensified charge-coupled devices,” *Review of Scientific Instruments*, vol. 78, no. 12, p. 123702, 2007.

[65] J. J. Iratcabal, *Investigating Total Charge Liberation From Low Intensity Laser Ablation of Solid Targets.* Undergraduate Honors Senior Thesis, University of Nevada, Reno, May 2010.

[66] Hiden Analytical, “HPR-60 MBMS.” `https://www.hidenanalytical.com/products/for-gas-analysis/hpr-60-mbms/`.

[67] H. Yousfi, S. Abdelli-Messaci, O. Ouamerali, and A. Dekhira, “A comparative study of carbon plasma emission in methane and argon atmospheres,” *Spectrochimica Acta Part B: Atomic Spectroscopy*, vol. 142, pp. 97 – 107, 2018.

[68] S. S. Harilal, R. C. Issac, C. V. Bindhu, V. P. N. Nampoori, and C. P. G. Vallabhan, “Spatial analysis of C_2 band emission from laser produced plasma,” *Plasma Sources Science and Technology*, vol. 6, no. 3, p. 317, 1997.

[69] S. S. Harilal, R. C. Issac, C. V. Bindhu, V. P. N. Nampoori, and C. P. G. Vallabhan, “Optical emission studies of C_2 species in laser-produced plasma from carbon,” *Journal of Physics D: Applied Physics*, vol. 30, no. 12, p. 1703, 1997.

[70] M. A. Fareed, S. Mondal, Y. Pertot, and T. Ozaki, “Carbon molecules for intense high-order harmonics from laser-ablated graphite plume,” *Journal of Physics B: Atomic, Molecular and Optical Physics*, vol. 49, no. 3, p. 035604, 2016.

[71] M. Dong, G. C.-Y. Chan, X. Mao, J. J. Gonzalez, J. Lu, and R. E. Russo, “Elucidation of C_2 and CN formation mechanisms in laser-induced plasmas through correlation analysis of carbon isotopic ratio,” *Spectrochimica Acta Part B: Atomic Spectroscopy*, vol. 100, pp. 62 – 69, 2014.

[72] W. Swan, “XXIX.—On the prismatic spectra of the flames of compounds of carbon and hydrogen,” *Transactions of the Royal Society of Edinburgh*, vol. 21, no. 3, p. 411–429, 1857.

[73] S. S. Harilal, B. E. Brumfield, N. L. LaHaye, K. C. Hartig, and M. C. Phillips, “Optical spectroscopy of laser-produced plasmas for standoff isotopic analysis,” *Applied Physics Reviews*, vol. 5, no. 2, p. 021301, 2018.

[74] A. Bayliss, “Rolling out revolution: Using radiocarbon dating in archaeology,” *Radiocarbon*, vol. 51, no. 1, p. 123–147, 2009.

[75] D. L. Lambert, Y. Sheffer, A. C. Danks, C. Arpigny, and P. Magain, “High-resolution spectroscopy of the C_2 Swan 0-0 band from Comet P/Halley,” *The Astrophysical Journal*, vol. 353, pp. 640–653, Apr. 1990.

[76] Kowalski, P. M., "The origin of peculiar molecular bands in cool DQ white dwarfs," *A&A*, vol. 519, p. L8, 2010.

[77] NKT Photonics, "SUPERK EXTREME SUPERCONTINUUM LASERS." `https://www.nktphotonics.com/lasers-fibers/product/superk-extreme-fianium-supercontinuum-lasers/`.

[78] Martin Hipp, et al., "Application of interferometric fringe evaluation software at Technical University Graz," 1999.

[79] M. Hipp, et al., "Digital evaluation of interferograms," *Measurement*, vol. 36, no. 1, pp. 53 – 66, 2004.

[80] "Interferometry, Optical Metrology: IDEA-Interferometric Data Evaluation Algorithms." `http://optics.tu-graz.ac.at/`.

[81] J. H. Goebel, J. D. Bregman, D. M. Cooper, D. Goorvitch, S. R. Langhoff, and F. C. Witteborn, "The c_2h, c_2 and cn electronic absorption bands in the carbon star hd 19557.," *The Astrophysical Journal*, vol. 270, pp. 190–199, July 1983.

[82] S. S. Harilal, C. V. Bindhu, R. C. Issac, V. P. N. Nampoori, and C. P. G. Vallabhan, "Electron density and temperature measurements in a laser produced carbon plasma," *Journal of Applied Physics*, vol. 82, no. 5, pp. 2140–2146, 1997.

[83] C. Western, "A Program for Simulating Rotational, Vibrational and Electronic Spectra." `http://pgopher.chm.bris.ac.uk`.

[84] C. M. Western, "PGOPHER: A program for simulating rotational, vibrational and electronic spectra," *Journal of Quantitative Spectroscopy and Radiative Transfer*, vol. 186, pp. 221 – 242, 2017. Satellite Remote Sensing and Spectroscopy: Joint ACE-Odin Meeting, October 2015.

[85] A. Tanabashi, T. Hirao, T. Amano, and P. F. Bernath, "The Swan system of C_2 : A global analysis of fourier transform emission spectra," *The Astrophysical Journal Supplement Series*, vol. 169, pp. 472–484, Apr 2007.

[86] J. S. Brooke, P. F. Bernath, T. W. Schmidt, and G. B. Bacskay, "Line strengths and updated molecular constants for the C_2 Swan system," *Journal of Quantitative Spectroscopy and Radiative Transfer*, vol. 124, pp. 11 – 20, 2013.

[87] C. Naulin, M. Costes, and G. Dorthe, "C_2 radicals in a supersonic molecular beam. radiative lifetime of the $d^3\pi_g$ state measured by laser-induced fluorescence," *Chemical Physics Letters*, vol. 143, no. 5, pp. 496 – 500, 1988.

[88] W. Bauer, K. H. Becker, C. Hubrich, R. Meuser, and J. Wildt, "Radiative lifetime measurements of the C_2 $(A^1\Pi_u)$ state," *The Astrophysical Journal*, vol. 296, pp. 758–764, Sept. 1985.

[89] C. de Jager, "The yellow hypergiants," *The Astronomy and Astrophysics Review*, vol. 8, pp. 145–180, Mar 1998.

[90] A. Lobel, G. Israelian, C. De Jager, F. Musaev, J. W. Parker, and A. Mavrogiorgou, "The spectral variability of the cool hypergiant ρ Cassiopeiae," *Astronomy and Astrophysics*, vol. 330, pp. 659–675, 1998.

[91] A. Lobel, J. Aufdenberg, I. Ilyin, and A. Rosenbush, "Mass-loss and recent spectral changes in the yellow hypergiant ρ Cassiopeiae," *arXiv preprint astro-ph/0504524*, 2005.

[92] A. Lobel, A. K. Dupree, R. P. Stefanik, G. Torres, G. Israelian, N. Morrison, C. de Jager, H. Nieuwenhuijzen, I. Ilyin, and F. Musaev, "High-resolution spectroscopy of the yellow hypergiant ρ Cassiopeiae from 1993 through the outburst of 2000-2001," *The Astrophysical Journal*, vol. 583, no. 2, p. 923, 2003.

[93] S. S. Harilal, B. E. Brumfield, B. D. Cannon, and M. C. Phillips, "Shock wave mediated plume chemistry for molecular formation in laser ablation plasmas," *Analytical Chemistry*, vol. 88, no. 4, pp. 2296–2302, 2016. PMID: 26732866.

[94] M. Kuehne, K. Danzmann, and M. Kock, "Oscillator strengths of TI I from hook and emission measurements," *Astronomy & Astrophysics*, vol. 64, pp. 111–113, Mar. 1978.

[95] A. Kramida, Yu. Ralchenko, J. Reader, and and NIST ASD Team. NIST Atomic Spectra Database (ver. 5.6.1), [Online]. Available: `https://physics.nist.gov/asd` [2018, December 11]. National Institute of Standards and Technology, Gaithersburg, MD., 2018.

[96] Prism Computational Sciences Inc., "PrismSPECT Overview." `http://prism-cs.com/Software/PrismSPECT/overview.html`, 2020.

[97] R. S. Ram, P. F. Bernath, M. Dulick, and L. Wallace, "The $a^3\phi - x^3\delta$ system (γ bands) of TiO: Laboratory and sunspot measurements," *The Astrophysical Journal Supplement Series*, vol. 122, pp. 331–353, May 1999.

[98] NIST, "NIST Chemistry WebBook." `webbook.nist.gov/chemistry/`.

[99] NIST-JANAF, "Thermochemical Tables." `http://kinetics.nist.gov/janaf/`.